博士論文

論文題目

The Relationship between Structural and Electrical Properties in Complex Oxide Heterostructures

（複合酸化物ヘテロ構造における構造特性と電気特性との相関）

氏　名　　佐藤　弘樹

It never gets easier, you just go faster. – Greg LeMond

Acknowledgments

At the top of the list, I would like to express my deepest gratitude to my supervisors: Prof. Harold Y. Hwang and Prof. Hiroshi Okamoto. Prof. Hwang has been my supervisor since I was an undergraduate, even after he has moved from the University of Tokyo to SLAC National Accelerator Laboratory, USA. His strong advice, both as a researcher and an educator, has been motivating and encouraging me. I learned from him what a scientist is, how a scientist should be. Also, living and working as a visiting researcher outside Japan was an irreplaceable experience, which would have definitely been impossible without his courtesy.

Although the research presented in this Thesis has been conducted practically in the USA, Prof. Okamoto has been giving me strong support from Japan. His intellectual guidance and crucial advice on my work greatly improved the quality of this Thesis. I should also note that his sincere help was indispensable for my movement to the USA with maintaining my formal position at the University of Tokyo.

I am also grateful to the committee members: Prof. Taka-hisa Arima, Prof. Mikk Lippmaa, Prof. Hideki Yoshizawa, and Dr. Yusuke Kozuka. Their critical comments on my work, based on their vast backgrounds, promoted a better consideration. The discussions with them during the pre-defense and the final defense significantly enriched this Thesis.

This work was directly supported by all of the menbers in Hwang laboratory. I would like to add sincere thanks to them: Dr. Yasuyuki Hikita, Dr. Hongtao Yuan, Dr. Yanwu Xie, Dr. Makoto Minohara, Dr. Bongju Kim, Dr. Adrian G. Swartz, Mr. Satoshi Harashima, Mr. Hisashi Inoue, Mr. Takashi Tachikawa, Mr. Di Lu, Mr. Brian Sae Yoon Kim, Mr. Tyler Merz, Mr. Zhuoyu Chen, Ms. Hyeok Yoon, and Mr. Yik Lun Lee. I cannot neglect the former members and the visitors I worked with: Dr. Christopher Bell, Dr. Takeaki Yajima, Dr. Takuya Higuchi, Dr. Minu Kim, Dr. Masayuki Hosoda, and Mr. Yuchi Liu; Prof. Joonghoe Dho (Kyungpook National University, Korea), Dr. Hiroyuki Nakamura (Osaka University), and Dr. Felix Gunkel (Peter Grünberg Institute, Germany). Through daily interactions with them, I learned a lot of things. Background knowledge, experimental methods, presentation skills are just a few examples of many. Also, my fruitful and enjoyable life in the laboratory was greatly supported by them.

I would equally like to emphasize that my work has been indirectly, but greatly supported by the administrative assistants: Ms. Hiromi Toyoi, Ms. Sachie Iimura, Ms. Yukiko Tan, Ms. Makiko Tanaka, and Ms. Deborah Woodward. Without their office work as well as cheerful words, I would not have been able to pursue my research.

Let me also express my appreciations to my collaborators outside the laboratory. I thank

Hitachi Kyowa Engineering Co., Ltd. for the inductively coupled plasma spectrometry measurements presented in Chap. 4. I am also thankful to Mr. Shaobo Zhu and Prof. Darrell G. Schlom (Cornell University, USA), for their strong support with the Rutherford backscattering spectrometry measurement presented in Chap. 4. I appreciate the kind help by Dr. Jaewook Kim, Dr. Marcelo Jaime, and Dr. Ross D. McDonald (National High Magnetic Field Laboratory, Los Alamos National Laboratory, USA) with the pulsed magnet experiment presented in Chap. 5. I am grateful to Prof. Kathryn A. Moler (Stanford University, USA) and the group members, especially Dr. Beena Kalisky, Dr. Julie A. Bert, and Mr. Eric M. Spanton, for characterizing my samples in detail using scanning superconducting quantum interference device, as presented in Chap. 6. I also thank Dr. Jun-Sik Lee and Prof. Chi-Chang Kao (SLAC National Accelerator Laboratory, USA) for their extensive research using spectroscopic techniques presented in Chap. 6.

While the results are not explicitly presented in this Thesis, I have really enjoyed working in collaboration with many other talented and sincere people. I thank Prof. Yasuhiro Yamada and Prof. Yoshihiko Kanemitsu (Kyoto University) for their measurement of the femtosecond optical absorption of my $LaAlO_3/SrTiO_3$ sample. I am also thankful to Dr. Rainer Jany and Dr. Christoph Richter (University of Augsburg, Germany), Dr. Carsten Woltmann, Dr. Georg Pfanzelt, and Prof. Jochen Mannhart (Max Planck Institute, Germany), for participating in the research on the local conductivity in $LaAlO_3/SrTiO_3$ heterointerfaces. I am grateful to Ms. Julia A. Mundy and Prof. David A. Muller (Cornell University, USA) for their scanning transmission electron microscopy measurements on some of my samples.

Last of all, I give my sincere thanks to my family for their endless support.

From the bottom of my heart,
February 2014

Hiroki Sato

Contents

Chapter 1

General Introduction

1.1 Background of oxide electronics

Complex oxide heterostructures have been attracting increasing interest for many years. This is first because of the rich variety of physical properties observed in bulk, that are absent in conventional semiconductors [1]. Perhaps the most famous example is the discovery of high-temperature superconductivity in the cuprates [2]. Such novel physical properties are important not only for fundamental physics, but also for possible device applications beyond conventional semiconductor electronics. For example, despite many remaining challenges, the high-temperature cuprate superconductors have been utilized for creating unconventional electronic devices [3]. Colossal magnetoresistance in manganites [4] may enable the design of novel magnetically operated devices. Ferroelectricity of $Pb(Zr,Ti)O_3$ has been applied to ferroelectric-gate field-effect transistors, which work as a nonvolatile memory [5, 6].

Notably, perovskite oxides share the same crystal structure [Figs. 1.1(a) and (b)] with a small difference in lattice constants [Fig. 1.1(c)]. This enables the fabrication of high-quality epitaxial heterostructures consisting of materials that have different physical properties. Artificial heterostructures of such perovskite oxides show an even wider range of properties, which are often different from those of the constituent materials. For example, La-Ca-Mn-O epitaxial thin films show an extremely large magnetoresistance (ratio $\sim 10^6\%$), orders of magnitude larger than in bulk [7, 8]. Another striking example can be found in superlattices. The [111]-oriented $LaCrO_3$-$LaFeO_3$ superlattice shows ferromagnetic order, although the constituent materials both have antiferromagnetic character [9]. A high-mobility electron gas at the interface between the insulating perovskite oxides $LaAlO_3$ and $SrTiO_3$ [10] is another representative case, which has been attracting many studies on this system, including this Thesis.

Thanks to the recent development of the fabrication and analysis techniques of artificial heterostructures, the field of oxide electronics is rapidly growing. One of the most common fabrication techniques is pulsed laser deposition (PLD), where ceramics targets are ablated by an ultraviolet pulsed laser and the evaporated species are transferred to substrates in the vacuum chamber (explained in more detail in Chap. 3). After growth of high-quality thin films of Y-Ba-Cu-O superconductors was demonstrated [12], PLD has been widely used for growth of artificial oxide heterostructures. A notable feature of PLD is that the energy source for evaporation

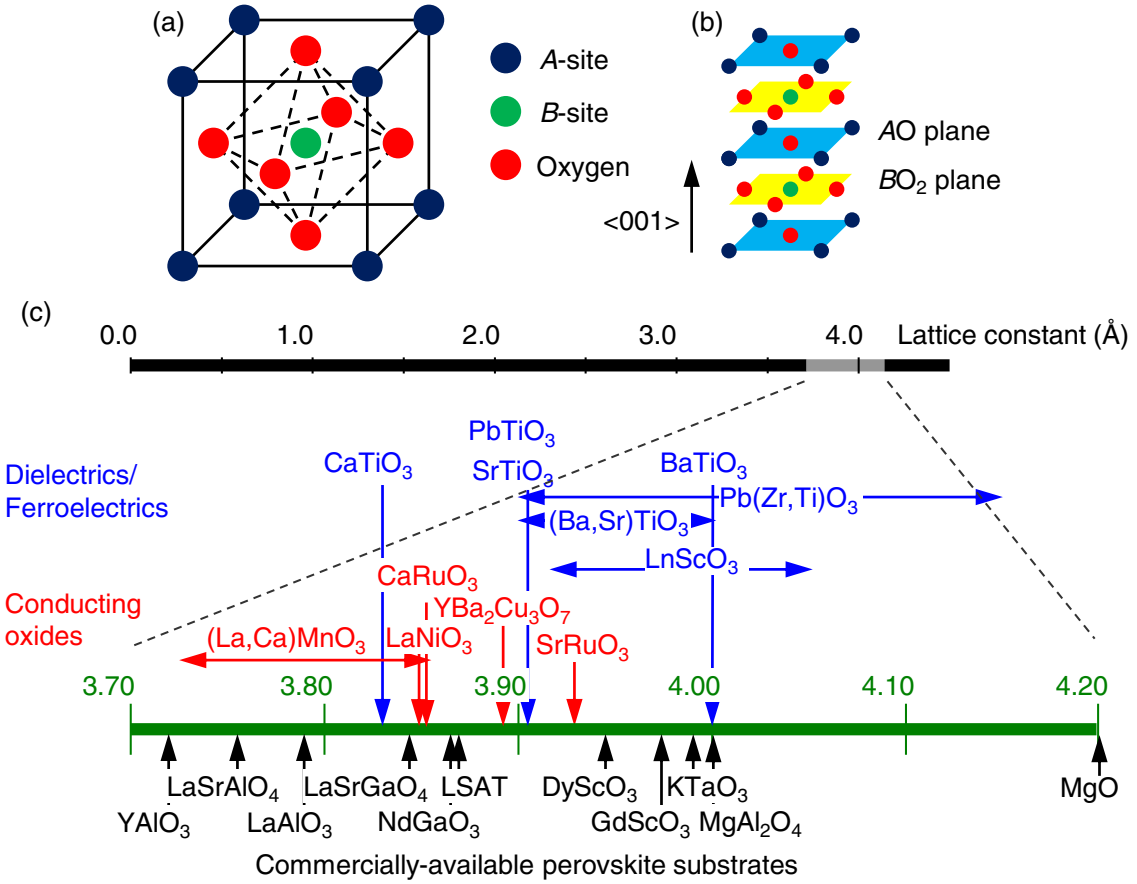

Fig. 1.1 (a) Cubic perovskite structure of ABO_3 and (b) its description as a stacking of alternating layers in the <001> directions. (c) (Pseudo-)Cubic lattice constants of perovskites. Adapted from Ref. [11].

is outside of the growth chamber, enabling flexible design of the growth system. In particular, many growth parameters (temperature, ambient gas pressure, energy of the ablating laser, etc) can be controlled over a wide range, which is often limited in other growth techniques. By optimizing such growth parameters, high-quality oxide thin films have been fabricated. The ability to grow high-quality films is often crucial to realize exotic physical properties. For example, by optimizing the growth conditions with high accuracy [13], a high-mobility two-dimensional electron system has been realized in the ZnO/$Mg_xZn_{1-x}O$ heterostructure, which is sufficiently clean that it shows the quantum Hall effect [14].

It has been becoming more and more evident, however, that in order to grow high-quality artificial oxide heterostructures by PLD, detailed control of the growth parameters is necessary. Several studies have pointed out that the structural and electrical properties of PLD-grown films can vary greatly with growth conditions, due to growth induced defects, especially off-stoichiometry [15–18]. Controversies have been caused by the sensitivity of growth control. For example, the actual physical mechanism of the room-temperature ferromagnetism in transition metal-doped TiO_2 grown by PLD [19] remains an open question, in particular because growth study using molecular beam epitaxy found negligible ferromagnetism in structurally

high-quality films [20]. The origin of the conductivity at the $LaAlO_3/SrTiO_3$ interface is another example, as discussed in the next Chapter.

The variation of the film quality thus often prevents detailed studies, potentially slowing down the further advance of this field. Therefore, in order to make a thorough investigation of complex oxide heterostructures, it is vital to obtain a better understanding on the sensitivity of the physical properties to all of the standard control parameters in thin film growth.

1.2 Scope and outline of this Thesis

Motivated by these backgrounds, we set the goal of this Thesis as obtaining detailed knowledge of the relationship between structural and electrical properties of complex oxide heterostructures, modulated by PLD growth conditions, which is necessary to further develop the field of oxide electronics. Two complex oxide systems are employed to demonstrate the importance of such fundamental growth study: the $LaAlO_3/SrTiO_3$ heterostructure and $SrMoO_3$ thin films. More detailed background and motivation to study these systems are described in Chap. 2.

The discovery of a conducting layer formed at the $LaAlO_3/SrTiO_3$ interface [10] has led to extensive research on this system. In particular, the low density superconductivity and the high electron mobility of $SrTiO_3$ (Sec. 2.2.1) indicate the possibility of novel two-dimensional electron physics in this system, such as the coexistence of the quantum Hall effect and superconductivity. However, the variation in growth parameters used by various groups leads to a wide range of reported properties, which are sometimes contrary to each other, preventing a thorough exploration of this system. In Chap. 4, we investigate the sensitivity of the properties of this system to the PLD growth parameters, which gives better understanding of the growth dependence of the electronic phase diagrams of this system. Based on the knowledge obtained, the possibility to realize novel electronic states at the interface is next investigated: mobility enhancement to observe quantum oscillations (Chap. 5) and ferromagnetism coexisting with superconductivity (Chap. 6).

$SrMoO_3$ is a "good and simple metal," with the highest conductivity among perovskite oxides [21], indicating that this material is a potentially useful building block of complex oxide heterostructures (Sec. 2.4.1). However, studies of this material are currently very limited, because of the difficulty in growth of this material that requires extremely strong reducing conditions. In Chap. 7, we aim to grow high-quality $SrMoO_3$ thin films by systematically tuning the PLD growth parameters, which should enable more detailed investigation of this potentially interesting material.

As summarized in Chap. 8, the results obtained in this work will play an important role as a basis for the study of complex oxide heterostructures. In particular, the high-quality $LaAlO_3/SrTiO_3$ and $SrMoO_3$ samples may enable the exploration of novel electron physics in these systems.

Chapter 2

Background

2.1 Outline

In this Chapter, we review previous studies on the systems investigated in this Thesis. For the $LaAlO_3/SrTiO_3$ heterostructure, bulk properties of the constituent materials are first explained in Sec. 2.2. Section 2.3.1 describes the most important discovery about this system: a conducting layer formed at the interface. By reviewing possible origins of the conductivity and controversy about this system in Secs. 2.3.2 and 2.3.3, the motivation to study this system is explained in Sec. 2.3.4.

For $SrMoO_3$, we first review bulk properties of this material in Sec. 2.4.1, which also explains why this material is potentially interesting from a thin film perspective. Section 2.4.2 describes a central experimental difficulty in studying this material. Based on this background, the aim of growing high-quality $SrMoO_3$ thin films is explained in Sec. 2.4.3.

2.2 Bulk properties of $SrTiO_3$ and $LaAlO_3$

2.2.1 $SrTiO_3$

$SrTiO_3$ has a cubic perovskite structure with a lattice constant of $a = 3.905$ Å at room temperature, and undergoes a cubic–tetragonal phase transition at around 105 K [22, 23]. Stoichiometric $SrTiO_3$ is a band insulator with a wide bandgap of ≈ 3.2 eV [24–26]. The conduction band consists of Ti $3d$ t_{2g} bands with the minimum located at the Γ point, while the valance band consists of O $2p$ bands with the maximum located either at the R point or the M point [27, 28].

The transport properties of $SrTiO_3$ can easily be modified with a small compositional change. The substitution of La at the Sr site, Nb at the Ti site, or the introduction of oxygen vacancies induces electronic conduction in bulk $SrTiO_3$. Notably, when the carrier density is relatively low, the Hall mobility can exceed 10^4 $cm^2V^{-1}s^{-1}$ at low temperatures [29–31], as shown in Figs. 2.1(a) and (d).

This exceptionally high mobility among transition metal oxides is a result of effective screening from impurities or defects by the extremely large permittivity, $\sim 2\times10^4\epsilon_0$ (ϵ_0 is the vacuum permittivity) at low temperature, as shown in Fig. 2.1(b). This property is understood based

on the idea that the effective temperature is limited by quantum fluctuations, suppressing the ferroelectric transition [32, 33]. Due to this incipient ferroelectricity, the dielectric response of $SrTiO_3$ is sensitive to many external parameters. For example, the large permittivity at low temperatures is suppressed by applying large electric fields [34, 35]. It is also remarkable that a ferroelectric transition at finite temperature can be induced in $SrTiO_3$ by chemical substitution [36, 37] or by applying stress [38, 39].

Utilizing the extremely large permittivity of $SrTiO_3$, the electronic properties of the $LaAlO_3/SrTiO_3$ heterointerface can be electrostatically modulated from the back-side using the $SrTiO_3$ substrate as the gate dielectric [40–42]. However, as mentioned, the dielectric response of $SrTiO_3$ is a nonlinear function of the electric field applied, which adds complexity to the back-gating [42, 43].

Another important feature of $SrTiO_3$ is the low density superconductivity. As shown in Figs. 2.1(c) and (d), $SrTiO_3$ becomes superconducting below $\lesssim 300$ mK over a carrier density range of $\sim 10^{19}$–10^{20} cm^{-3} [44–47]. The low density limit is somewhat controversial; superconductivity has recently been found with an extremely low carrier density of 5.5×10^{17} cm^{-3} [48]. This carrier density range is much lower than those of other semiconductors, which become superconducting only above a carrier concentration of $\sim 5 \times 10^{20}$ cm^{-3} [49–53]. It is only very recently that a few topological materials have been found to become superconducting with a carrier density which is comparable to that for $SrTiO_3$ [54–56].

2.2.2 $LaAlO_3$

$LaAlO_3$ has a trigonal perovskite structure with a pseudo-cubic lattice constant of $a = 3.790$ Å and interior angles of $\alpha = \beta = \gamma = 90.5°$ at room temperature, and undergoes a cubic–trigonal phase transition around 800 K [22, 60, 61]. Thus $LaAlO_3$ is reasonably well lattice-matched to $SrTiO_3$, which enables the fabrication of the $LaAlO_3/SrTiO_3$ heterostructure. Because of its distorted unit cell, $LaAlO_3$ has two different directions of crystal domains, creating a "twin structure" [62]. Throughout this Thesis, all the Miller indices and the lattice constants of $LaAlO_3$ are based on the pseudo-cubic perovskite unit.

$LaAlO_3$ is also a band insulator with a wider bandgap of ≈ 5.6 eV [63]. Unlike transition metal oxides, the valence state of each cation in $LaAlO_3$ is fixed as La^{3+} and Al^{3+}. Because of the wide bandgap and the fixed valence, electronic conduction can hardly be induced in $LaAlO_3$. Indeed, as shown in Fig. 2.2(a), the conductivity of $LaAlO_3$-based compounds is very low ($< 10^{-2}$ S cm^{-1}) and shows an Arrhenius type temperature dependence [64], contrasting to doped $SrTiO_3$, which shows much higher conductivity ($\gtrsim 1$ S cm^{-1}) and metallic behavior.

The permittivity of bulk $LaAlO_3$ is about $24\epsilon_0$ and does not have a strong temperature dependence over the temperature range of 300–4 K [65], as shown in Fig. 2.2(b). Because of this large permittivity, although much smaller than that of $SrTiO_3$, $LaAlO_3$ can also be used as a gate dielectric. Indeed, $LaAlO_3$ films have been utilized for electric field-effect devices with a top-gate geometry, which can effectively control the electronic properties of the $LaAlO_3/SrTiO_3$ heterointerface [66–68].

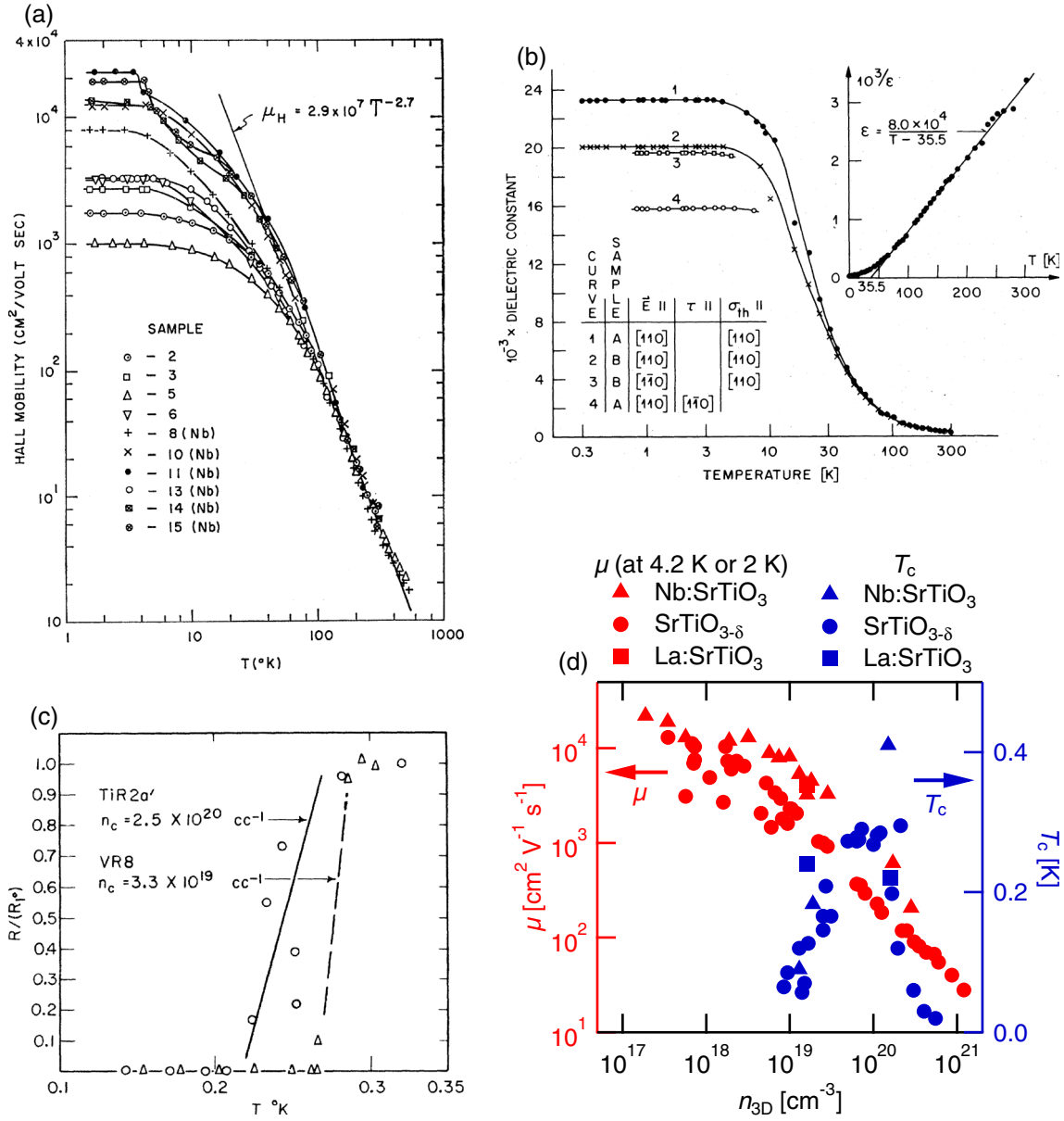

Fig. 2.1 Physical properties of bulk $SrTiO_3$. (a) Temperature dependence of the Hall mobility, doped by Nb or oxygen vacancies with various carrier concentrations. From Ref. [30], © 1967 American Physical Society. (b) Temperature dependence of the relative permittivity. From Ref. [33], © 1979 American Physical Society. (c) Temperature dependence of the resistance, normalized by that at 1 K, of reduced $SrTiO_3$. From Ref. [44], © 1964 American Physical Society. (d) Summary of the electron mobility (μ) at low temperature and the superconducting transition temperature (T_c) of $SrTiO_3$ single crystals as a function of three-dimensional carrier density (n_{3D}). Data are from Refs. [30, 57, 58] for μ and Refs. [47, 59] for T_c. Data summary is courtesy of Y. Kozuka.

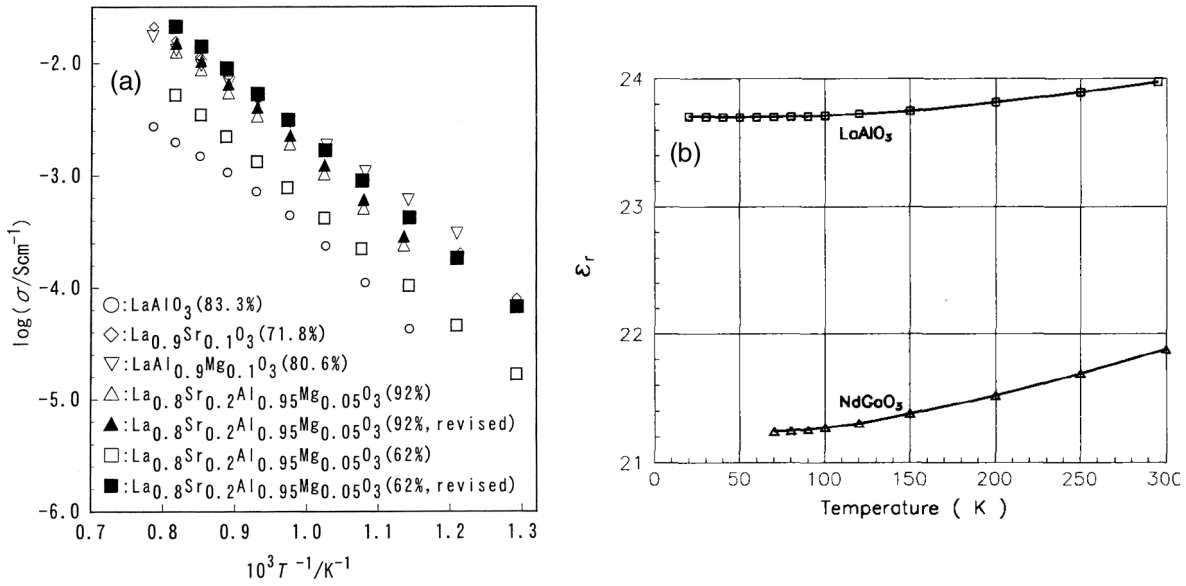

Fig. 2.2 Physical properties of bulk $LaAlO_3$. (a) Arrhenius plot of the total electrical conductivity of $LaAlO_3$-based compounds measured in air. Reprinted from Ref. [64], © 2000, with permission from Elsevier. (b) Temperature dependence of the relative permittivity of $LaAlO_3$ (and $NdGaO_3$). From Ref. [65], © 1994 IEEE.

2.3 $LaAlO_3/SrTiO_3$ heterointerface

2.3.1 Conductivity at the interface between two insulating oxides

Ohtomo and Hwang [10] have shown that a high-mobility electron gas is formed at the interface between the band insulators $LaAlO_3$ and $SrTiO_3$. They have demonstrated that, when $LaAlO_3$ is grown directly onto a TiO_2-terminated $SrTiO_3$ (001) substrate, the interface shows electronic conduction. The transport properties of the interface are shown in Fig. 2.3.

Subsequent studies have found that the interface shows not only electrical conductivity, but also many other intriguing properties. One representative example is the two-dimensional superconductivity below ≈ 200 mK [69]. It has also been reported that the high-mobility electron gas shows quantum oscillations at low temperature under high magnetic fields [70]. Magnetic ordering has also been suggested as the ground state of samples with a relatively low conductivity [71].

It is also remarkable that inserting only one monolayer of SrO between the $LaAlO_3$ film and the $SrTiO_3$ (001) substrate makes the system insulating [10, 72], emphasizing the importance of the atomic scale details at the interface. These unexpected results motivated many researchers to investigate the possibility of novel two-dimensional electron physics in this system as well as to search for the origin of the conductivity, as briefly reviewed in the following sections.

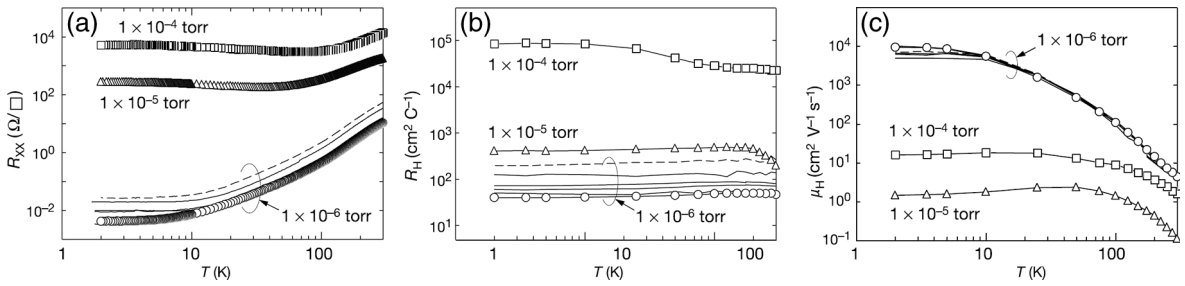

Fig. 2.3 Temperature dependence of (a) the sheet resistance, (b) the Hall coefficient, and (c) the Hall mobility of $LaAlO_3$ (60 Å)/$SrTiO_3$ (001) heterostructures grown in various oxygen pressures. Reprinted by permission from Macmillan Publishers Ltd: Nature [10], © 2004. Re-labeled following the corrigendum.

2.3.2 Possible origins of the conductivity

The polar discontinuity picture

To explain the origin of the conductivity and the strong impact of the one monolayer of SrO on it, the *polar discontinuity picture* has been suggested [73]. The perovskite structure ABO_3 can be described as a stacking of alternating layers of AO and BO_2 in the [001] direction (see Fig. 1.1(b)). If we consider atomically-abrupt $LaAlO_3/SrTiO_3$ (001) interfaces with perfect stoichiometry, they can be distinguished into two different types by the interface termination. One type is LaO/TiO_2, the other is AlO_2/SrO. Hereafter these two interfaces are referred to as the *n*-type and the *p*-type interfaces, respectively, as often used in the literature.[*1]

The *n*-type interface can be fabricated by depositing $LaAlO_3$ directly on a TiO_2-terminated $SrTiO_3$ (001) substrate, and the *p*-type interface can be fabricated by inserting one monolayer of SrO in between. By utilizing the large difference in solubility in acids between SrO and TiO_2 (the latter is more stable), a TiO_2-terminated $SrTiO_3$ surface can be created by selectively etching the SrO layer on the surface with buffered HF [74, 75], which has been applied in most studies of the $LaAlO_3/SrTiO_3$ (001) interface.

In the ionic limit, $SrTiO_3$ can be described as a sequence of charge-neutral sheets of $(SrO)^0$ and $(TiO_2)^0$, whereas $LaAlO_3$ can be described as a sequence of $\pm e$-charged (e is the elementary electric charge) sheets of $(LaO)^+$ and $(AlO_2)^-$, as schematically shown in Figs. 2.4(a) and (b). The charged sublayers produce an internal electric field E, which leads to a diverging electrostatic potential V with the $LaAlO_3$ film thickness, as shown in the figures. The interface termination determines the sign of the divergence.

It should be noted that the diverging electrostatic potential is deduced based only on elementary electrostatic considerations. In this sense the polar discontinuity is a fundamental problem in this system, and thus charge rearrangement is required to prevent the potential divergence. It is also important to note that the polar discontinuity problem itself is not confined only to oxide heterostructures. Essentially the same problem has already been discussed for conventional

[*1] This notation is based on the type of the carriers at these interfaces expected from the polar discontinuity picture.

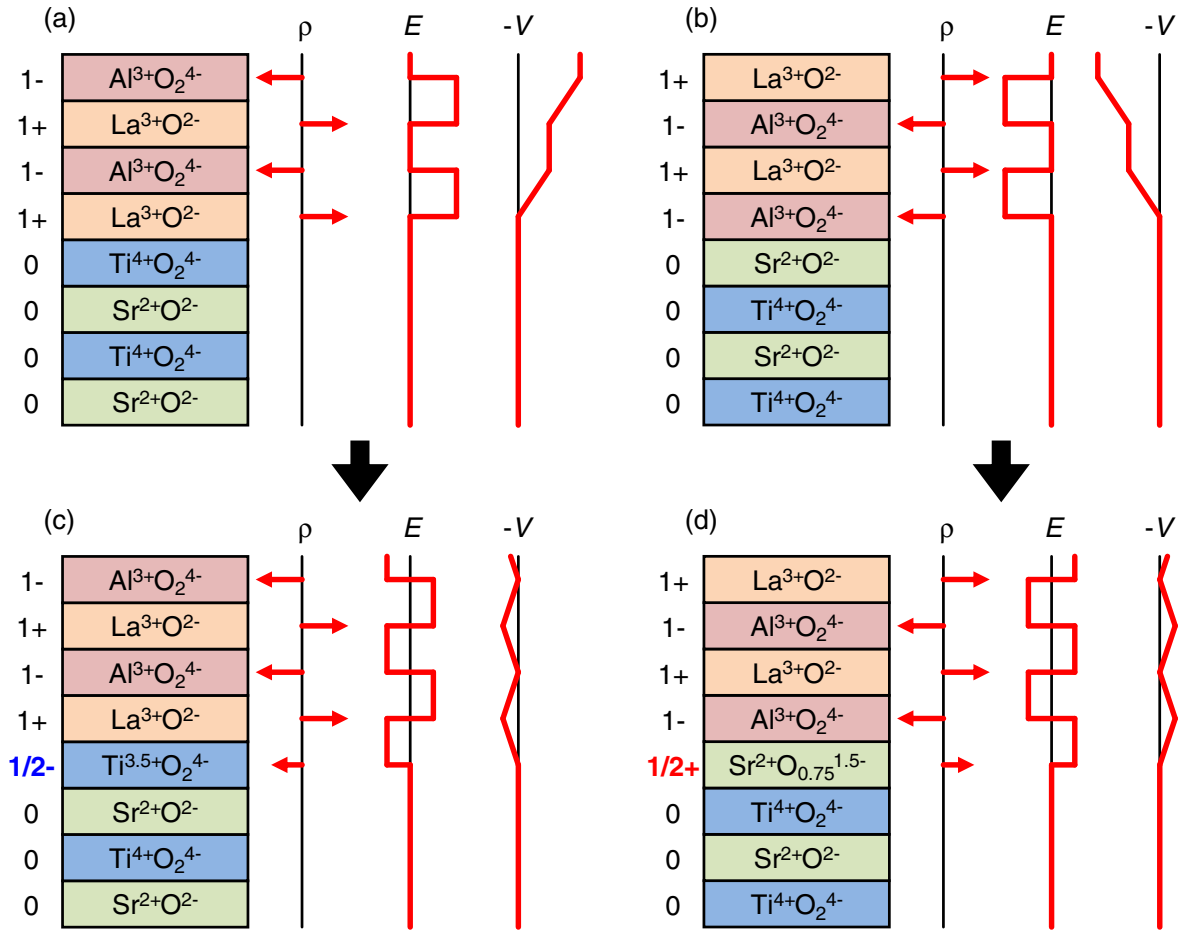

Fig. 2.4 Schematic structure, charge density ρ, electric field E, and electrostatic potential V of the $LaAlO_3/SrTiO_3$ heterostructure. (a) The unreconstructed LaO/TiO_2 interface. (b) The unreconstructed AlO_2/SrO interface. (c) The reconstructed LaO/TiO_2 interface via charge transfer. (d) The reconstructed AlO_2/SrO interface by the formation of oxygen vacancies. Adapted from Ref. [73].

semiconductor heterojunctions [76, 77].

However, the system response to the polar discontinuity problem can be unconventional at the $LaAlO_3/SrTiO_3$ interface. Unlike conventional semiconductors with fixed valence, where stoichiometry change is the only option to resolve the polar discontinuity [76, 77], the multi-valency of transition metal oxides can play an important role at the $LaAlO_3/SrTiO_3$ interface [73]. Specifically, the multiple stable valence states of Ti (Ti^{4+} and Ti^{3+}) may enable electronic reconstructions instead of atomic ones.

At the *n*-type $LaAlO_3/SrTiO_3$ interface, a possible charge rearrangement to resolve this polar problem is that half an electron per two-dimensional unit cell is introduced to $SrTiO_3$, to make the Ti ion at the interface to be $Ti^{3.5+}$, as shown in Fig. 2.4(c). These extra electrons at the *n*-type interfaces can be the origin of the conductivity. Analogous to this, the divergence at the *p*-type interface can be avoided if half a hole per two-dimensional unit cell is introduced to $SrTiO_3$. However, since there is no available mixed-valence state to accept the holes, atomic

reconstructions are preferred, as in conventional semiconductor heterojunctions [76, 77]. The introduction of oxygen non-stoichiometry was observed experimentally [73], preventing the divergence but not contributing to the electrical conduction, as shown in Fig. 2.4(d).

Other possible origins of the conductivity

While the polar discontinuity picture has been supported by some studies, as briefly reviewed in the next Section, other studies have revealed several results that cannot easily be explained purely within the polar discontinuity picture. One representative example is the carrier density modulation by the oxygen pressure during growth [10, 71]. Especially, the sheet carrier density at the *n*-type interfaces can be as high as $\sim 10^{17}$ cm^{-2} when the $LaAlO_3$ film is grown under relatively low oxygen pressures. This value is much larger than half an electron per unit cell ($\approx 3.28 \times 10^{14}$ cm^{-2}), the expected value from the polar discontinuity picture. These results can be explained more simply by oxygen vacancies introduced into the $SrTiO_3$ substrate during growth [78–80].

Several studies have point out that there can be a significant interdiffusion at the $LaAlO_3/SrTiO_3$ interface [81–84]. It has also been suggested that the interdiffusion at the *n*-type interface is thermodynamically favorable [83, 84]. As explained in Sec. 2.2.1, the substitution of La at the Sr site can induce electronic conduction in $SrTiO_3$, and therefore the intermixing can also be the origin of the interface conductivity.[*2]

2.3.3 Controversy about the $LaAlO_3/SrTiO_3$ heterointerface

Advantages of the polar discontinuity picture

An important advantage of the polar discontinuity picture is that it can explain the strong asymmetry between the *n*-type and the *p*-type interfaces, as discussed above. Contrasting to this, the oxygen vacancy picture and the intermixing picture have a great difficulty in explaining this asymmetry. It is highly nontrivial, if not impossible, for only one monolayer of SrO to prevent the $SrTiO_3$ substrate from being reduced, or the cations near the interface from intermixing, so that the *p*-type interface remains insulating.

Another strong point of the polar discontinuity picture is its ability to explain the metal-insulator transition of the $LaAlO_3/SrTiO_3$ interface with film thickness [40]. It has been reported that the *n*-type interface remains unmeasurably insulating when the $LaAlO_3$ thickness is below a critical thickness of 4 unit cells (uc). At 4 uc the conductivity shows an abrupt change, and the interface becomes conducting above that thickness, as shown in Figs. 2.5(a-1) and (a-2) [40]. This transition can be understood by considering the competition between the electrostatic potential in the $LaAlO_3$ film and the energy required for the electronic reconstruction.

This interpretation of the film thickness-driven metal-insulator transition expects that the critical thickness is tunable by "diluting" the polarization of $LaAlO_3$. Reinle-Schmitt *et al.* [85] examined this possibility by growing $(LaAlO_3)_x(SrTiO_3)_{1-x}$ solid solution films on $SrTiO_3$ sub-

[*2] Since the *B*-site in the perovskite structure ABO_3 is enclosed by the oxygen octahedron, it is difficult for the *B*-site cations to move. Thus the Al–Ti interdiffusion is unlikely, which would induce an acceptor-type defect in $SrTiO_3$, reducing the conductivity.

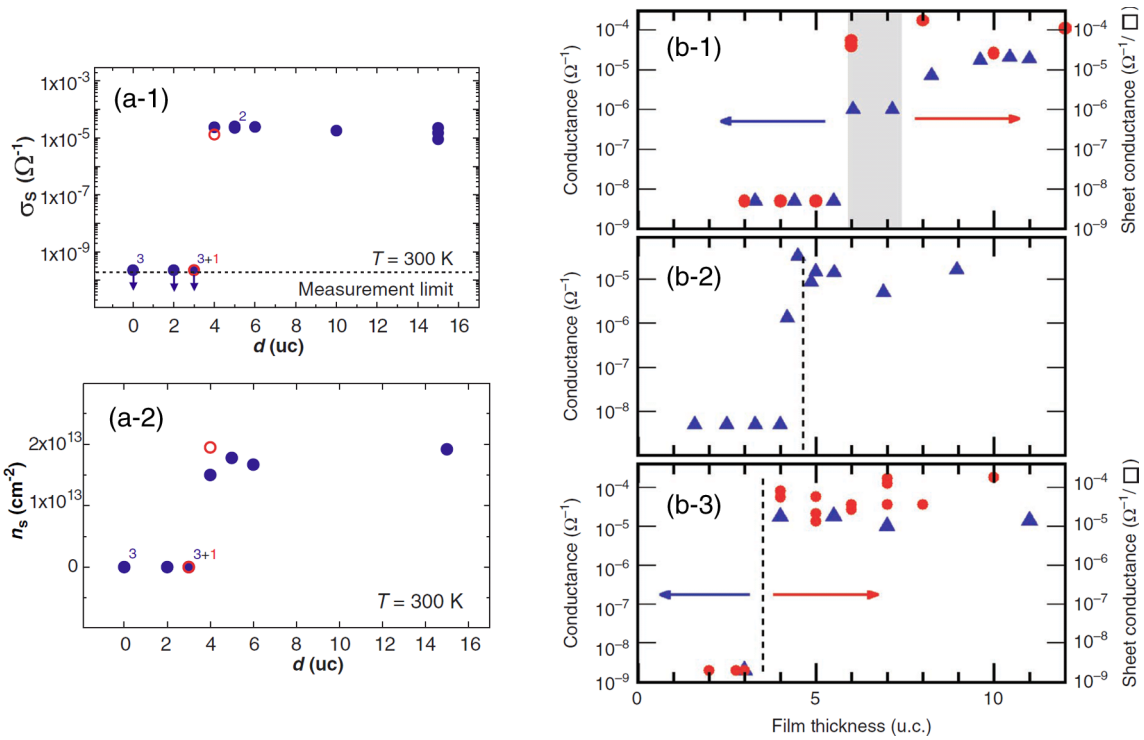

Fig. 2.5 (a) Film thickness dependence of (a-1) the sheet conductance and (a-2) the sheet carrier density of $LaAlO_3/SrTiO_3$ samples grown at 770 °C (solid) and 815 °C (open), respectively. Numbers next to the data points indicate the number of samples with values that are indistinguishable in this plot. From Ref. [40]. Reprinted with permission from AAAS. (b) Film thickness dependence of the sheet conductance of $(LaAlO_3)_x(SrTiO_3)_{1-x}/SrTiO_3$ samples for (b-1) $x = 0.50$, (b-2) $x = 0.75$, and (b-3) $x = 1$. Reprinted by permission from Macmillan Publishers Ltd: Nature Communications [85], © 2012.

strates with varying the fraction x and the thickness, and measuring the interface conductivity. As shown in Figs. 2.5(b-1)–(b-3), their observation shows that with decreasing x, or diluting the formal polarization of the film, the critical thickness for conductivity increases [85]. This tunable critical thickness can be interpreted to further support the polar discontinuity picture.[*3]

Challenges to the polar discontinuity picture

The simple polar discontinuity picture also has weakness in explaining some experimental observations. As mentioned in the last Section, the high electron density in the samples grown under reducing conditions is an important example. The thickness of the conducting channel of those high density samples has been found to be very thick, comparable to the substrate thickness [80, 86]. When postannealed in oxidizing conditions, the conductivity, the carrier density, and the thickness of the conducting channel are strongly reduced [86, 87], or some-

[*3] However, the change of the critical thickness with x is smaller than expected; the simplest calculation expects that the critical thickness should be 7–8 uc for $x = 0.5$, while experimentally it is 6 uc [Fig. 2.5(b-1)]. Reinle-Schmitt *et al.* argue that this is likely due to the uncertainty in the permittivity of the solid solution films [85].

times the interface becomes unmeasurably insulating [80]. These results strongly indicate that, at least for the $LaAlO_3/SrTiO_3$ heterostructure grown in reducing conditions without postannealing treatment, oxygen vacancies induced in the bulk of the $SrTiO_3$ substrate dominate the conductivity.

It has recently been reported that the (110)-oriented $LaAlO_3/SrTiO_3$ heterostructure can also be conducting [88, 89], which also challenges the polar discontinuity picture. Analogous to the [001] direction, the perovskite structure ABO_3 can be described as a stacking of alternating layers of ABO and O_2 in the [110] direction. Notably, the formal net charges of these layers are $+4e$ and $-4e$, respectively, independent of the valence states of the cations. Therefore, in the [110] direction, any two perovskites can be joined without introducing a polar discontinuity [90, 91]. The polar discontinuity picture thus expects no conductivity at the (110) $LaAlO_3/SrTiO_3$ interface, since no electronic (nor atomic) reconstruction is required. Experimentally, however, a few recent studies have found that the (110) $LaAlO_3/SrTiO_3$ interface shows similar conducting properties to those of the *n*-type (001) interface [88, 89], indicating that mechanisms other than the polar discontinuity doping play an important role, at least at the former interface.

The polar discontinuity picture should lead to a significant internal field in ultrathin $LaAlO_3$, as predicted in several theoretical studies [92–94]. However, the existence of the electric field is experimentally unclear: while some experiments support its existence [95, 96], some studies using spectroscopic techniques have found no significant electric field in the $LaAlO_3$ [84, 97]. It is important to note that there may be extrinsic factors preventing the observation of the internal electric field; surface polar adsorbates [98] and electron-hole pairs induced by x-rays [99] can reduce the electric field in $LaAlO_3$.

Due to these controversial issues, the exact origin of the electronic conduction in this system is still under debate. It is likely that multiple contributions exist to varying degrees, which can interact in a highly complex way, depending on the growth details of a given sample [100].

2.3.4 Motivation

As briefly reviewed, there are many conflicting studies and unresolved questions on the $LaAlO_3/SrTiO_3$ heterostructure. In this Thesis, the most basic motivation for the research on this system is to disentangle them, in particular aiming to resolve the origin of the conductivity. As briefly mentioned in the last Chapter, fundamental growth studies are necessary to resolve the controversy. Therefore, in Chap. 4, we first investigate the relationship between the growth and the physical properties of this system, which provides important insights into the origin of the conductivity.

There are many other open questions on the physical properties of the $LaAlO_3/SrTiO_3$ heterostructure. Chapters 5 and 6 are dedicated to tackle such questions, based on the knowledge obtained in Chap. 4. In Chap. 5, we investigate the origin of the discrepancy in carrier densities estimated from the Hall effect and from the quantum oscillations. In Chap. 6, ferromagnetism of this system is characterized in detail, which is also controversial, particularly because it apparently coexists with superconductivity. More specific motivations for these topics are explained at the beginning of each chapter.

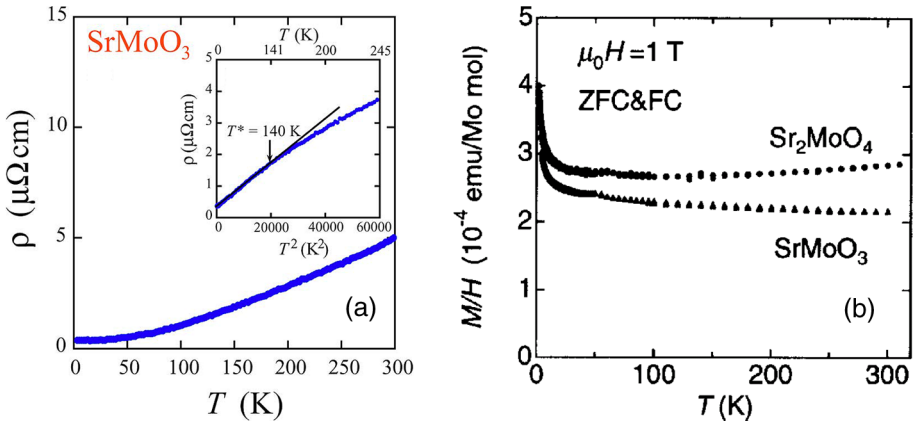

Fig. 2.6 (a) Temperature (T) dependence of the resistivity (ρ) of a $SrMoO_3$ bulk single crystal. Inset: same ρ data plotted as a function of T^2. Reprinted with permission from Ref. [21]. © 2005, AIP Publishing LLC. (b) Magnetic susceptibility of $SrMoO_3$ and Sr_2MoO_4 polycrystals, after diamagnetic corrections, as a function of temperature. Reprinted from Ref. [107], © 2000, with permission from Elsevier.

2.4 $SrMoO_3$ thin films

2.4.1 Bulk properties of $SrMoO_3$: Highest conductivity perovskite oxide

Most perovskite oxides are insulators; even if conducting they are usually "dirty," in the sense that the conductivity is very low compared to normal metals, and correspondingly the mean free path is very short [101]. Such conducting oxides often show complex electronic and magnetic phases with temperature and dopant concentration [102]. Even $SrRuO_3$, a famous example of a relatively good and simple conducting metal oxide, shows a paramagnetic–ferromagnetic phase transition at about 160 K in bulk [103], which affects the electronic properties [104, 105]. In particular, the sign of the Hall effect changes around the transition, whose exact origin is still under debate [106].

In these senses, a "simple good metal" is a rather rare and exceptional category in perovskite oxides. $SrMoO_3$ is an important example of such a simple good metal. It has a cubic perovskite structure with a lattice constant of $a = 3.975$ Å [108, 109]. As shown in Fig. 2.6, it shows a metallic conduction down to low temperature. Most notably, the resistivity is the lowest among oxides: 5.1 μΩ cm at room temperature and ≈ 0.35 μΩ cm at low temperature [21]. It should also be noted that $SrMoO_3$ shows no sign of any magnetic ordering: as shown in Fig. 2.6, it shows Pauli-paramagnetic susceptibility down to 2 K [107]. Recent density-functional calculations also support no magnetism in $SrMoO_3$ [110]. The calculations also show that the density of states near the Fermi level is mainly from the Mo 4d t_{2g} bands, with a small contribution of O 2p due to p–d hybridization, while the unoccupied Mo 4d e_g bands are ≈ 2 eV above the Fermi level [110].

These properties of $SrMoO_3$ indicate that this material is a potentially useful building block

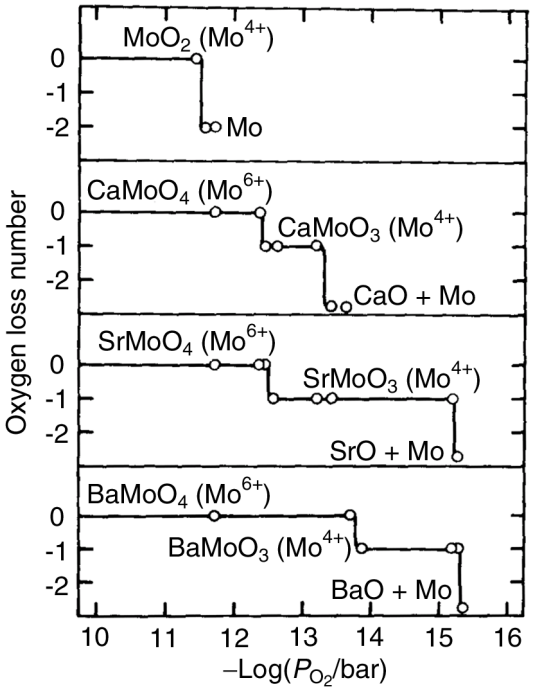

Fig. 2.7 Variation of oxygen content in molybdenum-based oxides with the oxygen partial pressure at 1200 °C. Reprinted from Ref. [117], © 1975, with permission from Elsevier. Re-labeled for clarity.

of complex oxide heterostructures, particularly for device applications. An obvious example is to use it as an electrode; if the electrode metal is ferromagnetic, the device properties may be nontrivially modified via spin injection [111]. It is also important to note that the heterojunction between ferromagnetic and nonmagnetic metals is one of the most fundamental components for spintronic devices [112, 113], while the latter is rare among perovskite oxides.

From a relatively more fundamental perspective, the high conductivity of $SrMoO_3$ indicates that an electronically clean system may be realized using this material. $SrMoO_3$ will also be useful for studying fundamentals of strongly correlated interfaces, e.g., band alignment between a metal and a strongly correlated material, since the simple properties of this material can avoid adding too much complexity at the interface. Interfaces with elemental metals have been extensively studied [114–116], but $SrMoO_3$ has an advantage over them, because an epitaxial interface can be grown, potentially reducing effects of interfacial defects.

2.4.2 Central challenge in growth

Despite the potential interest of $SrMoO_3$, studies of this material are currently very limited. A central challenge is the difficulty in growth that requires extremely strong reducing conditions. Figure 2.7 shows the variation of oxygen content in molybdenum-based oxides with the oxygen partial pressure, indicating the stable valence states of Mo in different thermodynamic conditions [117]. As seen in the figure, $SrMo^{4+}O_3$ can be stabilized only under very low oxygen partial pressures ($\lesssim 10^{-12}$ bar). Note that this result was obtained at a relatively high temper-

ature (1200 °C). At lower temperatures, which are more common for thin film growth, even lower oxygen partial pressure is expected to be thermodynamically required.

While $SrMoO_3$ thin films have been fabricated in spite of this difficulty [118–120], their quality is degraded compared to the bulk single crystal, as indicated by the large difference in the resistivity. In particular at low temperatures, the resistivity of the thin films ($> 10^{-5}\ \Omega\,\mathrm{cm}$) [118–120] is higher than that of the bulk single crystal ($\approx 3.5 \times 10^{-7}\ \Omega\,\mathrm{cm}$) [21] by almost two orders of magnitude. A useful parameter to estimate the quality of a metal known as the residual resistivity ratio[*4] is also smaller for thin films ($\lesssim 2$) than for bulk (≈ 14). The degraded quality of the films prevents detailed studies on this material, in particular by transport measurements.

2.4.3 Motivation

In order to study this potentially interesting material in more detail, it should be important to improve the quality of the thin film. This is first because the thin film will enable more detailed transport measurements; for example, the Hall effect can be measured using the thin film, which is practically impossible with a bulk sample. Growth of high-quality thin films is also important for possible device applications, where heterostructuring with other materials is necessary.

These backgrounds motivated the improvement of the growth of $SrMoO_3$ thin films in this Thesis. Chapter 7 describes how the quality of the film is improved by systematically tuning the growth parameters. The improved film quality enabled a Hall effect measurement, which is also presented in the Chapter.

2.5 Summary

This Chapter presented brief reviews of previous studies on the $LaAlO_3/SrTiO_3$ heterostructure and on $SrMoO_3$, the two systems investigated in this Thesis. The former system is very actively studied, but there still remain many unresolved questions, most notably the origin of the conductivity at the interface. This background motivates a detailed growth study on this system presented in this Thesis. Contrasting to this, studies on $SrMoO_3$ are currently very limited, although this high conductivity metal can be useful especially for device applications. This is likely because of the difficulty in growing this material, in particular thin films. We thus aim to improve the quality of $SrMoO_3$ thin films, which should enable more detailed studies on this potentially interesting material.

[*4] The ratio of the resistivity at room temperature and at low temperature ($\sim$ 2 K). See Chap. 7 for details.

Chapter 3

Experimental Methods

3.1 Outline

In this Chapter, equipment and techniques used throughout this Thesis are reviewed. In this study, samples were fabricated using pulsed laser deposition (PLD; Sec. 3.2). Structural properties of the fabricated samples were characterized by x-ray diffraction (XRD; Sec. 3.3) and atomic force microscopy (AFM; Sec. 3.4). Electrical properties were measured using Physical Property Measurement System (PPMS; Sec. 3.5).

A few other techniques are also used to characterize the samples, but for relatively specific topics only. Therefore, they will be reviewed in each section in which they are used.

3.2 Pulsed laser deposition

PLD is a versatile method with which a wide variety of nanostructures have been fabricated, including oxide thin films with atomic-length scale precision possible in the growth direction [121, 122]. A schematic illustration of our PLD system is shown in Fig. 3.1. The main components of the system are the vacuum chamber, the sample holder, the target holders, the KrF excimer laser, the pressure gauges, and the reflection high-energy electron diffraction (RHEED) monitoring system.

The principle of PLD is as follows (also schematically shown in Fig. 3.1). Intense laser pulses are introduced into the growth chamber and focused onto the surface of the target. Absorbing the energy from the laser pulses, the ablated target material is transformed into a plasma (also known as the “plume”), and the material from the plume is then allowed to recondense on the surface of the substrate, forming thin films.

As investigated throughout this Thesis, there are many growth parameters that are highly influential over the sample properties. In the following sections, the importance of those parameters and their control methods are briefly explained.

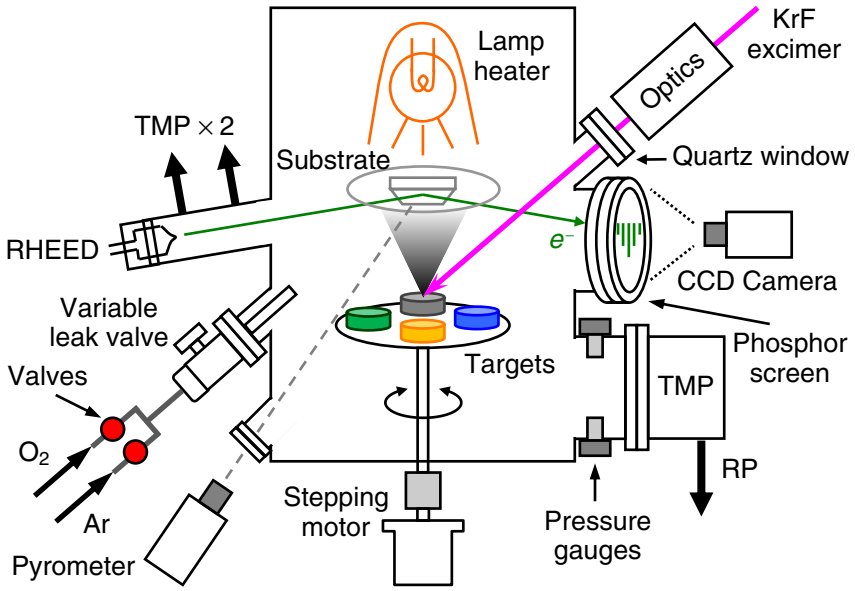

Fig. 3.1 Schematic illustration of the PLD system. TMP: turbo molecular pump, RP: rotary pump, respectively. (Courtesy of Y. Hotta, modified.)

3.2.1 Laser spot size and fluence

Effects of laser parameters on the sample properties are the main issue in Chap. 4, in which the importance of them are explained in detail. The control of the laser spot size and fluence were achieved using the optical systems described below.

The pulsed KrF excimer laser (wavelength = 248 nm, pulse duration time ~ 25 ns) was introduced into the chamber through two different optical systems, as schematically shown in Fig. 3.2. The first system [Fig. 3.2(a)] consists of a variable attenuator, an aperture, and only one lens. The aperture cuts the fringes of the Gaussian beam and defines the shape of the pulsed laser beam. The lens (focal length f = 360 mm) images the laser beam on the target, as the aperture–lens length a and the lens–target length b are set to satisfy the imaging condition $1/a + 1/b = 1/f$.

This imaging mode has an advantage over the focusing mode, as it is not strongly sensitive to the divergence of the laser beam. In principle, the beam can be focused on the target surface just by setting the target surface close to the lens focus, assuming a rectilinear beam – called the focusing mode. However, as the beam inevitably has a finite divergence, the laser profile will be blurred with the focusing mode, reducing the reproducibility. On the other hand, the imaging mode converts the whole laser beam on the image, even with a finite divergence. The laser profile is thus much more reproducible.

The imaging mode usually requires a long optical length,[*1] which may be practically limited

[*1] Considering that typically $a \approx 40$ cm and the magnification $a/b \sim 0.1$, b should be ~ 400 cm: an optical length of several meters is typically required.

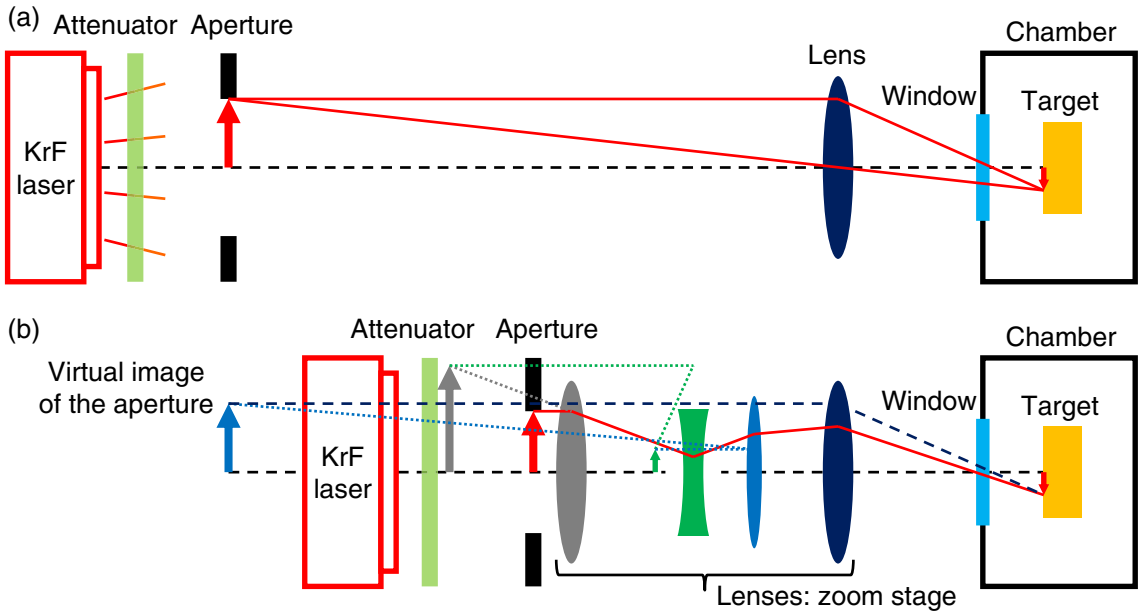

Fig. 3.2 Schematic illustration of the optical systems to image the laser beam (a) without and (b) with the zoom stage. Several additional mirrors used to guide the beam are not shown for clarity. (Courtesy of T. Yajima, modified.)

by space. This problem can be resolved by imaging the laser beam using the afocal "zoom stage," as schematically shown in Fig. 3.2(b). The zoom stage consists of four lenses (focal lengths $f_1 = 360$ mm, $f_2 = -26$ mm, $f_3 = 206$ mm, and $f_4 = 360$ mm). The first three are aligned to make a virtual image of the aperture far behind the real one, which is imaged by the last. This four-lens imaging can simulate the single-lens imaging mode, with saving much of the optical length.

In this study, the latter optical system was employed when the space for the optics was limited. The former was employed when a large space was available for the optical beam path, since the misalignment of the optics was less critical for this system owing to the fewer components. In both cases, the area of the imaged laser spot (A) was controlled by either changing the aperture or moving the optics, or by the combination of the two. The spot size was measured by firing the laser onto a thermosensitive paper placed at the position of the target surface. The laser energy (E) was controlled by rotating the variable attenuator, instead of changing the voltage of the laser source (fixed at 26 kV), in order to avoid changing the divergence of the beam [123].[*2]

The laser energy was measured using a power meter just before the quartz window (*outside* the chamber), and the fluence ($f = E/A$) was calculated. The transparency of the window was taken into the calculation, since the contamination of the window due to the deposited material significantly lowered the laser intensity [123]. The transparency was measured just

[*2] Although the optical systems are in principle not sensitive to the divergence, as explained, the finite misalignment of the optics might still have a small sensitivity to it. Thus it is still helpful to minimize the change to obtain a better reproducibility.

before conducting experiments. The typical degradation in transmittance during single film fabrication was confirmed to be negligibly small ($\lesssim 1\%$).

3.2.2 Temperature and pressure

The substrate temperature (T_{sub}) is an important parameter to control the thermodynamic conditions, as well as the kinetic processes of growth (sticking coefficient and surface mobility of adatoms).

To control the substrate temperature, the Inconel sample holders, on which the substrates were glued with Pt paste and Inconel clamps, were heated by a lamp heater from the backside. The highest temperature available in our system was $\approx$ 1000 °C. The temperature of the attached substrates was monitored by an external infrared pyrometer (CHINO IR-AP). The low measurement limit of the pyrometer was $\approx$ 390 °C.

The oxygen partial pressure ($P_{\mathrm{O_2}}$) is another parameter to control the the thermodynamic conditions. Also, when the ambient gas pressure (density) is high, the ablated species are scattered by the gas molecules before reaching the substrate, and thus the kinetics of the plume is also controlled. Note that the latter effect is not specific to oxygen; by using an inert gas (argon in this study; see also Chap. 7), effects of the scattering can be controlled independently of the thermodynamic conditions.

The oxygen partial pressure (argon partial pressure P_{Ar}) was tuned by introducing high purity oxygen (argon) gas ($>$ 99.9999% purity) into the chamber through a variable leak valve. In order to improve the precision of the control and suppress the effects of other gases which might contaminate the sample, the background pressure in the chamber was kept $\lesssim 10^{-8}$ Torr, often close to 10^{-9} Torr at room temperature (see next Section for details), achieved by the combination of the turbo molecular pump and the rotary pump. The pressure was measured by three different gauges: an ionization gauge ($< 10^{-4}$ Torr), a Baratron gauge ($> 10^{-4}$ Torr), and a quadrupole mass spectrometer (next Section).

3.2.3 Quadrupole mass spectrometer

In order to analyze the base pressure of the chamber in detail, a quadrupole mass spectrometer (qmass; Dycor™ LC series, model LC200MS: AMETEK Inc.) was used, which enabled the measurement of the partial pressure of each gas molecules. The principle of the qmass is schematically shown in Fig. 3.3. The qmass consists of the ionizer, the focus lens, the quadrupole mass filter, the exit lens, and the detector.

The gas molecules are ionized, mostly to have $+e$ charge, by the ionizer, and accelerated by a negative voltage applied on the focus lens, entering the quadrupole. The quadrupole is constructed of four parallel cylindrical rods. A constant direct current (DC) voltage is applied to a pair of opposite facing rods, which has an opposite sign to that applied to the other pair. An alternating radio-frequency (RF) voltage is also applied to the rods. Due to the oscillating electric field created by the quadrupole, only ions with a certain mass-to-charge ratio can reach the exit lens and the detector. By controlling the ratio and the intensity of the DC and RF

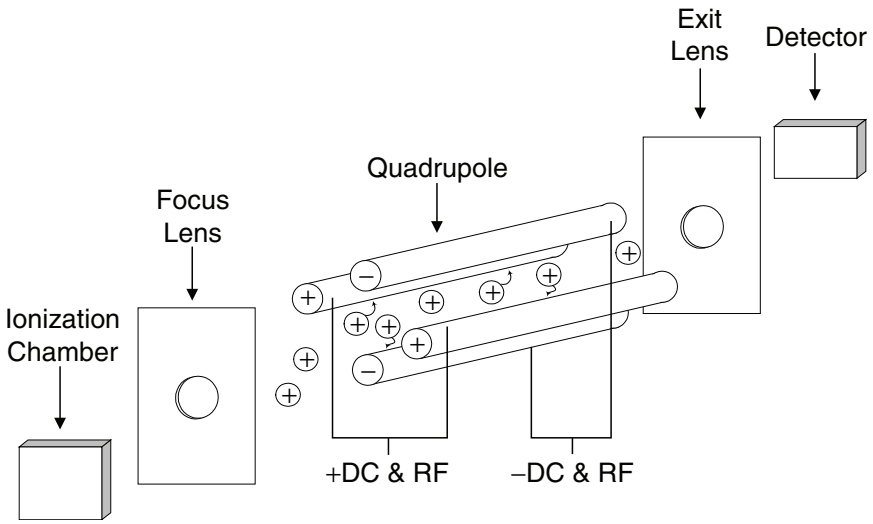

Fig. 3.3 Schematic illustration of qmass. Adapted from Ref. [124].

electric fields, ions with different masses can be detected independently.

Figure 3.4 shows typical qmass data.[*3] As shown in Fig. 3.4(a), the majority of the residual gas is water (H_2O: 18 amu) and nitrogen (N_2: 28 amu) at room temperature. There are also small signals ($< 10^{-9}$ Torr) of oxygen (O_2: 32 amu) and carbon dioxide (CO_2: 44 amu). As shown in Fig. 3.4(b), when the substrate is heated and correspondingly the whole chamber gets hot, the degassing of the chamber becomes stronger and the base pressure increases. In particular, the signals of carbon (C: 12 amu) and its oxides (CO: 28 amu and CO_2), and water significantly increase.

3.2.4 Reflection high-energy electron diffraction

RHEED enables *in situ* monitoring of the growth process, most notably the growth mode and the film thickness [125]. In this study, during the growth, the samples were irradiated by electrons which were emitted from a 25 keV electron gun and focused by electromagnetic lenses. The differential pumping near the electron beam source by two turbo molecular pumps (see Fig. 3.1) enabled the operation of RHEED during high pressure growth up to $\sim 10^{-1}$ Torr [126, 127]. The diffraction patterns of the electrons at the phosphor screen were measured with a high sensitivity CCD camera.

Due to the very small incident angle of the electrons ($\sim 1°$) as well as the strong scattering potential for electrons in solids, almost all of the electrons are diffracted by the topmost atoms at the surface of the sample. Therefore, the diffracted pattern is very surface-sensitive, reflecting the crystal structure and the morphology of the surface [128]. In particular, when the surface is atomically flat, the reciprocal lattice of the well-defined two-dimensional diffraction plane becomes rods, as schematically shown in Fig. 3.5(a). The corresponding RHEED

[*3] The multiplier enabled to obtain a better signal-to-noise ratio, as seen in the figure. Due to the uncertainty in the gain (nominally ~ 100), however, the pressure values measured with the multiplier were in arbitrary units.

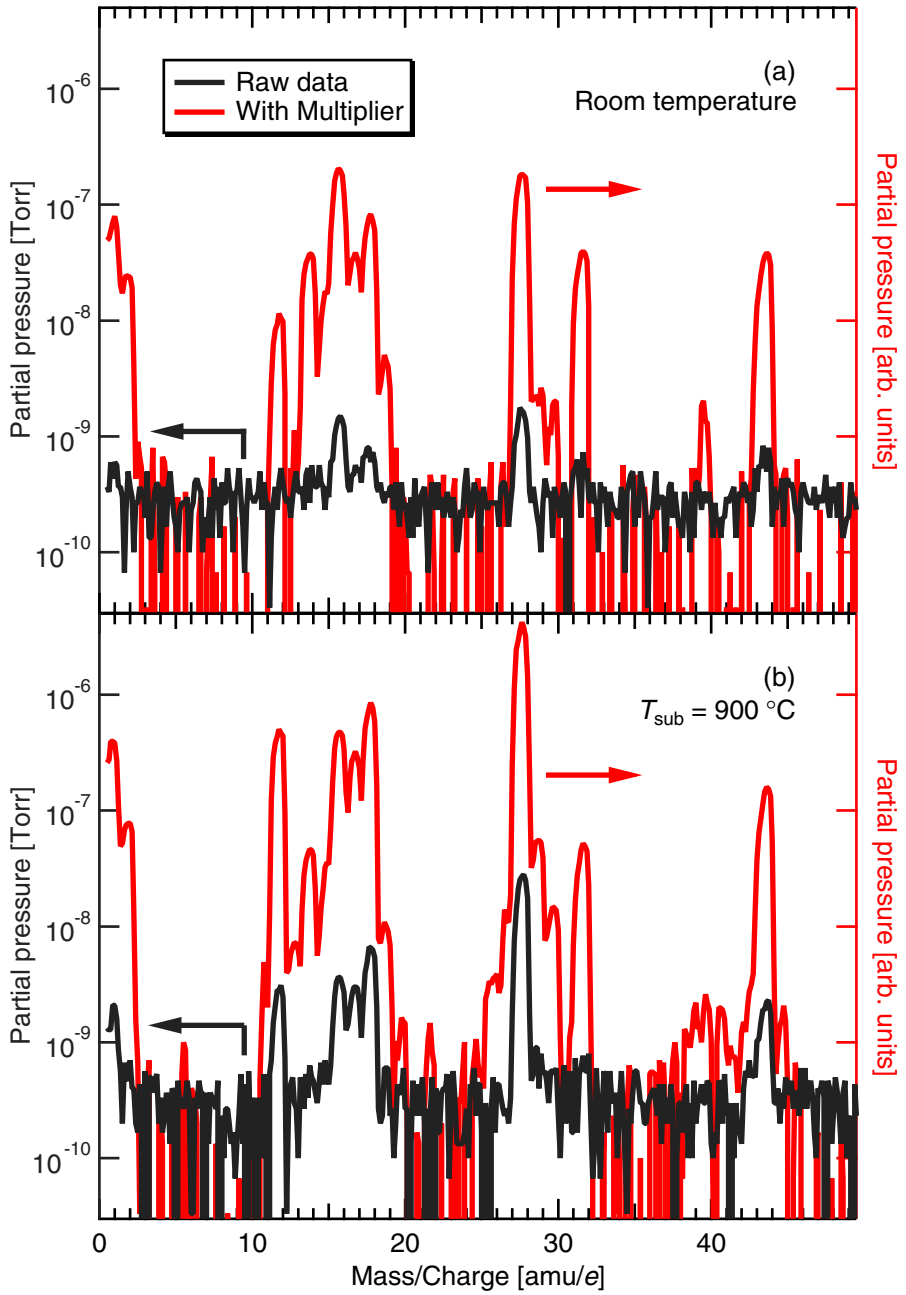

Fig. 3.4 Qmass analysis of the base pressure of the PLD chamber. Partial pressure as a function of the mass-to-charge ratio of gas molecules (a) at room temperature and (b) with the substrate heated to 900 °C. Above 50 amu/e, up to 200 amu/e, no significant signal was observed.

pattern has spots lying on a circle and streaks, the latter originating from the finite broadening of the reciprocal rods, as shown in Fig. 3.5(b). On the other hand, when the surface is rough, the two-dimensional diffraction pattern is weakened and broadened, and the three-dimensional diffraction pattern becomes stronger, as shown in Fig. 3.5(c).

During layer-by-layer growth of the film, the intensity of the RHEED patterns shows oscilla-

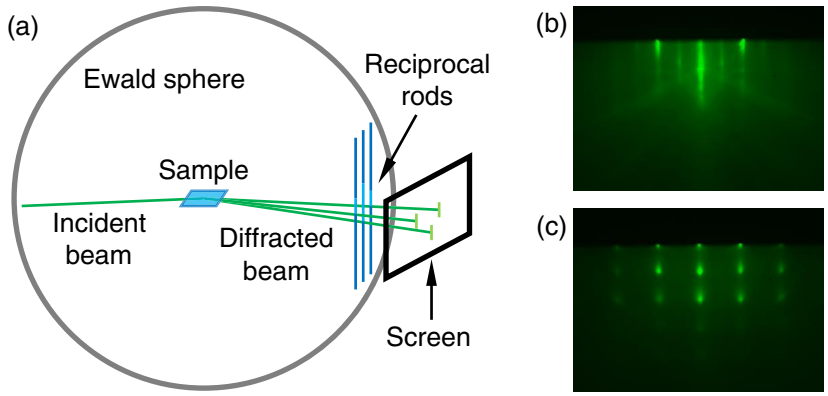

Fig. 3.5 (a) Schematic illustration of the geometry and the mechanism of RHEED. When the sample surface is atomically flat, diffraction spots appear in the direction of intersections between the Ewald sphere and the reciprocal lattice rods. (b) Typical RHEED pattern of a flat surface. (c) RHEED of a rough surface.

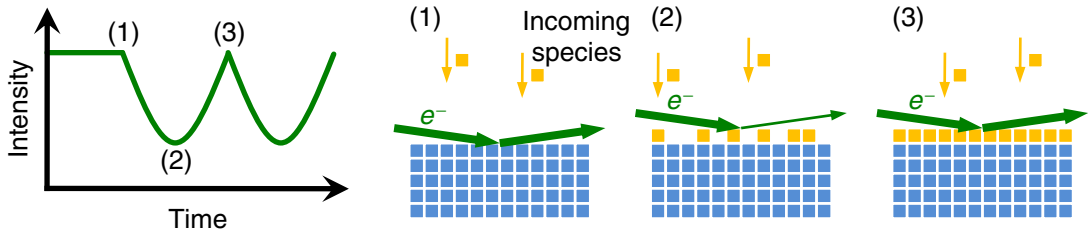

Fig. 3.6 Schematic illustration of the RHEED oscillations during layer-by-layer growth (left) and the corresponding surface structures (right).

tory behavior [129]. This can be understood by considering the change of the surface roughness during growth, as schematically shown in Fig. 3.6. At the beginning of the growth of a monolayer, the initially flat surface is roughened by the material deposited on it. Intuitively, the rough surface induces diffused reflection of the electrons, causing a decrease in the intensity of the RHEED pattern. By further deposition, the surface becomes smoother and correspondingly the intensity begins to increase. On completion of a monolayer of the film, the surface regain its original smoothness and the intensity becomes as strong as the initial state. Repetition of this cycle causes RHEED oscillations; accordingly, RHEED oscillations can be used as a thickness monitor in this growth mode, since ideally each oscillation peak corresponds to the deposition of each monolayer.

In reality, there are many growth modes other than the layer-by-layer one, and the corresponding RHEED oscillations are more complicated [128]. Moreover, it has been pointed out that RHEED oscillations show phase shifts and frequency doubling, depending on the incident angle of the electron beam [130, 131]. Due to these effects, the precise calibration of the film thickness cannot always be achieved only by RHEED. Nevertheless, RHEED still contains much information about the growth mode, and once the relationship between the thickness of the film and each oscillation is confirmed using other methods, such as x-ray diffraction (see

the next Section), transmission electron microscopy, etc, it can be used to determine the film thickness *in situ*.

3.3 X-ray diffraction

XRD is a very widely used method for characterizing crystal structures. In this study, we employed a high resolution XRD system (D8 Discover: Brucker AXS Inc.), where the samples were irradiated by the Cu $K\alpha_1$ line (wavelength $\lambda = 1.54056$ Å) which was screened by a Ge (220) monochromator. Crystal structures were characterized by three different measurement geometries, as described in the following sections. Before that, let us review the basics of XRD in more detail [132].

Mathematically, the intensity profile of diffracted x-rays is related to the Fourier transform of the electron density:

$$I(\boldsymbol{k}) = I_\mathrm{e} \left| \int_\mathrm{matter} \rho(\boldsymbol{r}) \mathrm{e}^{\mathrm{i}(\boldsymbol{k}-\boldsymbol{k}_0)\cdot\boldsymbol{r}} \mathrm{d}^3\boldsymbol{r} \right|^2 \equiv I_\mathrm{e} \left| A(\varDelta\boldsymbol{k}) \right|^2 , \tag{3.1}$$

where $I(\boldsymbol{k})$ is the intensity of the diffracted x-ray with wavevector $\boldsymbol{k}$, I_e is a prefactor, $\rho(\boldsymbol{r})$ is the electron density of the matter at position $\boldsymbol{r}$, $\boldsymbol{k}_0$ is the wavevector of the incident x-ray, and $\varDelta\boldsymbol{k} = \boldsymbol{k} - \boldsymbol{k}_0$. For crystals, where the atoms are periodically arranged and correspondingly $\rho(\boldsymbol{r})$ has a periodicity, $A(\varDelta\boldsymbol{k})$ can be described as

$$\begin{aligned} A(\varDelta\boldsymbol{k}) &= \sum_{l,m,n} \mathrm{e}^{\mathrm{i}\varDelta\boldsymbol{k}\cdot(l\boldsymbol{a}+m\boldsymbol{b}+n\boldsymbol{c})} \int_\mathrm{unit\ cell} \rho(\boldsymbol{r}') \mathrm{e}^{\mathrm{i}\varDelta\boldsymbol{k}\cdot\boldsymbol{r}'} \mathrm{d}^3\boldsymbol{r}' \\ &= G(\boldsymbol{k}) F(\boldsymbol{k}), \end{aligned} \tag{3.2}$$

where $\boldsymbol{a}$, $\boldsymbol{b}$ and $\boldsymbol{c}$ are the translation vectors of the crystal,

$$F(\boldsymbol{k}) \equiv \int_\mathrm{unit\ cell} \rho(\boldsymbol{r}') \mathrm{e}^{\mathrm{i}\varDelta\boldsymbol{k}\cdot\boldsymbol{r}'} \mathrm{d}^3\boldsymbol{r}' \tag{3.3}$$

is the crystal structure factor, and

$$G(\boldsymbol{k}) \equiv \sum_{l,m,n} \mathrm{e}^{\mathrm{i}\varDelta\boldsymbol{k}\cdot(l\boldsymbol{a}+m\boldsymbol{b}+n\boldsymbol{c})}. \tag{3.4}$$

Let L, M and N be the number of unit cells along the $\boldsymbol{a}$, $\boldsymbol{b}$ and $\boldsymbol{c}$ directions, respectively. Then $G(\boldsymbol{k})$ can be described as

$$\begin{aligned} G(\boldsymbol{k}) &= \sum_{l=0}^{L} \mathrm{e}^{\mathrm{i}l\varDelta\boldsymbol{k}\cdot\boldsymbol{a}} \sum_{m=0}^{M} \mathrm{e}^{\mathrm{i}m\varDelta\boldsymbol{k}\cdot\boldsymbol{b}} \sum_{n=0}^{N} \mathrm{e}^{\mathrm{i}n\varDelta\boldsymbol{k}\cdot\boldsymbol{c}} \\ &= \frac{1-\mathrm{e}^{\mathrm{i}L\varDelta\boldsymbol{k}\cdot\boldsymbol{a}}}{1-\mathrm{e}^{\mathrm{i}\varDelta\boldsymbol{k}\cdot\boldsymbol{a}}} \frac{1-\mathrm{e}^{\mathrm{i}M\varDelta\boldsymbol{k}\cdot\boldsymbol{b}}}{1-\mathrm{e}^{\mathrm{i}\varDelta\boldsymbol{k}\cdot\boldsymbol{b}}} \frac{1-\mathrm{e}^{\mathrm{i}N\varDelta\boldsymbol{k}\cdot\boldsymbol{c}}}{1-\mathrm{e}^{\mathrm{i}\varDelta\boldsymbol{k}\cdot\boldsymbol{c}}}, \end{aligned} \tag{3.5}$$

$$|G(\boldsymbol{k})|^2 = \frac{\sin^2(L\varDelta\boldsymbol{k}\cdot\boldsymbol{a}/2)}{\sin^2(\varDelta\boldsymbol{k}\cdot\boldsymbol{a}/2)} \cdot \frac{\sin^2(M\varDelta\boldsymbol{k}\cdot\boldsymbol{b}/2)}{\sin^2(\varDelta\boldsymbol{k}\cdot\boldsymbol{b}/2)} \cdot \frac{\sin^2(N\varDelta\boldsymbol{k}\cdot\boldsymbol{c}/2)}{\sin^2(\varDelta\boldsymbol{k}\cdot\boldsymbol{c}/2)}. \tag{3.6}$$

$|G(\boldsymbol{k})|^2$ is called Laue function. It can be proven that

$$\lim_{L,M,N\to\infty} |G(\boldsymbol{k})|^2 = \delta^3(\Delta\boldsymbol{k} - \boldsymbol{Q}), \tag{3.7}$$

where $\boldsymbol{Q}$ is the reciprocal lattice of the crystal. Therefore, if the crystal is much larger than the penetration depth of the x-ray, the XRD intensity $I(\boldsymbol{k}) = I_e|F(\boldsymbol{k})|^2|G(\boldsymbol{k})|^2$ has finite values only when $\Delta\boldsymbol{k} = \boldsymbol{k} - \boldsymbol{k}_0$ is equal to the reciprocal lattice.[*4]

3.3.1 θ–2θ measurement

Figure 3.7(a) shows the geometry of a XRD θ–2θ measurement. The diffraction profile was measured using a zero-dimensional detector (scintillation counter with a variable slit), which was rotated around the sample while maintaining the relationship $\omega = \theta$ (ω: incident angle of the x-ray to the sample surface,[*5] 2θ: diffraction angle of the x-ray). As seen in the figure, $\Delta\boldsymbol{k}$ is always along the normal of the sample surface, and correspondingly the Laue function is written as

$$|G|^2 = \frac{\sin^2[(\pi/\lambda)\cdot 2Nc\sin\theta]}{\sin^2[(\pi/\lambda)\cdot 2c\sin\theta]}, \tag{3.8}$$

where c is the out-of-plane lattice constant of the sample. $|G|^2$ has maximum values when Bragg's condition is satisfied:

$$2c\sin\theta = n\lambda \quad (n\text{: integer}). \tag{3.9}$$

If the film (thickness $\sim$ 10 nm) is deposited on the substrate (thickness $\sim$ 0.5 mm) maintaining the crystalline orientation, we can observe peaks other than those from the substrate, because of the difference in the out-of-plane lattice constants between the film and the substrate. Therefore, the θ–2θ measurement can tell us that single-crystalline oriented growth of the films has occurred, as well as the out-of-plane lattice constant of the films.

Moreover, the film peaks have an intrinsic broadening and satellite peaks (Laue fringes) because of the finite thickness, which can be used for the thickness estimation. The zero points of $|G|^2$ are given by

$$2t\sin\theta = m\lambda \quad (m\text{: integer}). \tag{3.10}$$

Here $t = Nc$ is the film thickness, which therefore can be determined by

$$t = \frac{\lambda}{2(\sin\theta_m - \sin\theta_{m-1})}, \tag{3.11}$$

where θ_m and θ_{m-1} are the position of the m^{th} and $(m-1)^{\text{th}}$ zero points, respectively. We can also use the local maxima positions instead of the zero points. Also, by approximating the Laue

[*4] In general, $|F|^2$ may become zero at certain reciprocal points and the corresponding reflections are "extinguished" (known as the "extinction rule"). For the perovskites investigated, however, this does not occur.

[*5] *Crystallographic* surface, which was determined using the substrate reflection in the scan area. The *macroscopic* surface is not perfectly parallel to the crystallographic plane due to the inevitable miscut.

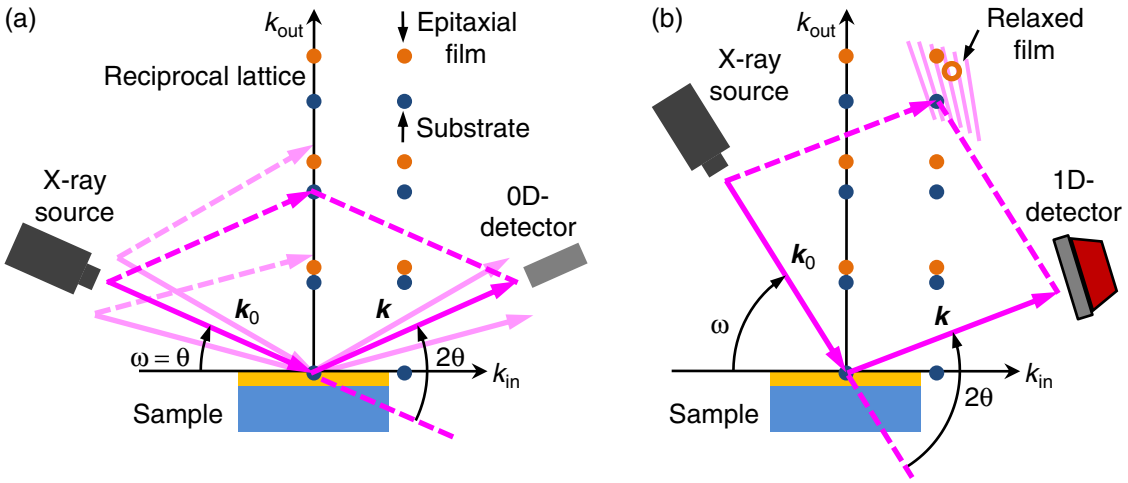

Fig. 3.7 Schematic illustration of the geometry of XRD for (a) θ–2θ measurement and (b) reciprocal space mapping.

function by a Gaussian function, we can deduce Scherrer's formula:

$$\mathrm{FWHM}(2\theta) = \frac{2[(\ln 2)/\pi]^{1/2}\lambda}{t\cos\theta} = \frac{0.94\lambda}{t\cos\theta}, \tag{3.12}$$

where FWHM denotes the full width at half maximum of the peak.

3.3.2 Reciprocal space mapping

While θ–2θ measurement scans only the on-axis peaks, off-axis peaks are also important to characterize the crystal structures, especially the strain state of the film. For off-axis measurement we employed a one-dimensional detector (VANTEC), which can simultaneously detect the diffracted x-ray over a range of 2θ of $\approx 10°$ with a resolution better than 0.01°. The reciprocal space was mapped using the detector by stepping ω with 2θ range fixed, as schematically shown in Fig. 3.7(b). The reciprocal space coordinates k_{in} and k_{out} are calculated by

$$k_{in} = \frac{2\pi}{\lambda}\left[\cos(2\theta-\omega) - \cos(\omega)\right], \tag{3.13}$$

$$k_{out} = \frac{2\pi}{\lambda}\left[\sin(2\theta-\omega) + \sin(\omega)\right]. \tag{3.14}$$

3.3.3 Rocking curve measurement

If the crystal structure of the sample is not perfect, the XRD peaks are broadened, which can therefore be used as a parameter of the crystalline quality. However, as explained in Sec. 3.3.1, the peaks from thin films have an intrinsic broadening along the out-of-plane direction. Therefore, the broadening along the in-plane direction is more useful for the evaluation of the film crystallinity. For on-axis peaks, the diffraction profile along the in-plane direction can be mea-

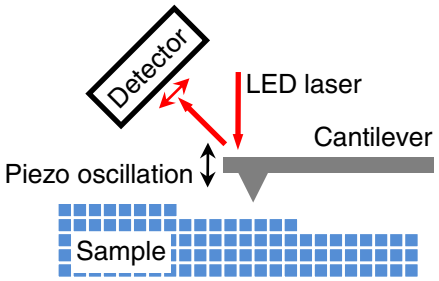

Fig. 3.8 Schematic illustration of AFM.

sured by rocking ω with 2θ locked. This profile is called the rocking curve.[*6] In this study, rocking curves were measured using the same arrangement as for the θ–2θ measurement. The film peak position was determined by the θ–2θ measurement.

3.4 Atomic force microscopy

AFM is a powerful method to investigate the surfaces of various materials [133]. In this study, topographical images of the surfaces of the samples were taken with an AFM (Veeco, Digital Instruments Dimension™) *ex situ*, at room temperature in air, using the "tapping-mode."

As shown in Fig. 3.8, the probe of the AFM is a cantilever with a resonance frequency of $\sim$ 300 kHz. It is oscillated vertically by a piezoelectric device at a frequency $\approx$ 5% away from the resonance frequency. A sharp (length $\lesssim$ 5 μm, end curvature $\lesssim$ 10 nm) tip located at the end of the cantilever moves over the surface of the sample. When the tip is close to the sample, the oscillation of the cantilever is modified by the change of the atomic force between the tip and the sample, which can be detected using a laser reflected from the top of the cantilever. Thus this modification can be converted into a height, resulting a topographical image of the surface of the sample with the two-dimensional rastering of the cantilever.

The root-mean-square (RMS) roughness of the imaged surface is evaluated by

$$\text{RMS roughness} = \sqrt{\frac{\sum_{i=1}^{N} (Z_i - Z_{\text{ave}})^2}{N}}, \tag{3.15}$$

where Z_i is the height at the i^{th} data point, Z_{ave} is the averaged height over the all area, and N is the number of the data points.[*7]

3.5 Physical Property Measurement System

In this study, unless otherwise indicated, transport measurements were carried out in a PPMS (Quantum Design Inc.), where the range of temperature (T) from 2 K to 400 K and the range

[*6] In general, rocking curve measurement is not only for the on-axis peaks. For off-axis peaks, however, the scan direction is not along the in-plane direction.

[*7] In this study, the scan area typically has $N = 512 \times 512 = 2^{18} = 262114$ data points.

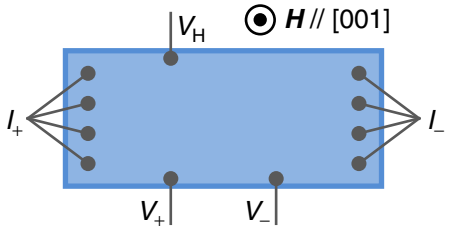

Fig. 3.9 Schematic illustration of the normal geometry of transport measurements.

of magnetic field ($\mu_0 H$; μ_0 is the vacuum permeability) from 0 T to ±14 T were available. The precision of the temperature was better than 0.5%, that of the magnetic field better than $\pm 10^{-3}$ T.

The longitudinal and the Hall resistances (R_{xx} and R_{xy}) were measured with a standard Hall bar geometry using the four-probe method, as schematically shown in Fig. 3.9, which is widely used to exclude the contact resistance. The resistance bridge of the PPMS was employed for these measurements, where the current direction was switched with a repetition rate of ≈ 7.5 Hz to exclude the effect of the possible DC offsets of voltage. The electrodes were created by bonding Al wire with an ultrasonic wirebonder (Model 7476D: West Bond Inc.).

Due to the inevitable imperfection in the electrode geometry, there was a practical problem with directly extracting R_{xx} and R_{xy}. Details of the problem and the data treatment to solve it are explained in App. A.

Chapter 4

Stoichiometry Control of the Electronic Properties of the $LaAlO_3/SrTiO_3$ Heterointerface

4.1 Introduction

4.1.1 Sensitivity of growth control

As reviewed in Sec. 2.3, the discovery of a conducting layer formed at the interface between the wide band gap perovskite insulators $LaAlO_3$ and $SrTiO_3$ [10] has led to extensive research on this system. Several scenarios have been proposed to explain the origin of the conductivity: an electronic reconstruction driven by the polar discontinuity between the (001) interfaces of polar $LaAlO_3$ and nonpolar $SrTiO_3$ [73], the formation of oxygen-deficient $SrTiO_{3-\delta}$ during growth [78–80], or atomic diffusion near the interface to create conducting $La_xSr_{1-x}TiO_3$ layers [81–84]. All are possible contributing mechanisms which are not mutually exclusive, and can interact in a highly complex way [100].

In order to disentangle these effects, a central challenge experimentally is to understand the sensitivity of the properties of this system to all of the standard control parameters in thin film growth, as partly reviewed in Sec. 2.3.3. These include the oxygen partial pressure [10, 71], the post-annealing treatment [86, 87], the growth temperature [70], and the $LaAlO_3$ thickness [40, 87, 134]. The latter effect, in particular the existence of a critical thickness of 3–4 uc required for conductivity [40], can be interpreted to support the polar discontinuity picture. However, it is clear that there are other, larger, characteristic thicknesses which also influence the conductivity [87, 134], indicating the need of more detailed considerations. The strong asymmetry between the *n*-type and *p*-type interfaces, in particular the insulating nature of the latter [10, 72] as well as the structural differences [73, 135], not only emphasize the importance of the atomic scale details, but also imply that oxygen vacancies and intermixing are not the sole cause of the conductivity.

4.1.2 Importance of laser parameters

In the case of PLD, the character of the ablating laser itself is well known in oxides to be crucial to obtain precisely controlled film stoichiometry. For example, Dam *et al.* [15] have demonstrated that the cation ratio of PLD-grown $SrTiO_3$ films can be controlled by the laser fluence. As shown in Fig. 4.1(a-1), the composition of the target surface is off-stoichiometric after growth under certain laser conditions, Ti rich in this case, indicating that Sr has been preferentially ablated [Fig. 4.1(b)] and thus a Sr rich film has likely been grown. They have also found that the cation ratio of the $SrTiO_3$ film has a lateral distribution, which is also fluence dependent, as shown in Fig. 4.1(a-2), indicating that the distributions of Sr and Ti in the plume are different from each other [Fig. 4.1(c)].

This stoichiometry modulation has a strong impact on the film properties. For example, Ohnishi *et al.* [17] have found that the conductivity of Nb-doped $SrTiO_3$ thin films is strongly suppressed by cation off-stoichiometry, due to trapping and scattering of the electrons by cation vacancies. It should be noted that the cation off-stoichiometric $SrTiO_3$ films show lattice expansion, as shown in Fig. 4.1(d-1). This is caused by Coulomb repulsion near the cation vacancies, which modify the local charge distribution, as schematically shown in Fig. 4.1(d-2). Note that in order to accept off-stoichiometry in perovskite oxides, it is energetically most favorable in general to induce vacancies. Due to the tightly packed lattice structure and the difference of the crystal field between the *A*- and *B*-sites, other defects are often highly energetically unfavorable.[*1]

In contrast, highly-reduced $SrTiO_3$ bulk single crystals show no detectable change of the lattice constant [139, 140], indicating that the oxygen vacancies (anion off-stoichiometry) do not contribute to the lattice expansion. This asymmetric behavior between the cation and anion vacancies can be understood by considering that the oxygen vacancies in $SrTiO_3$ is a donor-type defect (see Sec. 2.2). The induced free electrons can screen the Coulomb repulsion near the oxygen vacancies, counteracting the lattice expansion.

The importance of the character of the ablating laser is a general issue for all PLD-grown oxide films. Stoichiometry modulation and its effect on the film properties have been reported for many other oxide systems, for example for cuprates [16] and manganites [18]. Therefore, it is essential to clarify the effect of the laser parameters on the $LaAlO_3/SrTiO_3$ heterostructure, namely, $LaAlO_3$ cation stoichiometry, structure, and the interfacial electronic character.

However, there is an important difference between the previous studies and the case of $LaAlO_3/SrTiO_3$: as reviewed in Sec 2.2, $LaAlO_3$ is electrically an insulator over a wide stoichiometry range, particularly at low temperatures [64]. This indicates that *a priori* the influence of stoichiometry variations of the $LaAlO_3$ on the conductivity in the underlying $SrTiO_3$ substrate is rather indirect, compared to the typical optimization of electronic properties of conducting

[*1] However, sometimes vacancies are also not favorable, and the cation off-stoichiometry induces some non-perovskite phases. In the case of $SrTiO_3$, for example, Ti vacancies are known to be energetically unlikely [136], and Ruddlesden-Popper defects [137] and Sr segregation [138] are more favorable.

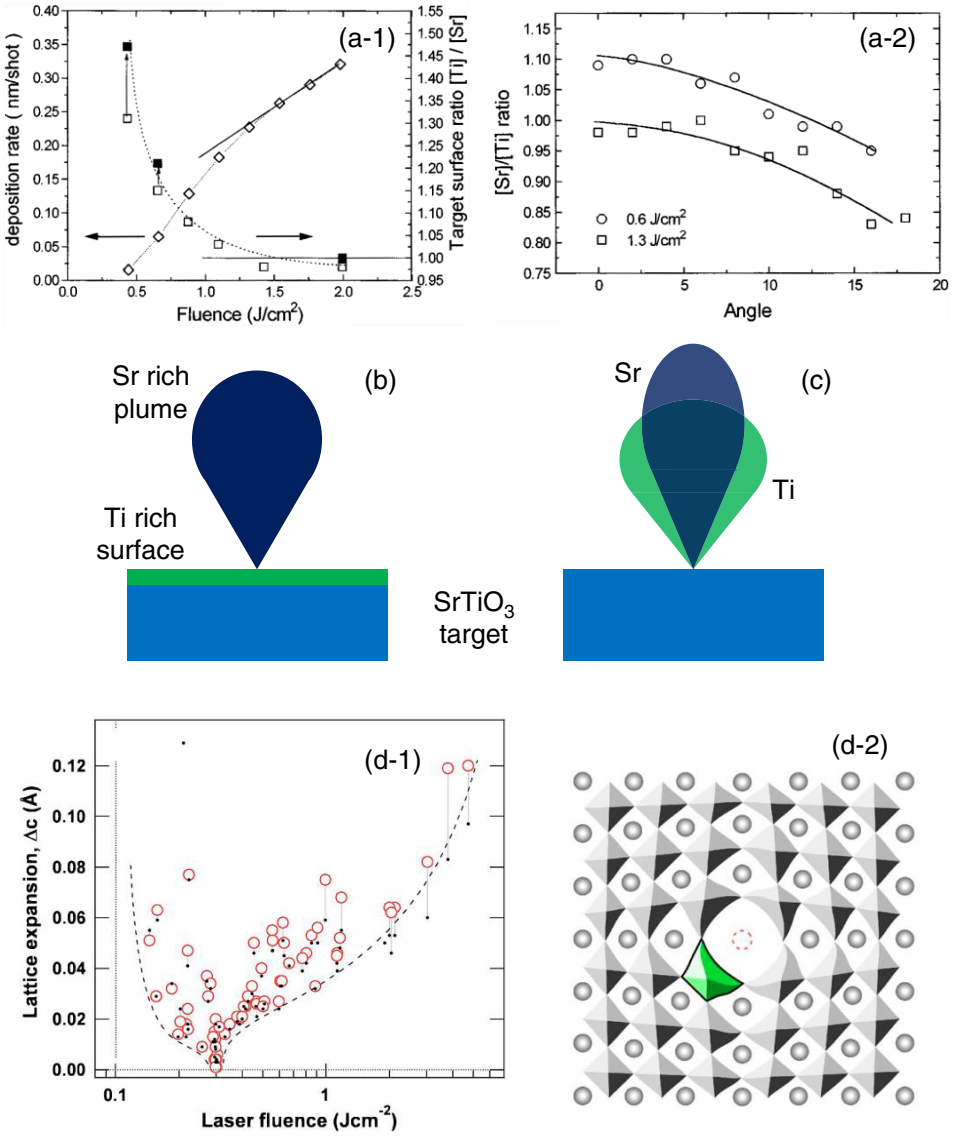

Fig. 4.1 (a-1) Deposition rate of the $SrTiO_3$ films (diamonds) and the [Ti]/[Sr] composition ratio of the target surface (open squares: after 1400 shots, solid squares: after 10000 shots) as a function of the laser fluence, and (a-2) lateral distribution of the [Ti]/[Sr] composition ratio. Reprinted with permission from Ref. [15]. © 1998, AIP Publishing LLC. (b) Schematic illustration of the incongruent ablation. (c) Different distributions of the ablated species. (d-1) Lattice expansion of $SrTiO_3$ thin films as a function of the laser fluence (dots: as-grown, open circles: after air-annealing), and (d-2) schematic illustration of the Sr vacancy, expanding the lattice due to Coulomb repulsion. Reprinted with permission from Ref. [17]. © 2008, AIP Publishing LLC.

thin films by directly tuning their own cation ratio. Still, it is quite possible that the above scenarios used to explain the interface conductivity can be significantly impacted by a change in the $LaAlO_3$ stoichiometry.

In this Chapter, we report the film stoichiometry, lattice structure, and electronic properties of various $LaAlO_3/SrTiO_3$ heterostructures with $LaAlO_3$ grown using different laser fluences, demonstrating a dramatic influence on the interface conductivity. The La/Al ratio in the $LaAlO_3$ films grown in different laser conditions was varied over a wide range from 0.88 to 1.15, and was found to have a strong effect on the interface conductivity, as presented in Sec. 4.3. In particular, the carrier density was modulated over more than two orders of magnitude, following one functional control parameter – the $LaAlO_3$ lattice constant. As discussed in Sec. 4.4, these results can be understood to arise from the variations in the electrostatic boundary conditions, and their resolution, with $LaAlO_3$ stoichiometry.

The work presented in this Chapter, except the Rutherford backscattering spectrometry result (Sec. 4.3.2), is published in Ref. [141].

4.2 Experimental details

The samples were fabricated by PLD (Sec. 3.2). The laser repetition rate was fixed at 2 Hz, unless otherwise indicated. For the XRD and transport measurements, each $LaAlO_3$ film was grown on a 5×5 mm^2 $SrTiO_3$ (001) substrate with a TiO_2-terminated surface [74, 75], which was commercially available (Shinkosha Co.). The variable growth parameters were: the laser spot size A, the laser energy E, and the laser fluence $f = E/A$. The laser beam was imaged to a rectangular spot on the single crystal $LaAlO_3$ target using the zoom stage (Sec. 3.2.1). Before growth, the substrates were preannealed at substrate temperature $T_{sub} = 950$ °C in oxygen partial pressure $P_{O_2} = 5 \times 10^{-6}$ Torr for 30 mins. Following this anneal, T_{sub} was reduced to 800 °C and P_{O_2} was increased to 1×10^{-5} Torr, the film growth conditions. The $LaAlO_3$ film thickness was 25 uc, as monitored using the *in situ* RHEED (Sec. 3.2.4). After growth, the samples were cooled to room temperature in $P_{O_2} = 300$ Torr, with a one hour pause at $T_{sub} = 600$ °C. These growth details (other than the laser parameters) are the same as used previously [134].

The out-of-plane lattice constant of the $LaAlO_3$ films (c_{LAO}) was evaluated using the (002) peak of the XRD θ–2θ scans (Sec. 3.3.1). The transport measurements were carried out in a PPMS, as described in Sec. 3.5. The cation stoichiometry of the $LaAlO_3$ films was measured by inductively coupled plasma (ICP) spectrometry, using $\sim$ 400 nm thick amorphous $LaAlO_3$ films grown on 10×10 mm^2 B-doped Si substrates at room temperature.[*2] For these samples, in order to obtain the necessary thick films in a practical time, the repetition rate of the laser was increased to 10 Hz, while P_{O_2} and the laser conditions were the same as used for the epitaxial growth.

[*2] Measured by Hitachi Kyowa Engineering Co., Ltd. The Si substrates were employed for a technical issue of ICP related to the chemical solubility.

Table. 4.1 Cation ratio from ICP and out-of-plane lattice constant of $LaAlO_3$ films grown at different laser conditions. Published in Ref. [141].

Fluence f (J/cm^2)	Spot area A (mm^2)	La/Al atomic ratio	c_{LAO} (Å)
0.7	3.0	0.984	3.726
0.7	4.3	0.969	3.735
0.7	5.6	0.996	3.737
0.9	3.0	0.965	3.733
1.1	3.0	0.957	3.739
1.1	3.5	0.908	3.749
1.3	2.5	0.883	3.753
1.3	3.0	0.946	3.742
1.6	2.5	1.155	3.763
1.6	3.0	0.992	3.748
1.9	2.5	1.037	3.758

4.3 Effect of the laser parameters on $LaAlO_3/SrTiO_3$

4.3.1 Evaluation of $LaAlO_3$ film stoichiometry

$LaAlO_3$ films were grown using a total of 11 different laser conditions, as summarized in Table 4.1, which also shows the cation ratios from ICP and c_{LAO} from the XRD measurements. The La/Al ratio was varied from 0.883 to 1.155, a range of more than ±10%, comparable to values reported for other similar systems [16–18]. Two of the films were La rich, while the remaining were La poor to varying degrees, including two samples which were within 1% of La/Al = 1. As shown in Fig. 4.2(a), c_{LAO} increased with increasing the laser fluence. As briefly reviewed in Sec. 4.1.2, the c_{LAO} expansion indicates that the $LaAlO_3$ films are off-stoichiometric, since cation vacancies in insulating films cause lattice expansion due to Coulomb repulsion [17]. We note that the formation of interstitial or anti-sites defects is energetically unlikely [142].

The c_{LAO} expansion is confirmed to be consistent with the ICP result: as shown in Fig. 4.2(b), c_{LAO} increases for both the La rich and La poor films, relative to La/Al = 1, where we estimate c_{LAO} = 3.72 Å. The estimated c_{LAO} of the stoichiometric $LaAlO_3$ film is in good agreement with calculations of the Poisson ratio [143], assuming a tensile strain by the $SrTiO_3$ substrate. Theoretical calculations show that the formation energy of (V_{Al}''' + $\frac{3}{2}V_O^{\bullet\bullet}$) is larger than that of (V_{La}''' + $\frac{3}{2}V_O^{\bullet\bullet}$) in a wide range of the La-O-Al ternary phase diagram [142] (here we follow the notation of Kröger and Vink [144]), which qualitatively explains why most growth conditions result in La poor films. It is also suggested that V_{Al}''' produce larger atomic relaxations as compared to those from V_{La}''' [142], which may explain the asymmetry about La/Al = 1. Interestingly, there are two films which are nearly stoichiometric from ICP, but show nontrivial

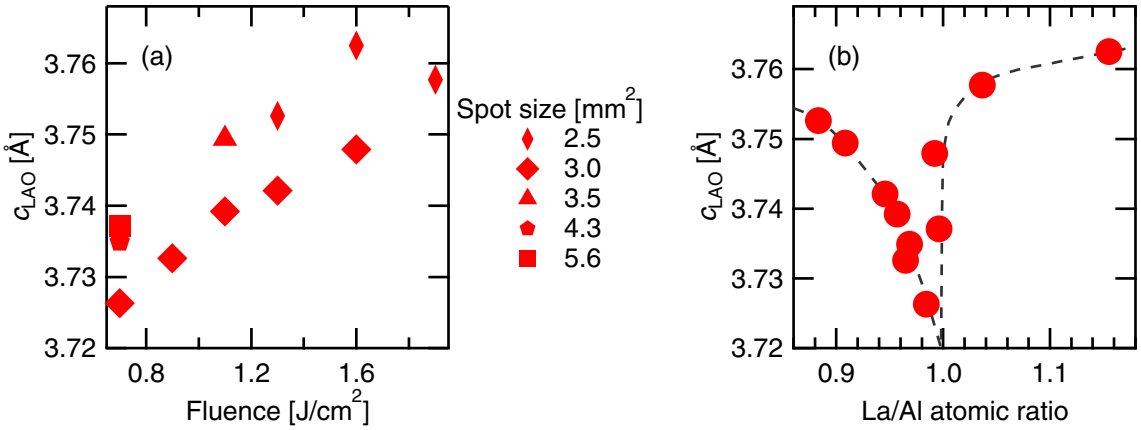

Fig. 4.2 (a) Out-of-plane lattice constant of the epitaxial $LaAlO_3$ films as a function of laser fluence. (b) c_{LAO} as a function of the cation ratio obtained from the amorphous $LaAlO_3$ films grown at the same laser conditions. Dashed curve is a guide to the eye. Published in Ref. [141].

expansion of c_{LAO}, which cannot be explained within the above scenario. A likely interpretation is that both La and Al vacancies are kinetically induced in equal amounts at these conditions [142], and the oxygen content differs between the two.

4.3.2 Possible effect of other growth parameters

While ICP is known as an element-selective and highly quantitative chemical characterization method, care is needed due to the fact that the ICP results were obtained from the films grown at room temperature. The measurement on the amorphous films cannot take into account the possible effects of strain and the difference of the sticking coefficient between La and Al at elevated temperatures. The strong and expected relationship between the ICP and XRD results [Fig. 4.2], the latter directly characterizing the $LaAlO_3/SrTiO_3$ samples, suggests that these factors do not strongly affect the $LaAlO_3$ stoichiometry. Nevertheless, it is important to quantitatively confirm the validity of the ICP measurement on the films grown in the different condition.

In order to quantify the possible effect of other growth parameters, $LaAlO_3$ stoichiometry was evaluated also by Rutherford backscattering spectrometry (RBS). For the RBS measurement, a $\approx$ 40 nm $SrTiO_3$ buffer layer was grown on a MgO (001) substrate prior to $LaAlO_3$. A $\approx$ 40 nm $LaAlO_3$ film was grown on the buffer, in the identical condition to that for the $LaAlO_3/SrTiO_3$ samples, contrasting to the ICP samples. The laser parameters were $f = 0.7$ J/cm^2 and $A = 3.0$ mm. ICP indicates that $LaAlO_3$ grown at this condition has a cation ratio of La/Al = 0.984 [Table 4.1]. The $SrTiO_3$-buffered sample structure enables a better resolution for Al, which otherwise cannot be well resolved from the substrate signal [145]. Preparation of the $SrTiO_3/MgO$ sample and the RBS measurement were performed by Mr. Shaobo Zhu and Prof. Darrell G. Schlom (Cornell University, USA).

Figure 4.3 shows the RBS spectrum of the sample. Thanks to the well separated peaks of

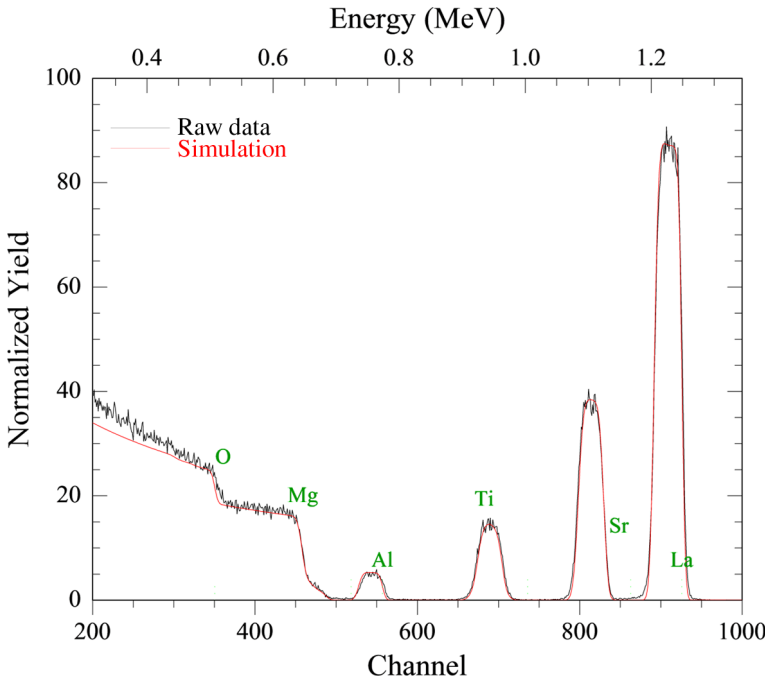

Fig. 4.3 (black line) RBS spectrum of the $LaAlO_3/SrTiO_3/MgO$ (001) sample (see text for details). (red line) Simulation for the data, giving a cation ratio of La/Al = 0.96 ± 0.03. Courtesy of S. Zhu and D. G. Schlom (Cornell University, USA).

different elements, in particular the well defined Al peak, the error bar on the composition calibration is small. The simulation of the spectrum gives a cation ratio of $La/Al = 0.96 \pm 0.03$, in good agreement with ICP (0.984). The slightly higher La deficiency, although within the error bar, suggests that the sticking coefficient of La at high temperatures is smaller compared to that of Al.

4.3.3 Effect on the electronic properties at the interface

We next examined the effect of the $LaAlO_3$ film stoichiometry, modulated by the laser parameters, on the electronic properties of the $LaAlO_3/SrTiO_3$ interface. In Fig. 4.4 we show representative examples of the film stoichiometry dependence of the interface conductivity. All of the samples show an upturn in the resistance at low temperatures, qualitatively consistent with previous reports [87, 134]. With increasing film off-stoichiometry, the sheet resistance becomes larger at all temperatures, and the upturn at low temperatures becomes more dramatic. In the following we focus on the sheet carrier density (n_s) at 100 K, since at this temperature the resistance of all the samples was low enough to obtain clear Hall effect data sets, with an estimated maximum error bar of $\lesssim 10\%$. Also, the Hall effects at this temperature were fully linear to the highest measured fields (8 T).

Figures 4.5(a) and (b) show $n_s(100\ K)$ of the $LaAlO_3/SrTiO_3$ samples as a function of the $LaAlO_3$ cation ratio from ICP and c_{LAO}, respectively. There is a clear and significant relationship between the film stoichiometry, the lattice constant and the carrier density. Despite some

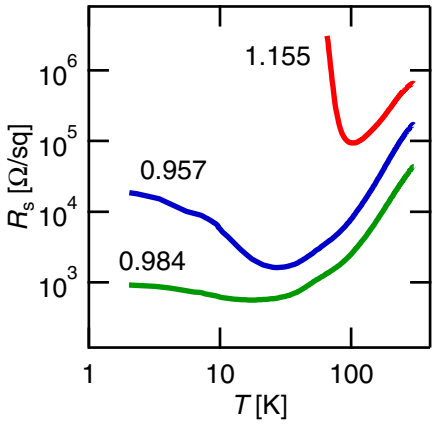

Fig. 4.4 Temperature dependence of the sheet resistance of the $LaAlO_3/SrTiO_3$ samples with different film cation ratios. Numbers indicate the La/Al atomic ratio from ICP. Published in Ref. [141].

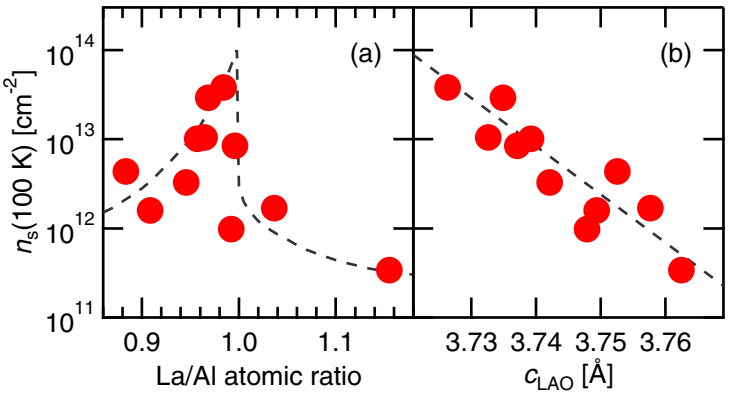

Fig. 4.5 Sheet carrier density of the $LaAlO_3/SrTiO_3$ samples at 100 K as a function of (a) the cation ratio from ICP and (b) the out-of-plane lattice constant of the $LaAlO_3$ films. Dashed curves are guides to the eye. Published in Ref. [141].

scatter, the samples with more off-stoichiometric films are found to have smaller n_s [Fig. 4.5(a)]. Most notably, as shown in Fig. 4.5(b), all the carrier densities are simply scaled with the film lattice constant over more than two orders of magnitude, independent of which cation(s) is (are) deficient.

4.4 Discussion

Next, we discuss the possible mechanisms that may explain these results. The observed smaller carrier density for cation off-stoichiometric samples [Fig. 4.5] is not consistent with a simple picture of intermixing, since the film off-stoichiometry should enhance the cation diffusion from the substrate to the film, creating more room for La ions to diffuse to the substrate, and enhance conductivity. The data are also not consistent with a simple picture of oxygen vacancies by gettering from $SrTiO_3$, since this would tend to increase with the density of vacancies caused

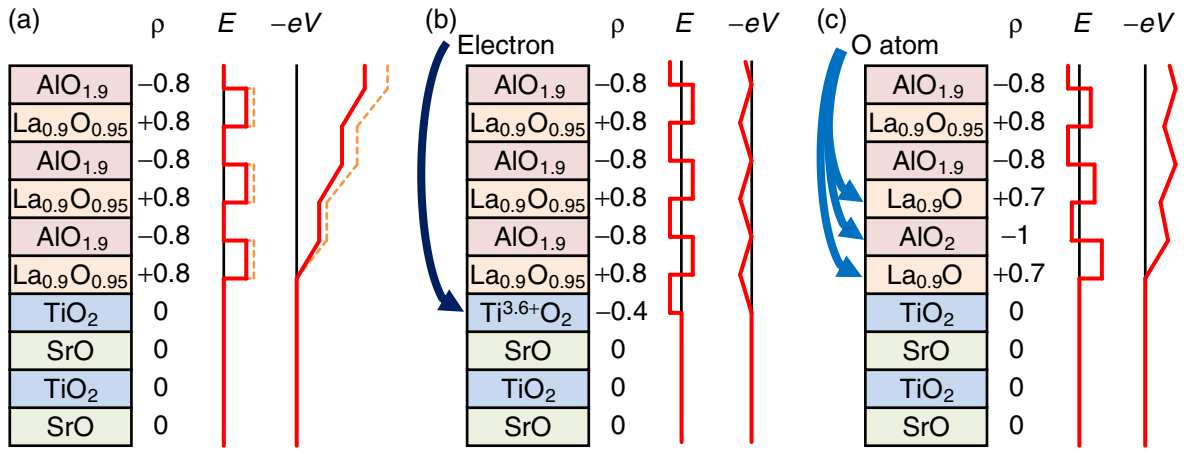

Fig. 4.6 Schematic structure, charge density ρ, electric field E and electrostatic potential $-eV$ of the $La_{0.9}AlO_{3-\delta}/SrTiO_3$ (001) heterostructure. (a) Unreconstructed structure with oxygen vacancies equally distributed amongst all oxygen sites. Dashed lines denote E and $-eV$ of the stoichiometric structure. (b) Possible reconstruction via charge transfer, which induces less electrons than in the stoichometric structure. (c) Atomic reconstruction via stoichometry change, which resolves the polar problem without doping electrons to the substrate. Published in Ref. [141].

by cation off-stoichiometry in $LaAlO_3$. Similarly, blocking of reoxidation from molecular O_2 by the $LaAlO_3$ should decrease as the $LaAlO_3$ thickness decreases, while experimentally we find that at fixed laser conditions, thinner films show higher conductivity. Thus we focus on the role of the electrostatic boundary conditions.

For simplicity, we consider the 10% La deficient case, $La_{0.9}AlO_{3-\delta}/SrTiO_3$, as shown in Fig. 4.6. Since La vacancies are negatively charged, it would be natural to assume that the off-stoichiometric $LaAlO_3$ film also has positively charged oxygen vacancies in order to maintain bulk charge neutrality. Despite the uncertainty in the exact density of the oxygen vacancies on each layer, here we illustrate the simplest case in which the oxygen vacancies are equally distributed amongst all the oxygen sites. In this case, the absolute values of the charge density of each layer becomes smaller [Fig. 4.6(a)], similar to $(LaAlO_3)_x(SrTiO_3)_{1-x}$ solid solution films [85]. Therefore, while there still remains a polar discontinuity, the extra charge required to resolve it is less than that in the stoichiometric structure, as schematically shown in Fig. 4.6(b).

Another important point is that the electronic reconstruction is not the only option for resolving the polar problem. Atomic reconstruction is also possible, as in conventional semiconductor heterojunctions [77] and at the *p*-type $LaAlO_3/SrTiO_3$ interface [73]. In the case of the *p*-type interface, the extra positive charge required for resolving the polar problem are provided by oxygen vacancies [73]. Analogous to this, the extra negative charge required at the *n*-type interface may be provided by *excess* oxygen. If the $LaAlO_3$ film is fully stoichiometric, there is no room to accept the excess oxygen, given the tightly packed perovskite structure, and it is highly energetically unfavorable [142]. However, if the $LaAlO_3$ film is significantly off-stoichiometric, it can accept the extra oxygen, as schematically shown in Fig. 4.6(c). This atomic reconstruc-

tion resolves the polar problem without doping electrons to the $SrTiO_3$ substrate, resulting in an insulating interface.

These two schematic extremes of the possible reconstructions qualitatively explains why the film off-stoichiometry strongly reduces the sheet carrier density. In particular, the atomic reconstruction model can explain the similar effect of La and Al vacancies [Fig. 4.6(a)]: since both cation vacancies require oxygen vacancies to maintain bulk charge neutrality, essentially the same atomic reconstruction is available in both cases. However, it is difficult to quantitatively explain our observation within these extremal models. In particular, purely within the electronic reconstruction model, a linear relationship between the cation ratio and n_s is expected, which is not consistent with the data. On the other hand, purely within the atomic reconstruction model, no conductivity is expected when the film is off-stoichiometric. The experimentally realized situation is thus probably intermediate of these two extremes. Very recent related explorations which were carried out in rather different growth regimes (molecular beam epitaxy [145], sputtering [146], and higher pressure PLD [147]) observed somewhat different results from this study, suggesting that the interface conductivity, determined by the balance between atomic and electronic reconstructions, is sensitive also to other growth parameters, not purely only to $LaAlO_3$ stoichiometry.

4.5 Conclusion

In summary, we found a strong impact of the $LaAlO_3$ film stoichiometry, modulated by the laser parameters, on the electronic properties of the $LaAlO_3/SrTiO_3$ interface. In particular, film off-stoichiometry strongly reduced the carrier density at the interface. We propose that film off-stoichiometry changes the balance between atomic and electronic reconstructions, the former resolving the polar discontinuity without doping electrons.

This film stoichiometry dependence provides important insights into the microscopic carrier generation mechanisms at the $LaAlO_3/SrTiO_3$ interface, and assists optimization of the electronic properties for future applications. These results also gives better understanding of the growth dependence of the electronic phase diagrams of this system, which is vital for disentangling many of the conflicting studies by various groups.

The wide growth-tunability of the properties of the $LaAlO_3/SrTiO_3$ heterointerface is applied to the studies presented in the next two Chapters. In Chap. 5, a low-density high-mobility electron system is realized at the interface, enabling the observation of quantum oscillations which provides important information about the electronic structure of this system. In Chap. 6, the microscopic origin of ferromagnetism in the $LaAlO_3/SrTiO_3$ heterostructure and the mechanism of its coexistence with superconductivity are investigated in detail.

Chapter 5

Mobility Enhancement and Quantum Oscillations at the $LaAlO_3/SrTiO_3$ Heterointerface

5.1 Introduction

5.1.1 Mobility enhancement by reducing the growth temperature

As presented in the last Chapter, the electronic properties of the $LaAlO_3/SrTiO_3$ heterointerface can be controlled by growth conditions over a wide range, most notably by the film stoichiometry. Previous growth studies on this system indicate that there are many other important growth parameters (see Secs. 2.3.3 and 4.1.1). In particular, Caviglia *et al.* have reported that the growth temperature is also crucial to tune the electronic properties, especially the low temperature mobility [70]. As shown in Fig. 5.1, when the $LaAlO_3$ film is grown at relatively low temperatures ($\approx$ 600 °C), the Hall mobility at the interface is enhanced up to $\approx$ 4000 $cm^2V^{-1}s^{-1}$, several times higher than previously reported ($\approx$ 100–1000 $cm^2V^{-1}s^{-1}$) [40, 86, 87, 134].

The enhanced mobility provides a great opportunity to study the electronic structure at the interface in detail, using quantum oscillations at low temperatures under high magnetic fields. The requirements for observing quantum conductance oscillations are [148]

$$\omega_c \tau = B\mu > 1, \tag{5.1}$$

$$\hbar\omega_c > k_B T, \tag{5.2}$$

where $\omega_c = eB/m^*$ is the cyclotron frequency ($B = \mu_0 H$ is the applied magnetic flux density and m^* is the carrier effective mass), τ is the transport elastic scattering time, μ is the carrier mobility, $\hbar$ is the reduced Planck constant, k_B is the Boltzmann constant, and T is the measurement temperature. To fulfill Eq. 5.1 at $T \sim 1$ K and $B \lesssim 10$ T, which are the typical values reasonably achievable in a helium cryostat with a superconducting magnet, $\mu \gtrsim 1000$ $cm^2V^{-1}s^{-1}$ is required. Assuming $m^* \approx 1.2m_0$ [149] (m_0 is the bare electron mass) and $T \sim 1$ K, Eq. 5.2 is

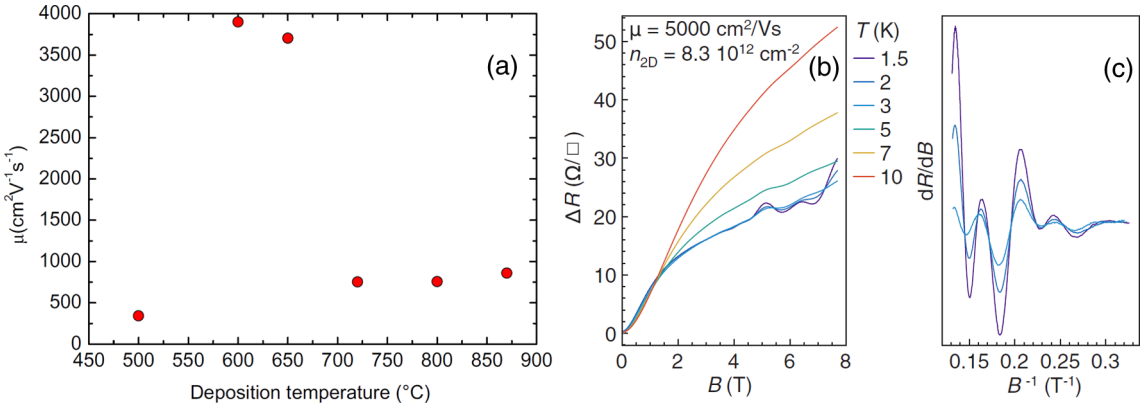

Fig. 5.1 (a) Growth temperature dependence of the Hall mobility of 10 uc $LaAlO_3/SrTiO_3$ samples, evaluated by Hall effect at 1.5 K. (b) Magnetoresistance of the high-mobility sample at different temperatures. (c) Numerical derivative of the data in (b) as a function of the inverse of the magnetic field. From Ref. [70], © 2010 American Physical Society.

fulfilled at $B \gtrsim 1$ T. As the enhanced mobility obtained by Caviglia *et al.* satisfies these conditions, they have observed clear Shubnikov–de Haas (SdH) oscillations, as shown in Figs. 5.1(b) and (c).

5.1.2 Discrepancy in carrier densities

The SdH oscillations are directly related to the Fermi surface, and thus contain important information about the electronic structure of the system [150]. For example, the Onsager relation enables an evaluation of the carrier density contributing to the SdH oscillations as

$$n_{\mathrm{SdH}} = f\frac{e}{h} \times N_{\mathrm{deg}}, \tag{5.3}$$

where f is the frequency, h is the Planck constant, and N_{deg} denotes the number of the degenerate states. The mobile carrier density can also be evaluated by the Hall effect as

$$n_{\mathrm{Hall}} = -\frac{1}{eR_{\mathrm{H}}}, \tag{5.4}$$

where R_{H} is the Hall coefficient (see also App. A). Ideally, the carrier densities evaluated by these two methods should be equal.

However, Caviglia *et al.* [70] found a discrepancy between n_{Hall} and n_{SdH}. As shown in Fig. 5.2(a), they found that the typical frequency of the SdH oscillations is 35 T (and a shoulder at $\approx$ 50 T). Assuming only the spin degeneracy ($N_{\mathrm{deg}} = 2$), the corresponding carrier density is evaluated to be $n_{\mathrm{SdH}} = 1.69 \times 10^{12}$ cm^{-2} ($\approx 2.4 \times 10^{12}$ cm^{-2} for the additional feature at $\approx$ 50 T), about an order of magnitude smaller than $n_{\mathrm{Hall}} = 1.05 \times 10^{13}$ cm^{-2}. The origin of this discrepancy is currently unclear. The existence of a non-oscillatory parallel transport channel, multiple degenerate valleys, or insufficient resolution within a magnetic field of $\approx$ 10 T are all possible mechanisms which are not well determined experimentally.

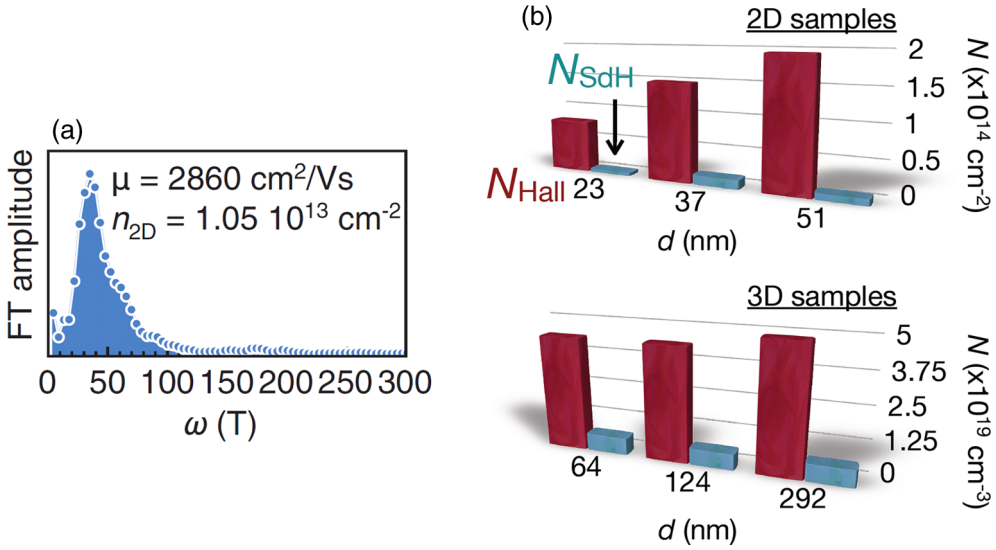

Fig. 5.2 (a) Fourier spectrum of the SdH oscillations of a typical high-mobility $LaAlO_3/SrTiO_3$ sample. From Ref. [70], © 2010 American Physical Society. (b) Carrier densities of δ-doped $SrTiO_3$ samples with different doped layer thicknesses, estimated from Hall effect (N_{Hall}) and SdH oscillations (N_{SdH}). From Ref. [155], © 2012 M. Kim.

It should be noted that the same order of discrepancy between n_{Hall} and n_{SdH} has been observed for the δ-doped $SrTiO_3$ heterostructure, where the thin Nb-doped layer is embedded between the nondoped buffer and cap layers. Owing to defect chemistry management in the $SrTiO_3$ films [151] as well as the strong quantum confinement which broadens the electron wave functions in the nondoped region [152], the δ-doped $SrTiO_3$ heterostructure also shows a very high mobility and SdH oscillations at low temperatures [153–155]. However, the confining potential profile in the δ-doped structure is designed to be symmetric, contrasting to the $LaAlO_3/SrTiO_3$ interface, which is asymmetric. Also, the carrier density of the δ-doped $SrTiO_3$ is relatively high, and the doped layer can be made arbitrarily thick [152, 154, 155]. Note that the thickness of the conducting layer at the $LaAlO_3/SrTiO_3$ interface is reported to be $\lesssim 10$ nm, estimated by conductive-tip atomic force microscopy [156], anisotropy of the superconducting transport properties [157], Seebeck effect [158], and infrared ellipsometry [159].[*1]

Despite these differences, the δ-doped $SrTiO_3$ heterostructure also shows much smaller n_{SdH} compared to n_{Hall} [153–155], as shown in Fig. 5.2(b), qualitatively the same as the $LaAlO_3/SrTiO_3$ heterointerface. This indicates that the origin of the discrepancy could be intrinsic to $SrTiO_3$ [154].

In this Chapter, in order to approach this discrepancy, we compare the SdH oscillations of different $LaAlO_3/SrTiO_3$ samples with various n_{Hall} and Hall mobilities (μ_{Hall}). As explained in Sec. 5.3, by tuning the growth temperature, the $LaAlO_3$ thickness, and the laser parameters, both μ_{Hall} and n_{Hall} were modulated over a wide range. The high mobility achieved enabled the

[*1] These estimations were made with relatively high-density low-mobility samples. The possible variation of the thickness with n_{Hall} and μ_{Hall} is currently not well known.

observation of clear SdH oscillations at low temperature. Most notably, as n_{Hall} decreased, the discrepancy between n_{Hall} and n_{SdH} became smaller, as presented in Sec. 5.4. A more detailed analysis using a pulsed magnet is described in Sec. 5.5, which suggests that the spin degeneracy can be resolved only under very high magnetic fields.

As discussed in Secs. 5.4.3 and 5.5.3, these results provide important insights into the complex electronic structure at the $LaAlO_3/SrTiO_3$ heterointerface. In particular, our observation suggests that at the lowest density regime ($n_{\mathrm{Hall}} \sim 3 \times 10^{12}$ cm^{-2}), nearly all of the mobile electrons contribute to the SdH oscillations.

5.2 Experimental details

The $LaAlO_3/SrTiO_3$ samples were fabricated by PLD (Sec. 3.2). Each $LaAlO_3$ film was grown on a 5×5 mm^2 $SrTiO_3$ (001) substrate with a TiO_2-terminated surface. Before growth, the substrates were preannealed at $T_{\mathrm{sub}} = 950$ °C in $P_{O_2} = 5 \times 10^{-6}$ Torr for 30 mins. As described in Sec. 5.3, the variable growth parameters were: the growth temperature (T_{g}), the $LaAlO_3$ thickness, and the laser parameters (fluence f, spot size A and the shape). After growth, the samples were cooled to room temperature in $P_{O_2} = 300$ Torr, with a one hour pause at $T_{\mathrm{sub}} = 500$–600 °C. It was confirmed that within this temperature range, details of the postannealing conditions do not have a significant effect on the electronic properties. Still, in order to minimize the possible effect of cation rearrangement (intermixing, defect formation) at high temperatures [160, 161], most samples were postannealed at relatively low tempearture ($T_{\mathrm{sub}} \approx 530$ °C).[*2] Unless otherwise indicated, the transport measurements were carried out in a PPMS (Sec. 3.5).

5.3 Enhancing the mobility by growth optimization

5.3.1 Reproducing the growth temperature dependence

We first examined the reproducibility of the growth temperature dependence reported by Caviglia *et al.* [70]. Figure 5.3 summarized the growth temperature dependence of the electronic properties of 10 uc $LaAlO_3/SrTiO_3$ samples. For these samples, the laser parameters were: $f = 0.7$ J/cm^2 and $A = 5.6$ mm^2, imaged to a rectangular spot using the zoom stage (see Sec. 3.2.1).

The temperature dependence of the sheet resistance of the all samples show metallic behavior down to 2 K [Fig. 5.3(a)]. As T_{g} decreases, n_{Hall} also decreases [Fig. 5.3(b)] and μ_{Hall} at low temperature increases [Fig. 5.3(c)]. The high mobilities of the $T_{\mathrm{g}} = 600$ °C and 700 °C samples enable the observation of SdH oscillations. As shown in Fig. 5.3(d), oscillatory components are observed for $\mu_0 H > 3$ T in the magnetoresistance of the $T_{\mathrm{g}} = 600$ °C sample, superimposed

[*2] Even reducing the postannealing temperature may cause another problem: the mobility of oxygen may not be sufficient at lower temperatures [162, 163], thus oxygen vacancies may remain in the substrate even after low temperature postannealing.

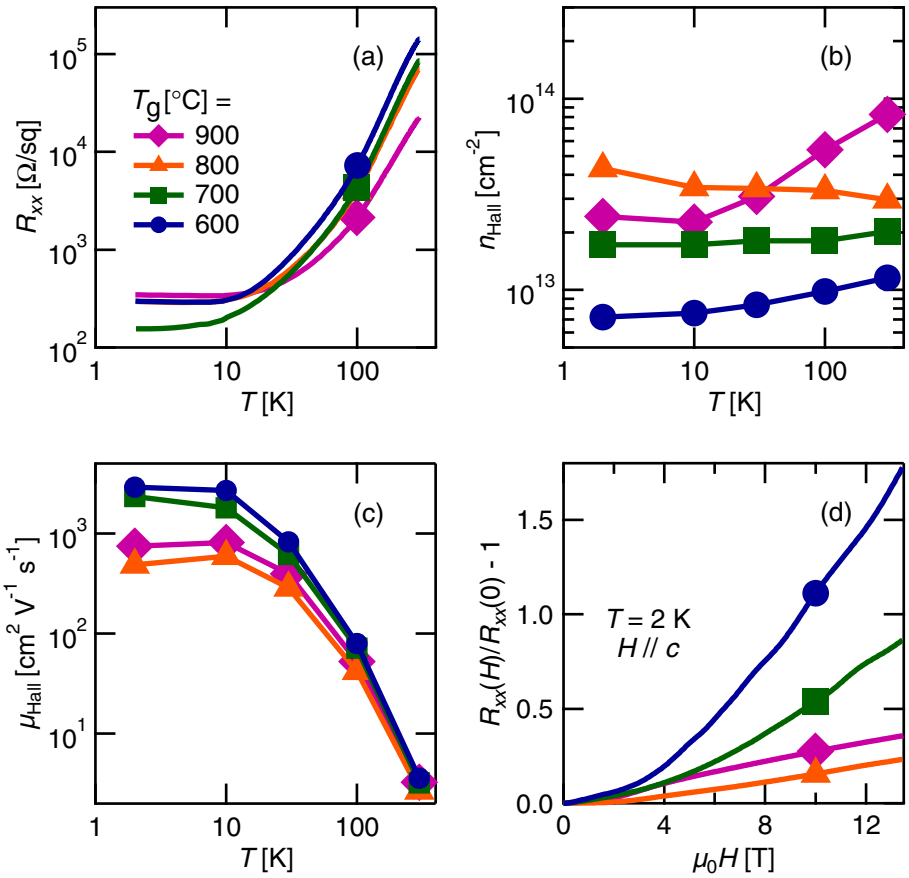

Fig. 5.3 Temperature dependence of (a) the sheet resistance, (b) the sheet carrier density, and (c) the Hall mobility of $LaAlO_3/SrTiO_3$ samples grown at various T_g. (d) Symmetrized magnetoresistance, measured at 2 K with magnetic field applied parallel to the substrate normal. Lines in (b) and (c) are guides to the eye.

on a positive background. Although less visible, the sample grown at T_g = 700 °C also shows oscillations of the magnetoresistance at high magnetic field. All of these results are qualitatively consistent with the previous report [70]. Quantitative comparison, in particular more detailed analysis of the SdH oscillations, is presented in Sec. 5.4.

5.3.2 Further optimization of the growth conditions

$LaAlO_3$ stoichiometry

As presented in Chap. 4, the $LaAlO_3$ film stoichiometry, modulated by the laser parameters, has a strong impact on the electronic properties. Thus the effect of the stoichiometry on the low temperature mobility was next examined. Figure 5.4(a) shows stoichiometry dependence of μ_{Hall} at 2 K of 10 uc $LaAlO_3/SrTiO_3$ samples grown at T_g = 600 °C. Details of the film stoichiometry modulation is presented in Sec. 4.3.1.

The highest mobility was obtained when the film is nearly stoichiometric. This is consistent with the results presented in Chap. 4. Although the growth conditions used in Chap. 4 were

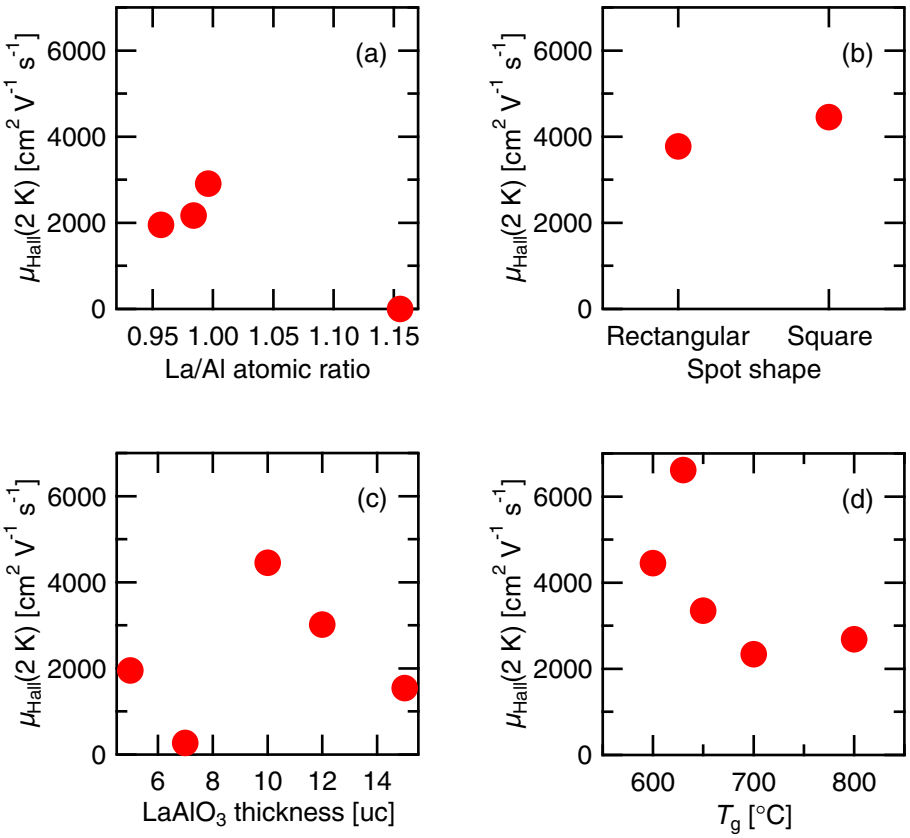

Fig. 5.4 Summary of the growth optimization. μ_{Hall} at 2 K as a function of (a) $LaAlO_3$ stoichiometry, (b) laser spot shape, (c) $LaAlO_3$ thickness, and (d) growth temperature.

quite different ($LaAlO_3$ thickness = 25 uc and T_g = 800 °C), the sheet resistance at the interface became larger with increasing the film off-stoichiometry, in particular at low temperatures (see Sec. 4.3.3, Fig. 4.4 in particular).

Film uniformity

The sharp peak of μ_{Hall} at the stoichometric point [Fig. 5.4(a)] indicates that even a small in-plane inhomogeneity of the $LaAlO_3$ film may be an issue. We thus next tried to minimize the in-plane inhomogeneity by optimizing the laser spot. First, the laser spot was imaged without the zoom stage to further improve the sharpness and the reproducibility of the laser profile (see Sec. 3.2.1 for details). Second, the shape of the aperture was changed to image a square, instead of rectangular, spot on the target, to minimize the anisotropic distribution of the ablated species.[*3]

Figure 5.4(a) shows μ_{Hall} at 2 K of 10 uc $LaAlO_3/SrTiO_3$ samples grown at T_g = 600 °C, using different laser conditions. The rectangular spot was 2.3 mm × 1.3 mm and the square spot was 1.8 mm × 1.8 mm, and the laser energy was kept constant at 20 mJ. The film off-stoichiometry was confirmed to be very small in both cases, by measuring the out-of-plane lat-

[*3] The rectangular aperture was useful to minimize the energy loss, and thus to obtain a relatively high fluence.

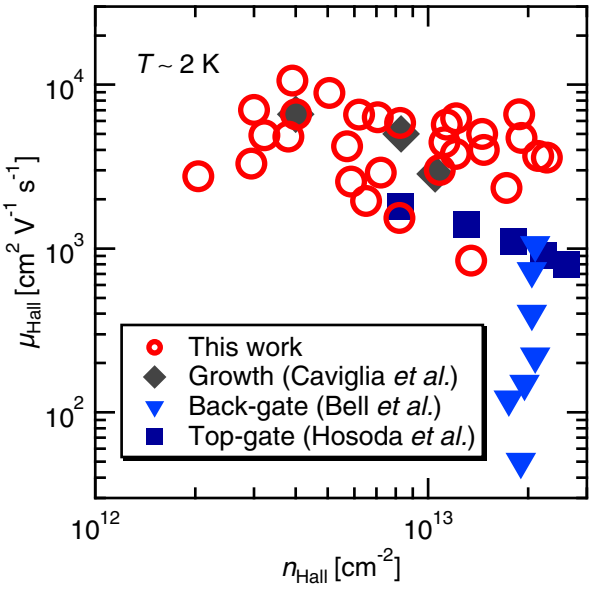

Fig. 5.5 Summary of μ_{Hall} as a function of n_{Hall} at low temperature (2 K for this work) for samples grown at various conditions. Results of another growth study (by Caviglia *et al.* [70]), back-gating (by Bell *et al.* [42]), and top-gating (by Hosoda *et al.* [68]) are also included for comparison.

tice constant of 25 uc $LaAlO_3$ films grown in these conditions (3.72 Å for both; see Sec. 4.3.1). Although the difference was small, higher μ_{Hall} was realized when growing using the square spot, likely due to the improved uniformity of the film.

Detailed $LaAlO_3$ thickness and temperature dependence

The $LaAlO_3$ thickness is known to be another important growth parameter [40, 87, 134], and thus its effect on the mobility was also examined. Figure 5.4(c) shows μ_{Hall} at 2 K of $LaAlO_3/SrTiO_3$ samples grown at T_g = 600 °C with different film thicknesses. The highest mobility was obtained for the 10 uc sample.

Finally the growth temperature was optimized in more detail. Figure 5.4(d) shows μ_{Hall} at 2 K of 10 uc $LaAlO_3/SrTiO_3$ samples grown at different T_g. The highest mobility was obtained for the T_g = 630 °C sample.

5.3.3 Controllable range and reproducibility

Figure 5.5 summarizes the growth-controllable range of μ_{Hall} and n_{Hall}, which also includes the data of the samples grown to examine the reproducibility. Both μ_{Hall} and n_{Hall} were modulated over a wide range, wider than that of conventional gating methods [42, 68]. In particular, the highest mobility achieved is 1.06×10^4 $\mathrm{cm^2V^{-1}s^{-1}}$. It is also notable that a general trend can be seen that μ_{Hall} increases with the decrease of n_{Hall}, qualitatively similar to that for bulk $SrTiO_3$ (see Sec. 2.2.1, Fig. 2.1(d) in particular).

However, scatter from the general trend is considerably large. This is mainly because the

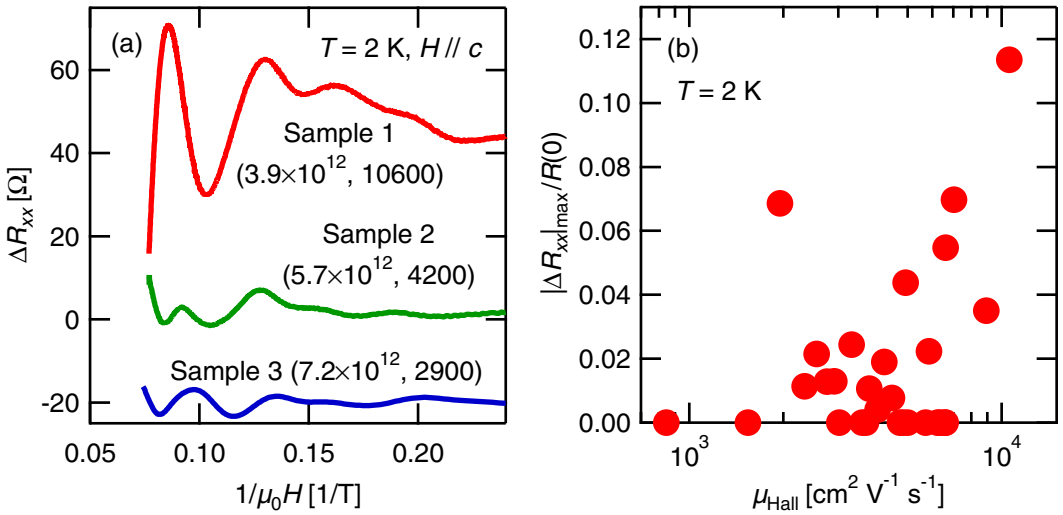

Fig. 5.6 (a) Magnetoresistance of three representative samples, after background subtraction, versus reciprocal magnetic field. Measured at 2 K with magnetic field applied parallel to the substrate normal. Numbers in parentheses indicate n_{Hall} [in cm^{-2}], μ_{Hall} [in $\mathrm{cm}^2\mathrm{V}^{-1}\mathrm{s}^{-1}$] for each sample. (b) Normalized SdH amplitude as a function of μ_{Hall} at 2 K.

reproducibility of the growth control is marginal; even when grown in nominally identical conditions, n_{Hall} and μ_{Hall} showed a sample-to-sample variation within a factor of ~ 2. Thus the growth optimization presented here should be considered just as a rough guideline. As μ_{Hall} seems to be highly sensitive to all of the growth parameters [Fig. 5.4], an extremely precise adjustment may be required to fully optimize and reproducibly grow the low-density high-mobility samples. It should also be noted that the samples have been exposed to air before the transport measurements, and the surface state, in particular water adsorption, is likely to have an inevitable sample-to-sample variation.[*4] It has been reported that polar adsorbates on the film surface decrease μ_{Hall} and increase n_{Hall} [98].

5.4 Analysis of the Shubnikov–de Haas oscillations

5.4.1 Typical oscillation data

The enhancement of the mobility has enabled the observation of SdH oscillations at low temperature, which are next analyzed. Typical SdH data at 2 K are shown in Fig. 5.6(a), which are extracted by fitting the positive magnetoresistance background (see Fig. 5.3(d)) using a polynomial function. Clear SdH oscillations were observed for many of the high-mobility samples, and in general the oscillations became more pronounced with increase of μ_{Hall}.

However, this trend was found *not* to be strong. Figure 5.6(b) shows the amplitude of the SdH oscillations normalized by the zero-field resistance as a function of μ_{Hall}. While there is a rough trend that the amplitude gets bigger with the increase of μ_{Hall}, scatter is nontrivial.

[*4] There was typically a few days interval between the growth and the transport characterization of each sample.

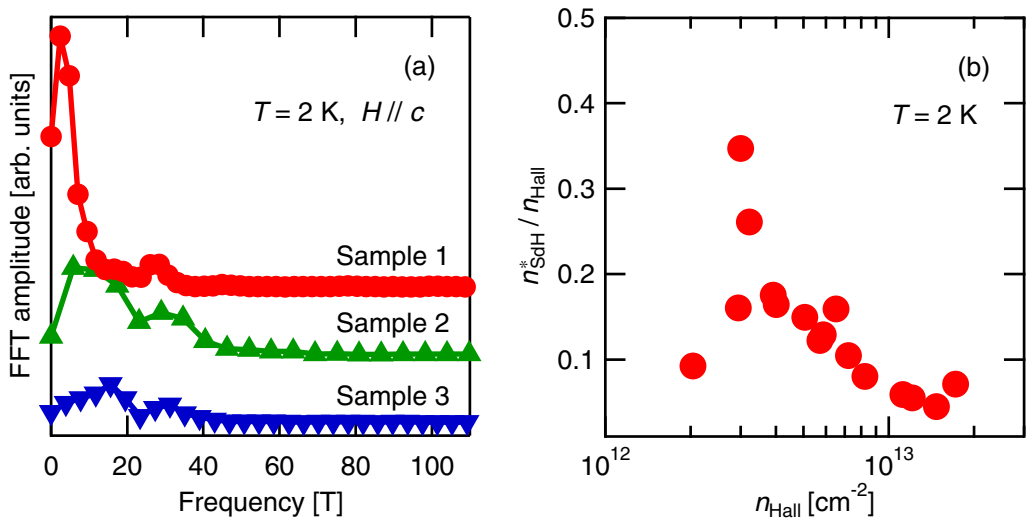

Fig. 5.7 (a) Fast Fourier transform (FFT) of the data in Fig. 5.6(a). (b) Ratio of the carrier densities n^*_{SdH}/n_{Hall} as a function of n_{Hall} at 2 K.

In particular, there were a few samples which showed no significant oscillation above noise (plotted as amplitude = 0), although the mobility was in principle sufficiently high. This is possibly due to the existence of multiple frequency components in the oscillations, smearing each other out, and for simplicity we neglect these samples below.

5.4.2 Comparison of carrier densities

Figure 5.7(a) shows the fast Fourier transform of the data in Fig. 5.6(a), from which the frequency of the SdH oscillations is extracted. Using the frequency, the carrier density contributing to the SdH oscillations was evaluated, assuming no valley or spin degeneracy, i.e., $n^*_{SdH} = fe/h$ (the superscript $*$ emphasizes the assumption of no degeneracy; see also Eq. 5.3). As shown in the figure, multiple frequency components were often observed. n^*_{SdH} was evaluated using the highest frequency, which can be assigned to the total density of oscillating electrons [164, 165].

Figure 5.7(b) shows the ratio of the carrier densities evaluated by SdH and Hall, i.e., n^*_{SdH}/n_{Hall}, as a function of n_{Hall}. Down to $n_{Hall} \sim 3 \times 10^{12}$ cm^2, the n^*_{SdH}/n_{Hall} ratio monotonically increases with decreasing n_{Hall}. This can be understood that when the carrier density is relatively high, multiple subbands are occupied, and only a part of them contributes to the SdH oscillations. At the lowest density regime, the ratio approaches $\sim$ 0.4–0.5 ($\sim 1/2$), although it is rather arbitrary to deduce any number purely within this data set. Possible interpretations of this number is discussed in more detail below.

5.4.3 Discussion

We next discuss the possible explanation of the results presented. Bulk $SrTiO_3$ is a d^0 electron system with a threefold degenerate conduction band at the Γ point, formed by the anisotropic

d_{xy}, d_{yz}, and d_{zx} t_{2g} orbitals. The added effects of a tetragonal distortion at $\sim$ 105 K and the spin-orbit interaction mix these orbital characteristics, and split into a heavy electron band, a light electron band, and a spin-orbit split-off band [27, 28]. Quantum confinement at the $LaAlO_3/SrTiO_3$ interface produces a series of two-dimensional subbands derived from those bands, with different orbital characters and effective masses [93, 166]. In particular, subbands with yz/zx characters are expected to have heavy effective masses in plane, due to the smaller hopping integrals.

When the electron density is relatively high ($\gtrsim 10^{13}$ cm^{-2}), multiple subbands are likely occupied, including the heavy subbands [166]. These heavy effective mass makes it more challenging to fulfill the condition to detect them via SdH oscillations, i.e., Eq. 5.1. Therefore, the heavy subbands can be the origin of the discrepancy between n^*_{SdH} and n_{Hall} at the relatively high n_{Hall} regime. The heavy electrons are theoretically expected to remain even in very low density regimes ($\lesssim 5 \times 10^{12}$ cm^{-2}) [166], and thus the $n^*_{\mathrm{SdH}}/n_{\mathrm{Hall}} \sim 1/2$ may also be explained by the existence of the non-oscillatory parallel transport channel.

Another possible interpretation of the number is that there is a two-fold degeneracy[*5] and nearly all of the electrons contribute to the oscillations (the heavy electrons are localized and do not contribute even to the Hall effect [93]). A strong candidate of the origin of this possible two-fold degeneracy is the spin degeneracy. However, due to the limited features observed within a magnetic field of 13 T (and at a temperature of 2 K), a stronger conclusion is difficult to make. Therefore, in the next Section, the SdH oscillations were measured under higher magnetic fields, in order to obtain more information from them.[*6]

5.5 Measurement under high magnet field

5.5.1 Brief review of the pulsed magnet

It is well known to be very difficult to create high magnetic fields. This is mainly because of the large current needed ($>$ 100 A), and the Joule heat resulting from it. Therefore, in order to induce a *static* high magnetic field in a electromagnet, a huge power supply and cooling capacity are required. This problem can partly be resolved by making the electromagnet with a superconductor. However, there still remains another limiting factor that superconductivity is quenched above certain critical current/field.

The Joule heat problem can be avoided if the current passes through the circuit for only a short time, which is the main reason why a *pulsed* magnet can create larger magnetic fields than DC magnets. A large pulsed current can be induced by a circuit schematically shown in Fig. 5.8(a). When the inductance L of the electromagnet coil, the capacitance C (charged by

[*5] Purely within the data set in Fig. 5.7(b), $n^*_{\mathrm{SdH}}/n_{\mathrm{Hall}} \sim 1/3$ is perhaps a more reasonable number. However, a three-fold degeneracy is not reasonable considering the symmetry at the interface.

[*6] As the Dingle temperature, which is a measure of the level of disorder, is reported to be 6 K [70], decreasing the temperature is perhaps insufficient (although likely helpful to some extent) to improve the resolution.

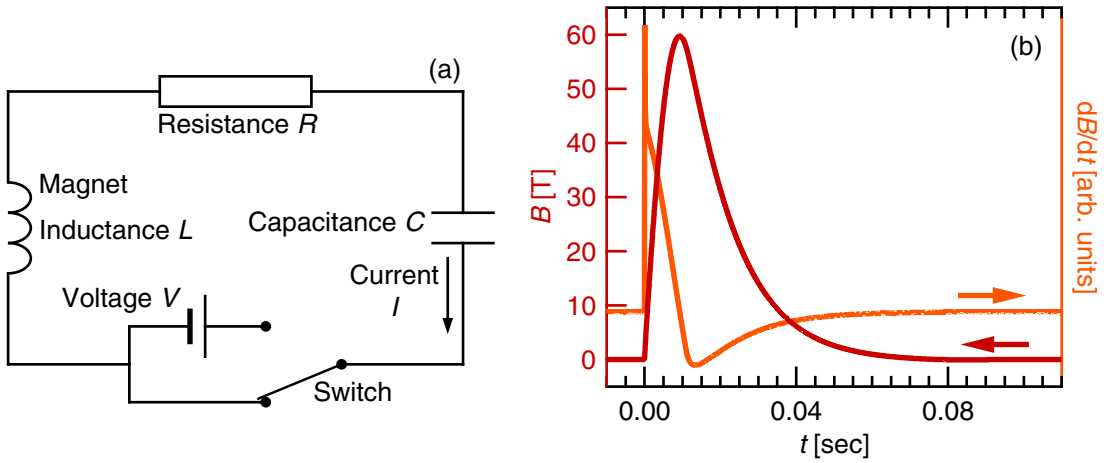

Fig. 5.8 (a) Simplified diagram of the circuit to create the pulsed magnetic field. (b) Magnetic flux density in the coil and its numerical derivative as a function of time.

voltage V), and the resistance R satisfies

$$R = 2\sqrt{\frac{L}{C}}, \tag{5.5}$$

after switching on the circuit, a pulsed current flows:

$$I(t) = \frac{V}{L} t \exp\left(-\frac{R}{2L}t\right), \tag{5.6}$$

where t denotes the time and $t = 0$ corresponds to the time when the switch is on. The magnetic field in the coil is proportional to this pulsed current. Eqs. 5.5 and 5.6 indicate that in order to obtain large I ($\propto$ magnetic field) for a reasonably long time, large V and C are needed. These are also challenging, but more practical compared to the Joule heat problem.

In this study, a 65 T short pulse magnet in the National High Magnetic Field Laboratory, Pulsed Field Facility was used [167]. The profile of the pulsed magnetic field is shown in Fig. 5.8(b). To briefly summarize the important characteristics, the magnetic field is raised in $\approx$ 9.6 msec up to 60 T,[*7] and decays in $\approx$ 70 msec. The full width at half maximum of the pulse is $\approx$ 18 msec. Experiments with the pulsed magnet were strongly supported by Dr. Jaewook Kim, Dr. Marcelo Jaime, and Dr. Ross D. McDonald (National High Magnetic Field Laboratory, Los Alamos National Laboratory, USA).

5.5.2 Shubnikov–de Haas oscillations up to 60 T

A high-mobility $LaAlO_3/SrTiO_3$ sample ($n_{\mathrm{Hall}} \approx 1.3\times10^{13}$ cm^{-2}, $\mu_{\mathrm{Hall}} \approx 3500$ cm^{2}V^{-1}s^{-1}) was characterized using the pulsed magnet.[*8] A 10 μA DC bias was applied to the sample in order to

[*7] During our experiment, the maximum magnetic field was limited to 60 T due to a minor problem with the bank capacitance.

[*8] This specific sample was fabricated by Dr. Yanwu Xie.

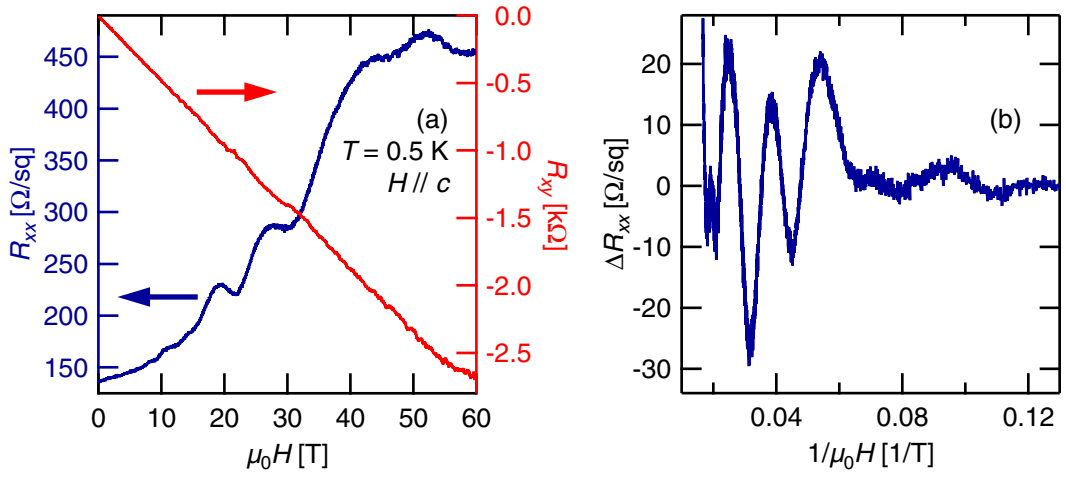

Fig. 5.9 (a) Symmetrized magnetoresistance and antisymmetrized Hall resistance, measured at 0.5 K with magnetic field applied parallel to the substrate normal. (b) Magnetoresistance, after background subtraction, versus reciprocal magnetic field.

measure the high resistivity (see App. A for details). Figure 5.9(a) shows the magnetoresistance and the Hall resistance of the sample at 0.5 K. Clear SdH oscillations were observed, and the Hall resistance also showed small, but significant oscillation-like features, indicating that the system was approaching the full quantum regime.

Additionally, there was a splitting of the SdH oscillation peaks at $\sim$ 50 T, reminiscent of the Zeeman effect. This can more clearly be seen after background subtraction, as shown in Fig. 5.9(b). This suggests that the spin degeneracy can be resolved only under very high magnetic fields, and thus the possible $\sim$2-fold degeneracy discussed in Sec. 5.4.3 could originate from the effective spin degeneracy under the relatively low fields.

5.5.3 Discussion

Next we discuss the possibility of the the effective spin degeneracy in more detail. As schematically shown in Fig. 5.10(a), the density of states of a two-dimensional system is quantized under magnetic field by the Landau quantization, and each quantized level is split by the Zeeman effect. The energy level of the quantized states is expressed as

$$\begin{aligned} E_{N,\pm} &= \hbar\omega_c \left(N + \frac{1}{2}\right) \pm \frac{1}{2} g^* \mu_B B \\ &= \frac{\hbar e B}{m^*} \left(N + \frac{1}{2}\right) \pm \frac{g^*}{2} \frac{\hbar e B}{2m_0}, \end{aligned} \tag{5.7}$$

where N is the Landau index, $\pm$ denotes the spin direction, g^* is the Landé g-factor, and $\mu_B = e\hbar/2m_0$ is the Bohr magneton. The first term denotes the Landau quantization, the latter the Zeeman effect.

When the Zeeman spin splitting $g^*\mu_B B$ is smaller compared to disorder broadening, it cannot experimentally be resolved, causing a spin degeneracy. However, considering the bulk value of

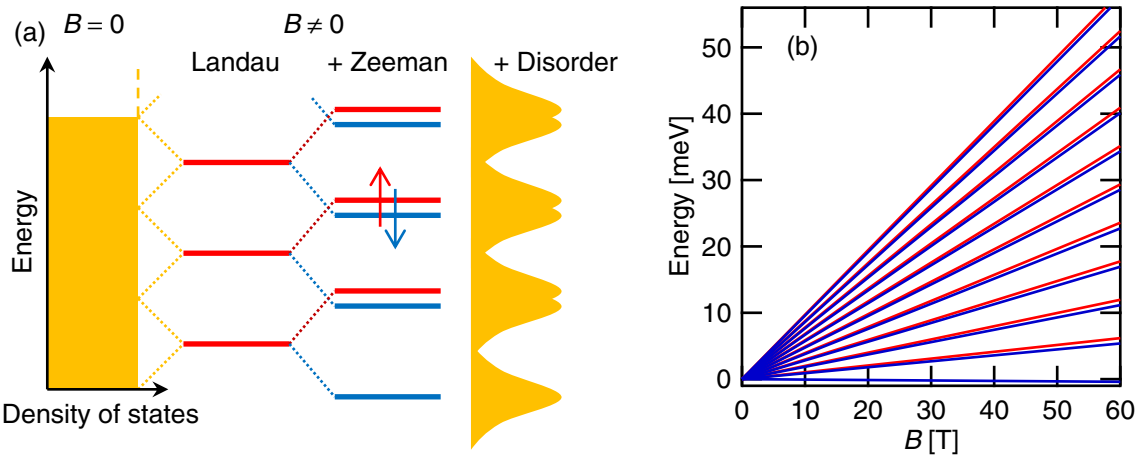

Fig. 5.10 (a) Schematic illustration of Landau quantization, Zeeman effect, and disorder broadening of the density of states of a two-dimensional system under magnetic field. (b) Simulated Landau level spectrum as a function of B, assuming $m^* = 1.2m_0$ and $g^* = 1.9$. The red lines are the up-spin branch and the blue lines are the down-spin branch. For each branch, the Landau index increases from bottom to top.

$g^* \approx 1.9$ [168], this situation is not likely. Indeed, $m^* \approx 1.2m_0$ in bulk [149] indicates that the separation of the Landau levels $\hbar\omega_c$ is comparable to the Zeeman splitting. Therefore, when clear SdH oscillations are observed, which indicates the Landau levels are well resolved, the intrinsic spin degeneracy should also be lifted.

The *effective* spin degeneracy is thus more likely caused by

$$\begin{aligned} E_{(N+1),-} &= \frac{\hbar eB}{m^*}\left(N+\frac{3}{2}\right) - \frac{g^*}{2}\frac{\hbar eB}{2m_0} \\ &\approx \frac{\hbar eB}{m^*}\left(N+\frac{1}{2}\right) + \frac{g^*}{2}\frac{\hbar eB}{2m_0} = E_{N,+}, \end{aligned} \tag{5.8}$$

which is satisfied when $g^* \approx 2\,(m^*/m_0)$. Indeed, $m^* \approx 1.2m_0$ and $g^* \approx 1.9$ in bulk $SrTiO_3$ [149, 168] nearly satisfy this condition, and therefore this effective spin degeneracy can only be resolved under very high magnetic fields, as shown in Fig. 5.10(b).

In order to confirm this picture, it is necessary to quantify m^* and g^* at the $LaAlO_3/SrTiO_3$ interface, which are suggested to be somewhat different from bulk [70, 169]. Therefore, further angle and temperature dependent measurements using the pulsed magnet are of particular importance, which are expected to give crucial information that will quantify the Zeeman effect and subband structure in more detail.

5.6 Conclusion

In summary, we fabricated $LaAlO_3/SrTiO_3$ heterostructures with various n_{Hall} and μ_{Hall}, controlled by growth conditions. The low-temperature mobility was greatly enhanced by growth optimization, which enabled the observation of quantum oscillations under high magnetic

fields. The discrepancy between n_{Hall} and n_{SdH} became smaller as n_{Hall} was reduced, and the pulsed magnet measurement suggested the presence of an effective spin degeneracy. These results suggest that around the peak density in Fig. 5.7(b), all of the mobile electrons were detected via the quantum oscillations.

These results provide an important basis for further investigation into the complex electronic structure of this system. In particular, measurements in the full quantum Hall regime using the pulsed magnet should be helpful, which is in principle possible with the low-density high-mobility sample fabricated in this study. Also, the low density superconductivity in $SrTiO_3$ [47, 48] suggests that the low-density high-mobility system achieved in this study may enable study of possible interplay between quantum Hall states and superconductivity, which is theoretically expected to show novel emergent phenomena [170].

Chapter 6

Ferromagnetism in the $LaAlO_3/SrTiO_3$ Heterostructure

6.1 Introduction

6.1.1 Indication of ferromagnetism in previous studies

The $LaAlO_3/SrTiO_3$ heterointerface has been attracting much interest, not only because of the unexpected conductivity, but also because of many other intriguing properties. Two-dimensional superconductivity [41, 69, 157] and ferromagnetism [71, 171–174] are important examples of such properties. The latter is perhaps the most unexpected phenomenon, since it rarely coexists with superconductivity in nature. It should also be noted that ferromagnetism in this system has no bulk analogue in the constituent materials; although bulk $SrTiO_3$ can be doped to be metallic and superconducting (see Sec. 2.2.1), there is no explicitly published work showing any magnetic ordering in $SrTiO_3$ or $LaAlO_3$ in bulk form. In these senses, ferromagnetism is a particularly exotic, but controversial property of this system.

The possibility of ferromagnetism was first suggested in 2007 by Brinkman *et al.* [71]. They have controlled the electronic properties of $LaAlO_3/SrTiO_3$ samples by varying the oxygen partial pressure during growth. As shown in Fig. 6.1(a), their observation shows a progressive change from metallic to almost insulating behavior at low temperatures with increasing the growth pressure. They have attributed the upturn in the resistance of the nearly insulating samples to the Kondo effect, which describes the interplay between localized magnetic moments and mobile carriers [175]. They have also found that the samples with high resistivity shows an isotropic negative magnetoresistance and hysteresis, as shown in Fig. 6.1(b), which may also be interpreted to originate from ferromagnetism.

However, the previous studies had several open issues. First, a precise interpretation of the magneto-transport to extract microscopic origins is difficult, partly because of the large magnetic field sweep rate of 30 mT/sec [71], and the exact nature of the magnetic ordering remains unknown. It should also be noted that superconductivity has been discovered also in 2007 by Reyren *et al.* [69], for samples showing more metallic behavior. Within these two

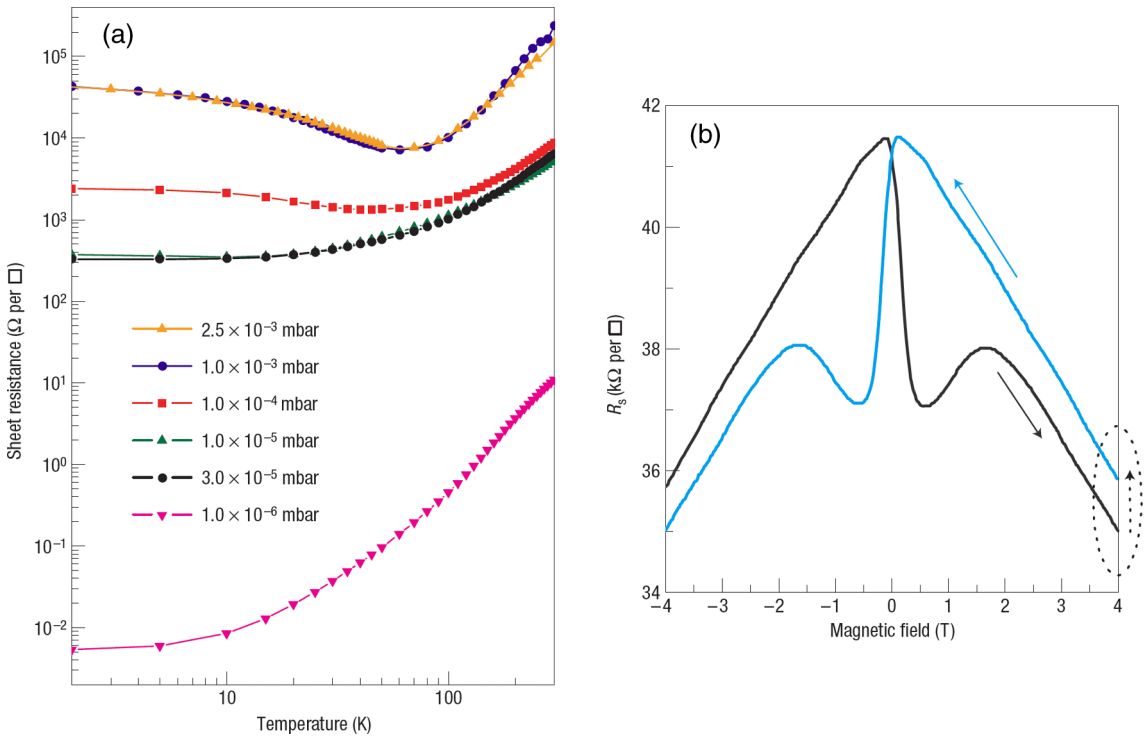

Fig. 6.1 (a) Temperature dependence of the sheet resistance of as-grown 26 uc $LaAlO_3/SrTiO_3$ samples grown in various oxygen pressures. (b) Magnetoresistance at 0.3 K of the sample grown at 1.0×10^{-3} mbar. Arrows indicate the direction of the measurements, and the area enclosed by the dashed line denotes an $\approx$ 30 sec wait at 4 T. Reprinted by permission from Macmillan Publishers Ltd: Nature Materials [71], © 2007.

reports in 2007, it would be more reasonable to interpret that depending on the growth details of a given sample, the interface becomes ferromagnetic *or* superconducting at low temperature: ferromagnetism and superconductivity do not coexist, but rather compete with each other. Possible contributions of impurities or defects are also not excluded; although no ferromagnetic behavior has experimentally been found in bulk $SrTiO_3$ or $LaAlO_3$, it still has been theoretically proposed that cation/anion defects play an important role for the formation of magnetism [176–178].

6.1.2 Direct imaging of the coexistence with superconductivity

Subsequent studies have further supported the existence of magnetic order in the $LaAlO_3/SrTiO_3$ heterostructure [171–174], partly resolving the ambiguity and the open questions remained in the previous studies. For example, Bert *et al.* have directly imaged the coexistence of ferromagnetism and superconductivity in this system, using a scanning Superconducting QUantum Interference Device (scanning SQUID) [174]. One of the most important features of the device is its ability to simultaneously measure magnetization and magnetic susceptibility [179, 180].

Using scanning SQUID, Bert *et al.* [174] have measured the local magnetic moments and

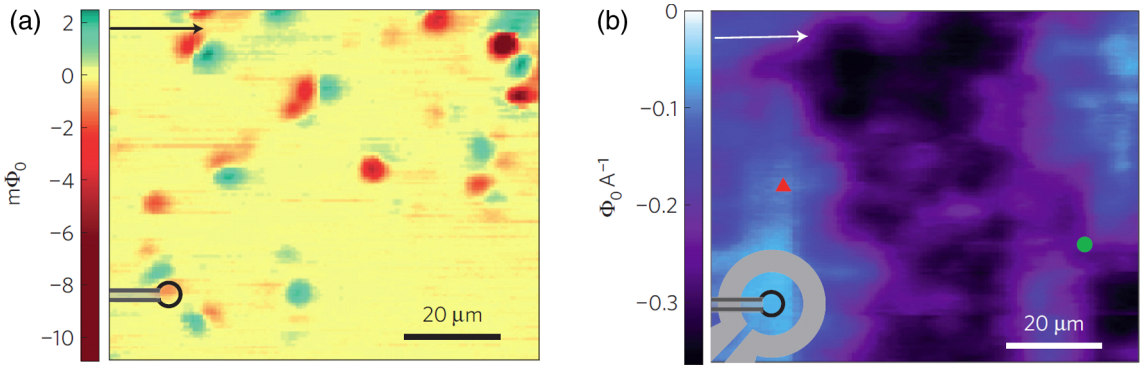

Fig. 6.2 (a) Scanning SQUID magnetometry image of a 10 uc $LaAlO_3/SrTiO_3$ sample. Inset: Scale image of the SQUID pick-up loop used to sense magnetic flux. (b) Susceptometry image. Inset: Scale image of the SQUID pick-up loop and field coil. Both are taken at 40 mK. Reprinted by permission from Macmillan Publishers Ltd: Nature Physics [174], © 2011.

the susceptibility of a $LaAlO_3/SrTiO_3$ sample at low temperature. As shown in Figs. 6.2(a) and (b), they have found many magnetic dipoles and a significant diamagnetic susceptibility in the sample, the latter originating from the perfect diamagnetism of the superfluid. Both of the magnetometry and susceptometry images show micrometer-scale spatial inhomogeneity. It is also important to note that the diamagnetic signal of the $LaAlO_3/SrTiO_3$ sample is an order of magnitude smaller than that of δ-doped $SrTiO_3$ [174], another two-dimensional superconducting system in $SrTiO_3$-based heterostructures [153, 154].

6.1.3 Open questions

While the recent experiments have confirmed the coexistence of ferromagnetism and superconductivity, there still remain several open questions. Perhaps the most important challenge is to understand the mechanism that makes the coexistence possible in this system. The large scale inhomogeneity of ferromagnetism and superconductivity, as well as the very weak signal of the latter [174], suggests that ferromagnetism and superconductivity compete with each other.[*1] It is also important to note that, while the recent reports qualitatively agree that the $LaAlO_3/SrTiO_3$ heterostructure shows both ferromagnetism and superconductivity, there is a quantitative disagreement in the moment density. In particular, polarized neutron reflectometry measurements have set an upper limit for the magnetization [181] that is much smaller than that observed in bulk measurements, such as magneto-transport, torque magnetometry, etc [171–173], but still higher than the value obtained by scanning SQUID [174].

Another critical question is the host of ferromagnetism. In principle, magnetism could arises from cation/anion defects in the $LaAlO_3$ or $SrTiO_3$, or could be specific to the interface, all of which have been theoretically proposed [176–178, 182–184]. However, no experiment thus far

[*1] It is also not clear that the competition is the cause of the inhomogeneity, since there is no clear spatial (anti-) correlation between the magnetometry and susceptometry images [174].

has provided direct information on the host of magnetism. Thus it is of central importance to determine the microscopic nature of the observed ferromagnetism.

In this Chapter, in order to address these issues, we characterize the magnetic properties of $LaAlO_3/SrTiO_3$ samples using scanning SQUID and synchrotron based spectroscopic techniques. Scanning SQUID is employed mainly to investigate the correlation between magnetic and (super)conducting properties, by tuning the latter with various methods, including growth control. As presented in Sec. 6.3, we found that magnetism appears only above a critical $LaAlO_3$ thickness, similar to conductivity. However, we also found that magnetism was not affected by controlling the (super)conductivity by interface termination or by electric field effect, as also explained in Sec. 6.3. These observations indicate that interface reconstruction driven by the polar discontinuity is necessary for the formation of magnetism, but the existence of mobile carriers is not a prerequisite.

Using the element-specific spectroscopic techniques, we found direct evidence for in-plane ferromagnetic order at the interface, with Ti^{3+} character in the d_{xy} orbital of the anisotropic t_{2g} band, as presented in Sec. 6.4. These results provide important insights into the microscopic origin of the ferromagnetism and the mechanism of its coexistence with superconductivity, as discussed in Secs. 6.3.4 and 6.4.3.

The work presented in this Chapter was done in strong collaboration with two groups: scanning SQUID measurements were performed by Prof. Kathryn A. Moler's group (Stanford University, USA), and the spectroscopic investigations were made by Dr. Jun-Sik Lee and Prof. Chi-Chang Kao (SLAC National Accelerator Laboratory, USA). This work is published in Refs. [185–187]. Related investigations are published in Refs. [188, 189].

6.2 Experimental details

6.2.1 Scanning superconducting quantum interference device

Magnetic properties of $LaAlO_3/SrTiO_3$ samples were characterized using a scanning SQUID, which is schematically shown in Fig. 6.3(a-1). Details of the device are described in Refs. [179, 180]. SQUIDs in general consist of a superconducting loop with two Josephson junctions. The current–voltage characteristic of the loop is strongly modulated by the magnetic flux inside the loop, enabling a high-sensitivity measurement of magnetic fields. In this study, Nb and AlO_x were used as the superconductor and the insulating barrier, respectively.

An important feature of the scanning SQUID is that it is microminiaturized, as shown in Fig. 6.3(a-2), in order to locally characterize the macroscopic samples that may be mesoscopically inhomogeneous. The diameter of the pickup loop is nominally 3 μm. Owing to the microminiaturization, as well as the counter loop which cancels the background signal and the modulation coils which allow the device to operate at the maximum-sensitivity bias point for all measurement conditions, the sensitivity of the device is highly improved. The sensitivity is better than $10^{-6}\phi_0 / \sqrt{\text{Hz}}$, where $\phi_0 = h/2e$ is the flux quantum.

The scanning SQUID also has a field coil surrounding the pickup loop, as shown in Figs. 6.3(a-1) and (a-2). Applying an AC current in the coil to produce a local magnetic field,

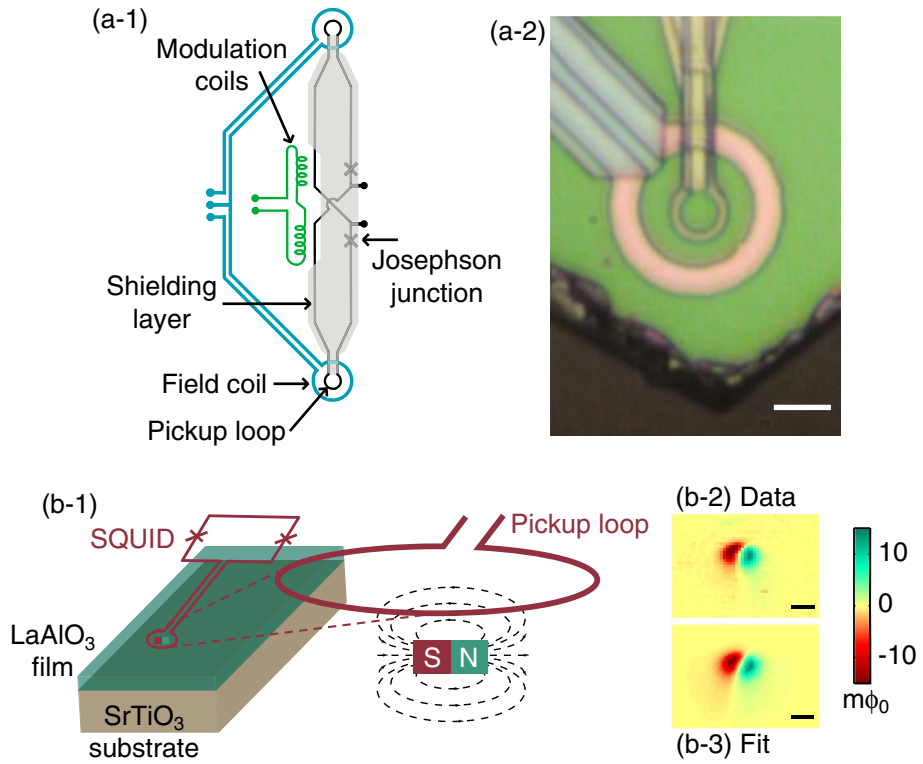

Fig. 6.3 (a-1) Simplified diagram of the scanning SQUID and (a-2) photomicrograph of the sensor area of the device. Scale bar: 5 µm. Reprinted with permission from Ref. [180]. © 2008, AIP Publishing LLC. (b-1) Schematic illustration of the measurement geometry and field lines from a in-plane ferromagnetic patch (conceptually shown here as a small bar magnet) captured in the pickup loop. (b-2) Typical image (data) of a ferromagnetic patch. Scale bar: 10 µm. (b-3) Fit of the data in (b-2) to a point dipole model, giving a dipole moment of $7 \times 10^7\,\mu_B$. Published in Ref. [185].

the magnetic susceptibility of the sample is detected by the pickup loop in a lock-in measurement. Since the magnetometry is a DC measurement, the lock-in technique can separate the magnetometry and susceptometry signals, enabling simultaneous measurement.

Figure 6.3(b-1) schematically shows the measurement geometry using the scanning SQUID. A magnetic dipole in the sample (conceptually shown as a small bar magnet) produces local magnetic fields (dashed lines), which is detected by the pickup loop of the SQUID. Typical data of a ferromagnetic patch is shown in Fig. 6.3(b-2). The faint tails to the bottom of the dipole are due to flux captured by the unshielded section of the leads to the pickup loop. By fitting the data to a point dipole model, we can obtain the dipole moment ($7 \times 10^7\,\mu_B$ in this case), as shown in Fig. 6.3(b-3).

6.2.2 Details of sample growth

The $LaAlO_3/SrTiO_3$ samples were fabricated by PLD (Sec. 3.2). Each $LaAlO_3$ film was grown on a 5×5 mm^2 $SrTiO_3$ (001) substrate with a TiO_2-terminated surface. Before growth, the sub-

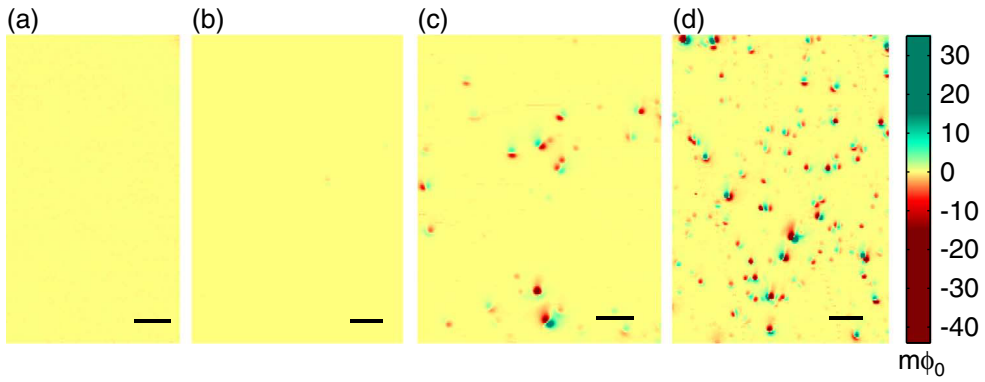

Fig. 6.4 Typical scanning SQUID images of $LaAlO_3/SrTiO_3$ samples taken at 4 K, showing no ferromagnetic patches for (a) annealed $SrTiO_3$ (no $LaAlO_3$ film) and (b) 2 uc of $LaAlO_3$, and ferromagnetic patches for (c) 5 uc and (d) 10 uc of $LaAlO_3$. Scale bar: 30 μm. Published in Ref. [185].

strates were preannealed at $T_{sub} = 950$ °C in $P_{O_2} = 5 \times 10^{-6}$ Torr for 30 mins. Following this anneal, T_{sub} was reduced to 800 °C and P_{O_2} was increased to 1×10^{-5} Torr, the film growth conditions. The laser beam was imaged to a rectangular spot of area 3.0 mm^2 on the $LaAlO_3$ target using the zoom stage (Sec. 3.2.1). The laser fluence was 0.7 J/cm^2. The $LaAlO_3$ film thickness (variable) was monitored using the *in situ* RHEED (Sec. 3.2.4). After growth, the samples were cooled to room temperature in $P_{O_2} = 300$ Torr, with a one hour pause at $T_{sub} = 600$ °C. The *n*-type interface grown in these conditions was confirmed to show electronic properties typically reported in the literature (Chap. 4; see also Ref. [134]).

6.3 Controlling ferromagnetism and superconductivity

6.3.1 $LaAlO_3$ thickness dependence

An important control parameter for the conductivity at the $LaAlO_3/SrTiO_3$ interface is the film thickness [40, 87, 134]. In particular, the existence of a critical thickness of 3–4 uc required for conductivity [40] can be interpreted to support the polar discontinuity picture (see Sec. 2.3.3). Therefore, we first examined the possible effect of the film thickness on ferromagnetism. A total of 9 $LaAlO_3/SrTiO_3$ samples were grown with varying the film thickness in the conditions mentioned above. Another 3 control samples were also prepared: as-received $SrTiO_3$ and $LaAlO_3$ substrates, and a $SrTiO_3$ substrate pre- and post-annealed in the same conditions for the $LaAlO_3/SrTiO_3$ samples (defined as the 0 uc sample).

Figures 6.4(a)–(d) show representative examples of the magnetic landscapes for four different thicknesses of the $LaAlO_3$ layer. The electrically insulating samples ($LaAlO_3$ thickness $<$ 3 uc, Figs. 6.4(a) and (b)) show very small ferromagnetic signal. On the other hand, the conducting samples ($LaAlO_3$ thickness $>$ 3 uc, Figs. 6.4(c) and (d)) show ferromagnetic patches that are spatially inhomogeneous on a micrometer scale. Most of the dipoles in the conducting samples lie in plane, with no clear preferential azimuthal orientation. The ferromagnetic

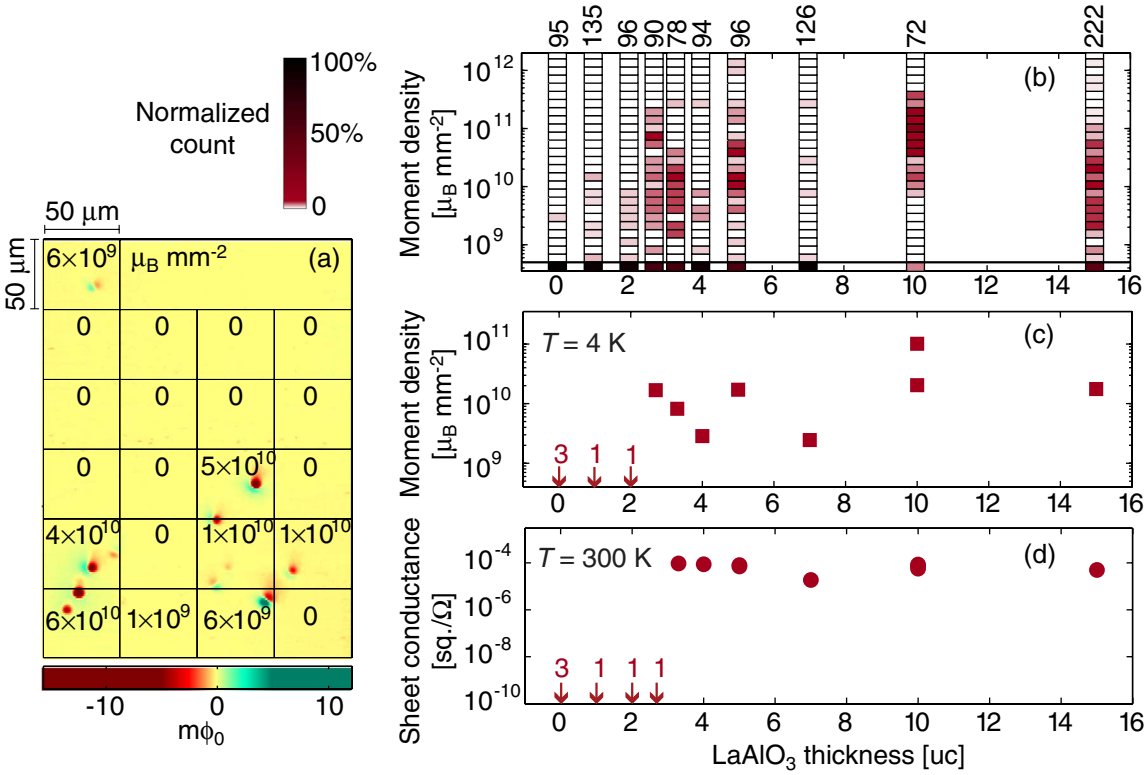

Fig. 6.5 (a) Large area scan at 4 K of the 5 uc sample divided into 50 μm × 50 μm squares, demonstrating the inhomogeneous distribution of the ferromagnetic patches. The numbers are the moment density in μ_B mm^{-2} in each square. (b) Histograms of the moment densities for ten samples with varying thickness. For each sample, color indicates the percentage of squares that have a particular moment density. The number at the top of each column represents the number of 50 μm squares measured in each sample. (c) Averaged moment density at 4 K and (d) sheet conductance at 300 K as a function of the $LaAlO_3$ thickness. Off scale values are marked by an arrow, which includes the number of samples measured for that thickness. Published in Ref. [185].

patches have a broad range of magnetic moments up to a few times $10^8\,\mu_B$ with a typical value around $10^7\,\mu_B$.

The $LaAlO_3/SrTiO_3$ samples above a critical thickness of about 3 uc showed ferromagnetic landscapes qualitatively similar to those shown in Figs. 6.4(c) and (d), with strong sample-to-sample variation. Two of the samples (4 and 7 uc) showed in particular dilute distributions of magnetic patches. On the other hand, the samples below the critical thickness, as well as the control samples, showed no detectable ferromagnetic patches.

The spatially heterogeneous distribution of ferromagnetism and sample-to-sample variation were quantitatively analyzed as follows. The large area scan of each sample was divided into 50 μm × 50 μm squares, and the moment density in each square was calculated, as shown in Fig. 6.5(a). Using ∼ 100 squares, a histogram of the moment densities were made for each sample, as shown in Fig. 6.5(b). As seen in the figures, many of the regions have no detected magnetic moment larger than $2 \times 10^5\,\mu_B$ (sensitivity threshold), and the local moment densities

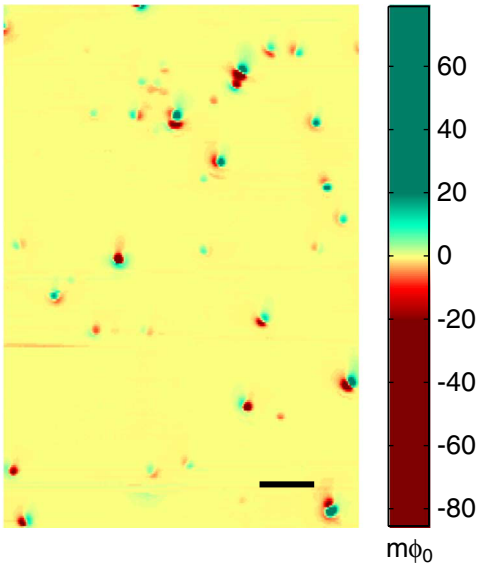

Fig. 6.6 Scanning SQUID image of a 10 uc *p*-type (electrically insulating) $LaAlO_3/SrTiO_3$ sample at 4 K. Scale bar: 30 μm. Published in Ref. [185].

show a large variation from ~ 0 to ~ $10^{12}\,\mu_B$ mm^{-2}.

Figure 6.5(c) shows the large-area averaged moment density in each sample as a function of $LaAlO_3$ thickness. The data set clearly indicates, despite the strong sample-to-sample variation, the existence of a critical thickness of 3 uc for the formation of ferromagnetism,[*2] which is very similar to that for conductivity (Fig. 6.5(d), Ref. [40]).

6.3.2 Effect of the interface termination

It has been reported that the interface termination also has a strong impact on the properties of the $LaAlO_3/SrTiO_3$ interface (see Secs. 2.3.1 and 2.3.2). Most notably, the *p*-type (AlO_2/SrO) interface is electrically insulating, contrasting to the conducting *n*-type (LaO/TiO_2) interface [10, 72]. This asymmetry also implies that oxygen vacancies and intermixing are not the sole cause of the conductivity. We thus next examine the possible difference in ferromagnetism between the *n*-type and *p*-type interfaces.

Figure 6.6 shows a magnetometry image of a *p*-type $LaAlO_3/SrTiO_3$ sample with a $LaAlO_3$ thickness of 10 uc, fabricated with one monolayer of SrO inserted in between. It has been confirmed that the interface is electrically insulating; the room-temperature resistivity is above our measurement limit (> 10 MΩ). Contrasting to this, the ferromagnetic landscapes in Fig. 6.6 are qualitatively similar to those of the *n*-type (conducting) samples shown in Figs. 6.4(c) and (d). The averaged moment density of the *p*-type sample is estimated to be $6 \times 10^{10}\,\mu_B$ mm^{-2}, comparable to the *n*-type samples.

[*2] The 2.7 uc sample is composed of 2 and 3 uc regions, the latter region likely showing ferromagnetic patches.

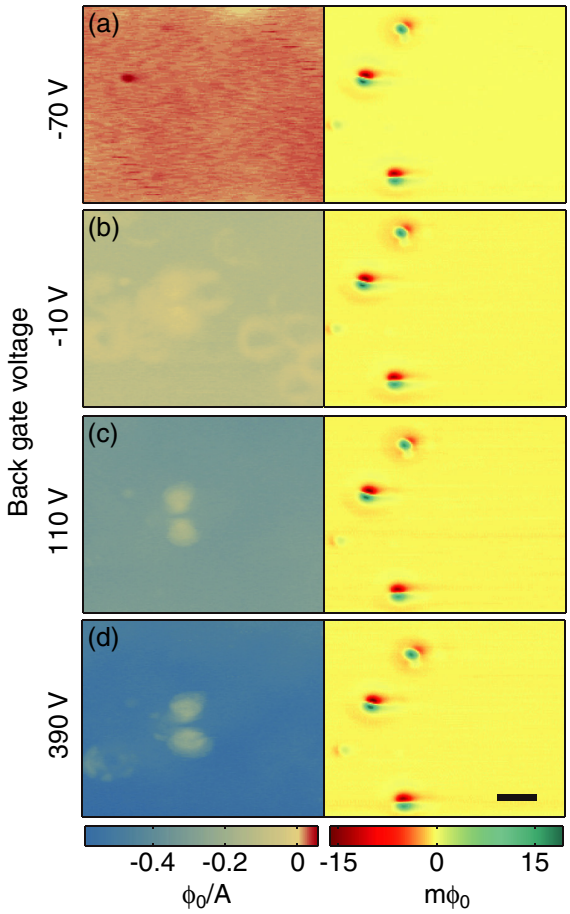

Fig. 6.7 Susceptometry (left) and magnetometry (right) images of the 5 uc $LaAlO_3/SrTiO_3$ sample with varying back-gate voltage, taken at 80 mK. (a) −70 V, (b) −10 V, (c) 110 V, (d) 390 V. Scale bar: 20 μm. Published in Ref. [186].

6.3.3 Electric field control

The electric field-effect has been applied for the $LaAlO_3/SrTiO_3$ interface to control the electronic properties, in particular with a back-gate geometry using the $SrTiO_3$ substrate as a gate dielectric [40–42]. Notably, the back gate geometry preserves access to the sample surface by scanning SQUID, enabling to examine the possible modulation of ferromagnetism with back-gate voltage.

Figures 6.7(a)–(d) shows susceptometry (left) and magnetometry (right) images of the 5 uc $LaAlO_3/SrTiO_3$ sample with varying gate voltage. The significant change of the susceptibility (left figures) confirms that back gating does modify superconductivity, as previously probed by electrical measurements [41]. In particular, no diamagnetic signal is observed with a back-gate voltage of −70 V [Fig. 6.7(a)], indicating that superconductivity is fully suppressed by the negative gate voltage. In contrast, the individual ferromagnetic patches are found to be insensitive to the gate voltage with a constant magnitude and orientation (right figures).

6.3.4 Discussion

To summarize the observations, magnetism appears only above a threshold $LaAlO_3$ thickness that is similar to the critical thickness for conductivity. No change in ferromagnetism is observed with SrO insertion or back-gate voltage, which on the other hand strongly modify the (super)conducting properties. The existence of a critical thickness for ferromagnetism indicates that a reconstruction driven by the polar discontinuity is likely necessary for the formation of magnetism. Note that there is a polar discontinuity also at the *p*-type interface (see Sec. 2.3.2; Ref. [73]). However, the correlation between ferromagnetism and (super)conductivity is not strong, indicating that *mobile* carriers at the interface are not necessary to generate magnetism. These results suggest that the magnetic moments are localized at the interface, decoupled from the conduction electrons.

Existence of localized carriers at the $LaAlO_3/SrTiO_3$ interface has been indicated both experimentally [174, 190–192] and theoretically [92, 93]. Note that the polar discontinuity picture expects a sheet carrier density of $\approx 3 \times 10^{14}$ cm^{-2} (half an electron per unit cell) [73], while the typical values by transport measurements are about an order of magnitude smaller [40, 87, 134]. Our observation suggest that these localized carriers contribute to the magnetic signal, although the microscopic origin of the ferromagnetic ordering remains to be explored [193].

6.4 Host of ferromagnetism

6.4.1 Outline of the spectroscopic investigation

It should be noted that scanning SQUID is not a surface sensitive measurement, and it cannot be fully determined whether the magnetism is really specific to the interface, or arises from cation/anion defects in the $LaAlO_3$ or $SrTiO_3$, all of which have been theoretically proposed [176–178, 182–184]. While absence of magnetic moment in the control samples (see Sec. 6.3, Fig. 6.5 in particular) has likely excluded significant contribution of impurities or defects, direct information regarding the host of the magnetism has not yet been obtained. Therefore, in order to further distinguish the theoretical ideas presented, it is of central importance to determine the microscopic nature of the observed ferromagnetism.

To address this issue, we applied element-specific techniques for this system, namely, synchrotron based x-ray absorption spectroscopy (XAS), x-ray magnetic circular dichroism (XMCD), and x-ray absorption linear dichroism (XLD). These measurements can uniquely determine whether the observed magnetization is from one of the constituent elements or from extrinsic impurities. All spectra were acquired by recording the total electron yield (TEY). As the maximum probing depth of TEY is approximately 5–10 nm, these measurements are surface-sensitive. Also, by measuring the angle dependence of the XMCD signal, which is proportional to $\boldsymbol{K} \cdot \boldsymbol{M}$ ($\boldsymbol{K}$ is the x-ray propagation vector and $\boldsymbol{M}$ denotes the magnetic moment), the direction of the magnetic moment can be determined. Moreover, owing to the high sensitivity of XMCD [194], a very small magnetic moment ($\sim 0.005 \mu_B$/atom) can be detect-

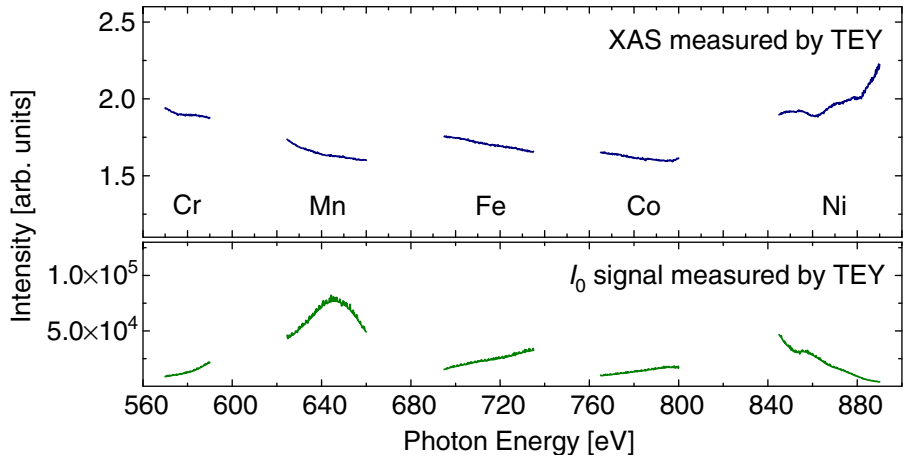

Fig. 6.8 XAS spectra of the 3.3 uc $LaAlO_3/SrTiO_3$ heterostructure. Sample signal (upper panel) are normalized by the incident beam signal I_0 (lower panel). Both I_0 and the sample signals were acquired by recording the total electron yield (TEY). Published in Ref. [187].

ed. All spectroscopic experiments were carried out in collaboration with Dr. Jun-Sik Lee and Prof. Chi-Chang Kao, at beamlines BL 10-1 and 13-1 at the Stanford Synchrotron Radiation Lightsource.

6.4.2 Titanium d_{xy} ferromagnetism

Probing possible impurities by XAS

Using XAS, possible presence of magnetic impurities in the $LaAlO_3/SrTiO_3$ samples was first examined. In general, ferromagnetic $3d$-transition metals (i.e., Cr, Mn, Fe, Co, and Ni) are the most likely candidates. Therefore, the scanned energy range was set from 560 eV to 890 eV; the presence of these candidate impurities can be detected via characteristic $2p \rightarrow 3d$ dipole transitions. Figure 6.8 shows the XAS spectra at Cr, Mn, Fe, Co, and Ni $L_{2,3}$-edges of the 3.3 uc $LaAlO_3/SrTiO_3$ sample (identical with that used in the scanning SQUID measurement presented in Sec. 6.3.1). Note that the signals (upper panel in the figure) via TEY were normalized by I_0 signals (lower panel in the figure).

No spectral features are observed at each $L_{2,3}$ edges, except in the case of Ni where it shows a dip near the energy positions corresponding to Ni absorption edges. If such behavior is due to the sample, the spectral feature should rather be a peak; it was found that the dip is due to the variation in I_0. These measurements thus confirms that the presence of $3d$ magnetic impurities in the probing volume of the sample is below the detection limit ($\sim 10^{12}$ atoms/cm^2) of our experiment.

Host of the magnetism by XMCD

In the absence of extrinsic magnetic impurities, interface ferrmagnetism is likely to originate from Ti atoms, as theoretically proposed [182, 183]. Therefore, we next performed Ti $L_{2,3}$-edges XMCD measurements on the same sample at 10 K with a magnetic field of 0.2 T applied.

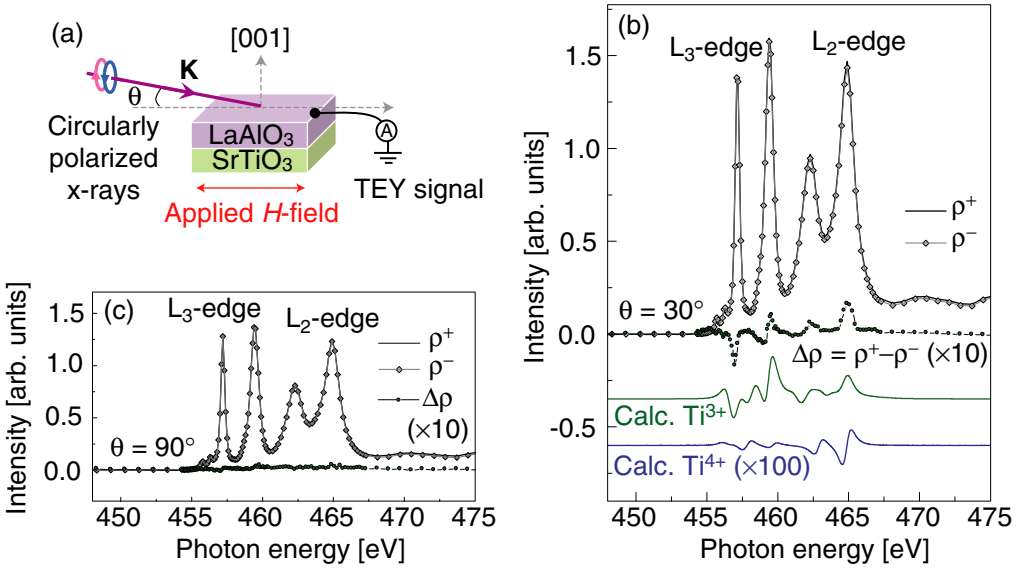

Fig. 6.9 (a) Schematic picture of the experimental configurations for the XMCD measurement. (b) XMCD spectra of the 3.3 uc $LaAlO_3/SrTiO_3$ sample for the in-plane geometry at 10 K. The $\Delta\rho$ shown is the result of averaging 20 scans. Simulated spectra by atomic multiplet calculations (see text and Ref. [195] for details) are also shown. (c) XMCD spectra for the out-of-plane geometry. The sample was zero-field cooled and measured in a constant applied field of 0.2 T. Published in Ref. [187].

The experimental geometry is shown in Fig. 6.9(a), where θ is the angle between $\boldsymbol{K}$ and the sample surface. θ was set at 30° (90°) to optimize the observation of an in-plane (out-of-plane) magnetic moment.

Figure 6.9(b) shows absorption spectra of the 3.3 uc $LaAlO_3/SrTiO_3$ sample for the $\theta = 30°$ geometry, where ρ^+ and ρ^- represent the parallel and anti-parallel alignment of the magnetization direction with the photon helicity vector, respectively. A Ti XMCD signal is clearly seen, although the dichroism ($\Delta\rho = \rho^+ - \rho^-$) is very weak. The Ti $\Delta\rho$ signal completely disappears for the $\theta = 90°$ geometry [Fig. 6.9(c)], indicating that the ferromagnetic Ti moment lie in-plane. For the in-plane geometry, $\Delta\rho$ is $\sim$ 0.5% of the total absorption signal, which corresponds to a total magnetic moment of $\sim$ 0.01–0.1 μ_B/Ti, with a large error bar mainly originating from the uncertainty in the detailed distribution of the Ti moments. The magnetic behavior observed by Ti XMCD is consistent with the scanning SQUID study of the same sample presented in Sec. 6.3.1, when averaging the observed inhomogeneous dipoles. The total moment estimated spectroscopically is also within the upper bound of magnetism based on polarized neutron reflectometry measurements [181].

As the $3d^0$ configuration of Ti^{4+} in bulk $SrTiO_3$ cannot generate a ferromagnetic polarization, the XMCD signal is expected to originate from Ti^{3+}. To confirm this, atomic multiplet calculations [195] were used to simulate XMCD spectra for the Ti^{3+} and Ti^{4+} states. The calculations were performed with 10 Dq = 1.85 eV, Hubbard U_{dd} = 1.5 eV, and charge-transfer energy Δ = 1.2 eV for the Ti^{3+} state under O_h symmetry. The calculated Ti^{3+} spectrum agrees

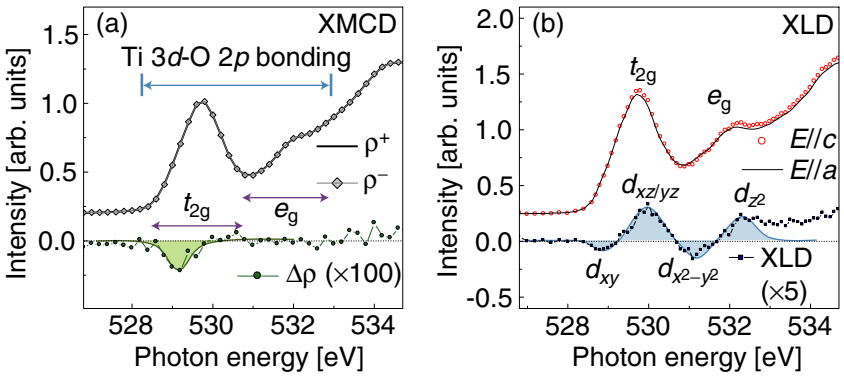

Fig. 6.10 (a) O K-edge XMCD in the 3.3 uc $LaAlO_3/SrTiO_3$ sample at 10 K with $\theta = 30°$. The green shaded region indicates the Ti ferromagnetism at the t_{2g} level. (b) O K-edge XLD. The blue shaded regions indicate the Ti orbital states. Published in Ref. [187].

well with the experimental result, as shown in Fig. 6.9(b).

Orbital character

The orbital character of the additional electron in the Ti^{3+} state was next determined by XMCD and XLD. Figure 6.10(a) shows XMCD spectra of the 3.3 uc $LaAlO_3/SrTiO_3$ sample at the O K-edge. Note that orbitally-selective magnetic polarization should be present in the oxygen neighboring the titanium, due to O $2p$–Ti $3d$ hybridization. A clear dichroism feature is observed around 529.2 eV, corresponding to the oxygen bonding with the Ti t_{2g} band, whereas the e_g band feature is around 532.5 eV. Figure 6.10(b) shows XLD spectra of the same sample at the O K-edge. Using the variation of the XLD signal, the contribution of each orbital character can be assigned. In particular, the d_{xy} contribution is around 529 eV, just where the O K-edge dichroism is observed. These observations indicate that the ferromagnetic Ti is associated with the d_{xy} orbital in the t_{2g} band.

6.4.3 Discussion

Density-functional calculations indicate that the lowest energy state at the $LaAlO_3/SrTiO_3$ interface has the d_{xy} orbital character, and strongly confined at the interface, mostly on the first TiO_2 layer [93, 196, 197]. The d_{xy} electrons account for most of the charge in this system, and due to the strong two-dimensional nature, they are likely to be Anderson localized even with a small amount of disorder, which is common in two-dimensional systems [198]. The observed Ti d_{xy} ferromagnetism thus further support the interpretation that these localized carriers contribute to ferromagnetism. However, due to the O $2p$–Ti $3d$ hybridization, a clear delineation of the source of magnetism between Ti and oxygen cannot fundamentally be made. Theoretical studies based on a relatively high defect concentration indicate the importance of oxygen vacancies to stabilize ferromagnetic states [177, 178], which may be relevant for the high magnetic moments observed elsewhere [173], much larger than observed in this study.

Comparing the magnetic properties of samples with different oxygen stoichiometry is thus

expected to be helpful to further distinguish the theoretical ideas. It should also be useful to examine whether a larger external field affect the ferromagnetism; it has very recently been proposed that the zero-field spin order is a "spiral," which has no net magnetization, and the small and randomly distributed magnetic moments observed by scanning SQUID may be related to defects that break the spiral structure [184]. The spiral ground state is expected to transform into a ferromagnetic state with a large enough field applied [184], which is another possibility to explain the discrepancy in the moment density.

6.5 Conclusion

In summary, we characterized the magnetic properties of the $LaAlO_3/SrTiO_3$ heterostructure using multiple high sensitivity techniques. The correlation between ferromagnetism and (super)conductivity indicated that the localized carriers contribute to magnetism, decoupled from the itinerant electrons, both of which are likely induced by the polar discontinuity. We found evidence for in-plane ferromagnetic order at the interface, with Ti d_{xy} orbital character, further supporting that the localized carriers contribute to ferromagnetism.

While more work is needed to further distinguish between the theories proposed [176–178, 182–184] and to understand what mediates the ferromagnetic interaction, the ferromagnetism at the interface reported here implies that it likely influences the superconductivity. Exotic superconducting phenomena may therefore emerge; for example, it is theoretically suggested that a small, but finite magnetic field can enhance the superconductivity [183], which rather suppresses in the case of conventional superconductors. A preliminary result to support the enhancement has already been presented [199], demonstrating a striking example of emergent phenomena at oxide interfaces.

Chapter 7

Growth of High-Quality $SrMoO_3$ Thin Films

7.1 Introduction

7.1.1 Comparison with $LaAlO_3/SrTiO_3$

In this Chapter, we present fabrication and characterization of high-quality $SrMoO_3$ thin films. The $SrMoO_3$ thin film is contrasting to the $LaAlO_3/SrTiO_3$ heterointerface we have focused on so far, in the following senses. First, from a fundamental perspective, $SrMoO_3$ is a metal, whereas $LaAlO_3$ is an insulator and $SrTiO_3$ is a wide-gap semiconductor. The $LaAlO_3/SrTiO_3$ interface correspondingly has a relatively low sheet carrier density of $\sim 10^{13}$ cm^{-2}, as presented in the last Chapters. While it is possible to induce more electrons in $SrTiO_3$, for example by electric field effect [200], it is usually inevitable to simultaneously reduce the electron mobility (see Sec. 2.2.1, Fig. 2.1(d) in particular), making the system "dirty." $SrMoO_3$ may provide a complementary approach to the study on high density and clean regime; its highest conductivity among perovskite oxides [21] suggests that the high density electrons in this material[*1] have a high mobility particularly at low temperatures.

From a relatively practical perspective, $SrMoO_3$ is much less actively studied compared to $LaAlO_3/SrTiO_3$. This does not mean that $SrMoO_3$ has no fascinating physical property; as briefly reviewed in Sec. 2.4.1, $SrMoO_3$ has many potential advantages for studying the fundamentals of strongly correlated interfaces as well as for device applications. Studies of this material are limited rather because of the difficulty in growth of this material that requires extremely strong reducing conditions [117]. As we have demonstrated the importance of fundamental growth studies with the $LaAlO_3/SrTiO_3$ interface in the last Chapters, this background motivates the development of the fabrication process of $SrMoO_3$ thin films, which should provide important basis for the more detailed study on this potentially interesting material.

[*1] Considering the typical electron density in a metal of $\sim 10^{22}$–10^{23} cm^{-3} and assuming that the film thickness can be reduced down to 1 nm, the sheet carrier density is estimated to be $\sim 10^{15}$–10^{16} cm^{-2}.

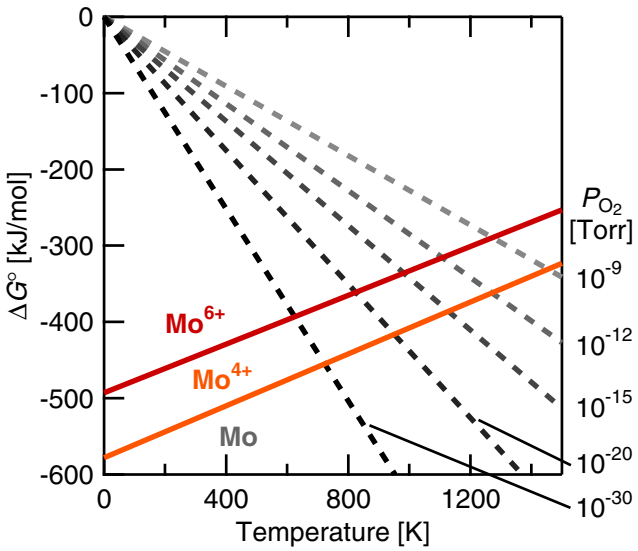

Fig. 7.1 Ellingham diagram for Mo, which indicates stable conditions of various valence states as the oxide. Calculated following Ref. [201].

7.1.2 Previous studies on $SrMoO_3$

As briefly reviewed in Sec. 2.4.2, $SrMo^{4+}O_3$ can be stabilized only under very low oxygen partial pressures [117], which makes fabrication of this material difficult. This can also be understood based on the Ellingham diagram shown in Fig. 7.1, where stable valence states of Mo are mapped for the simple metal oxide in terms of standard-state Gibbs energy (proportional to oxygen partial pressure) and temperature [201]. The diagram indicates that at typical growth temperature ($\sim$ 1000 K), Mo^{4+} can be stabilized in the oxygen pressure range of $\sim 10^{-15}$–10^{-20} Torr.

In spite of this difficulty, there are still a considerable number of reports on growth and electrical properties of $SrMoO_3$ in various forms [21, 118–120, 202]. Figure 7.2 summarizes the temperature dependence of the resistivity of $SrMoO_3$ reported previously, which also include results of two films grown in this study (details are explained later). Most notably, the resistivity of the thin films is much higher than that of the bulk single crystal, by almost two orders of magnitude at low temperature. The residual resistivity ratio, RRR $\equiv R(300\text{ K})/R(2\text{ K})$ (R is the resistivity),[*2] of the thin films is also much smaller, indicating that the quality of the thin films is degraded compared to the bulk single crystal.[*3]

In this Chapter, we aim to improve the quality of $SrMoO_3$ thin films by systematically tun-

[*2] Residual resistivity in the strict sense is $R(0\text{ K})$, but the absolute zero temperature is impossible to realize. Therefore, a resistance at low, but finite temperatures (2–10 K) is used in practice, where the resistance has small temperature dependence and is usually very close to $R(0\text{ K})$.

[*3] Since residual resistivity usually increases with the addition of disorder (impurity, crystallographic defects, etc), larger RRR values indicate better quality. Note that RRR can be a function of film thickness as well, since surface scattering can also affect the resistivity.

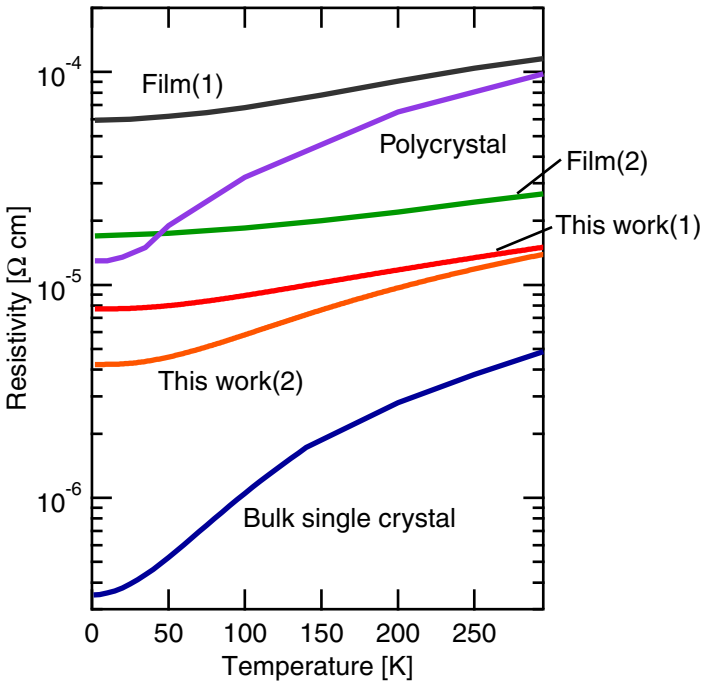

Fig. 7.2 Temperature dependence of the resistivity of bulk $SrMoO_3$ (polycrystal: Ref. [202], single crystal: Ref. [21]) and thin films (Film(1): Ref. [119], Film(2): Ref. [120]). Details of the films grown in this work are described in Sec. 7.4.

ing the growth parameters. Our main finding is that the interaction of ablated species with argon (inert gas) is a key growth parameter to simultaneously optimize the conductivity and the surface flatness. For comparison, the results of the growth in vacuum are first described in Sec. 7.3, showing the difficulty in the simultaneous optimization of structural and electrical properties. As presented in Sec. 7.4, the surface flatness is improved by growing the film in high pressure argon, without affecting the electrical properties. As a result, a $SrMoO_3$ film with a flat surface and a higher conductivity than reported previously is successfully grown. The resistivity of this film is shown also in Fig. 7.2 (This work(1)). By tuning the growth temperature, despite the slight degradation in surface flatness, the conductivity is further improved (Fig. 7.2, this work(2)). In particular, the largest RRR realized is 3.32, significantly larger than the films grown by other groups previously (< 2.0) [118–120].

7.2 Experimental details

The samples were fabricated by PLD (Sec. 3.2). Each $SrMoO_3$ film was grown on a 5×5 mm^2 $(LaAlO_3)_{0.3}$-$(Sr_2AlTaO_6)_{0.7}$ (LSAT) (001) substrate (Shinkosha Co.). The substrates were first *ex situ* preannealed at 1000 °C in air for 1 h to facilitate surface diffusion to create an atomically flat surface. Before growth, the substrates were also *in situ* preannealed at 900 °C in the base pressure of the chamber for 30 mins to degas contamination (see also Sec. 3.2.3). The variable growth parameters were the growth temperature T_g and the argon partial pressure P_{Ar}. Unless

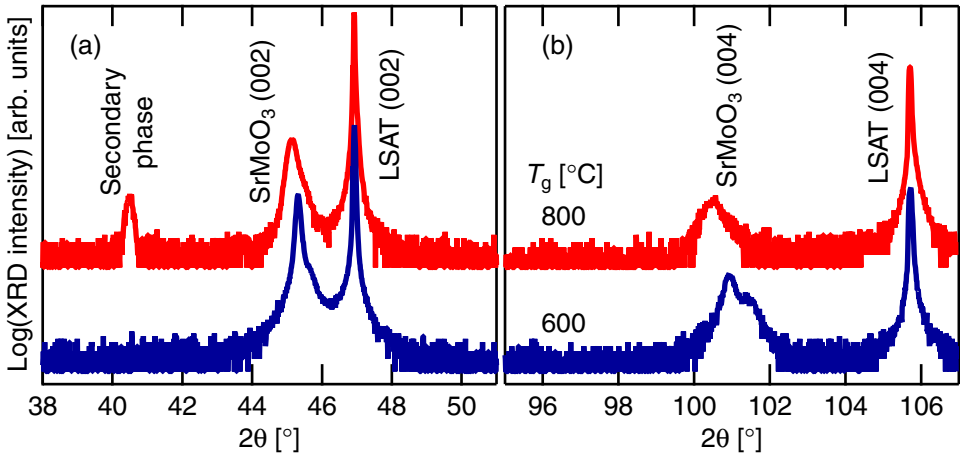

Fig. 7.3 XRD θ–2θ patterns of the $\approx$ 100 nm $SrMoO_3$ thin films on LSAT (001) grown at different temperatures in the base pressure, around (a) (002) and (b) (004) reflections.

otherwise indicated, the laser energy was 31 mJ, and the laser beam was imaged to a square spot of area 4.5 mm^2 on the polycrystal $SrMoO_x$ target without the zoom stage (see Sec. 3.2.1 for details of the optics). The laser repetition rate was fixed at 1 Hz. The film thickness was $\approx$ 50 nm, unless otherwise indicated, as measured by AFM.[*4] No RHEED oscillation was observed in any of the growth conditions, preventing *in situ* calibration of the film thickness. After growth, the samples were cooled to room temperature in the growth pressure.

The film surface was characterized by *in situ* RHEED (Sec. 3.2.4) and *ex situ* AFM (Sec. 3.4), and the crystal structure by XRD (Sec. 3.3). The transport measurements were carried out in a PPMS (Sec. 3.5), with a quasi-DC bias current of 100 μA, unless the sample resistance was too high. Most samples showed high conductivity (raw resistance $\sim$ 1–10 Ω), but there were a few films which had somewhat lower conductivity. For those high resistivity samples, the bias current was limited by the maximum voltage (95 mV) or power (1000 μW). Resistivity was measured assuming that the samples were homogeneous and current flowed throughout the film thickness. Note that LSAT is known to be highly insulating even after treated under extremely strong reducing conditions [161], and thus the contribution of the LSAT substrates to the transport properties is negligible.

7.3 Growth in vacuum

7.3.1 Growth temperature dependence

We first examined whether the oxygen partial pressure at the base pressure of our chamber is low enough to stabilize $SrMo^{4+}O_3$. Figure 7.3 shows XRD θ–2θ patterns of $\approx$ 100 nm $SrMoO_3$/LSAT (001) samples grown at different temperatures at the base pressure. Clear

[*4] The substrate was fastened on the holder with clamps, which blocked deposition and created a step in the film. The film thickness was estimated by measuring the height of the step.

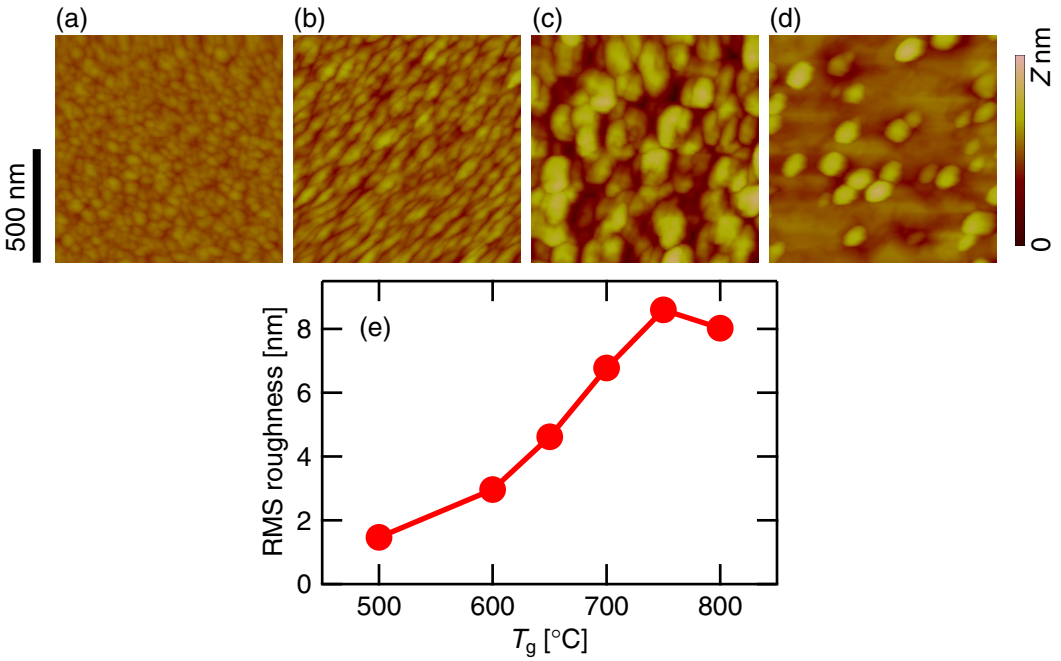

Fig. 7.4 AFM surface topography of the $SrMoO_3$ films grown at different temperatures in the base pressure. (a) T_g = 500 °C, (b) 600 °C, (c) 700 °C, and (d) 800 °C. Height scale Z = 50 nm for (a)–(c), 100 nm for (d). (e) RMS surface roughness as a function of growth temperature. Lines are guides to the eye.

single-crystalline and oriented $SrMoO_3$ peaks are observed, indicating that the base pressure is low enough to stabilize Mo^{4+}, perhaps with the contribution of epitaxial stabilization. Due to the large thickness and lattice mismatch, the films are partially relaxed, as indicated by the slight splitting of the peaks, in particular clearly seen in the (004) reflection [Fig. 7.3(b)]. Although the partial relaxation induces a large error bar, the out-of-plane lattice constant of the $SrMoO_3$ films are estimated to be 4.10 Å (T_g = 800 °C sample) and 4.05 Å (T_g = 600 °C sample), respectively.

As shown in Fig. 7.3(a), the T_g = 800 °C sample shows a small, but significant diffraction signal that is clearly different from those of $SrMoO_3$, indicating the existence of secondary phase. XRD cannot identify what the secondary phase is, however, since only this small (002)-like peak is observed, which is not consistent with the diffraction patterns of typical candidates of the secondary phase (SrO_x, MoO_x, $SrMo^{6+}O_4$). The secondary phase is thus perhaps single crystalline and has an epitaxial relationship with the perovskite structure, which reduces the number of the diffraction peaks in the θ–2θ pattern and modifies the pattern from the bulk reference via strain.

Having confirmed that the reducing conditions (P_{O_2}, T_g) are sufficient to stabilize $SrMo^{4+}O_3$, more detailed growth temperature dependence of the film structure and the electrical properties was next investigated. Figures 7.4(a)–(d) show the AFM surface topography of $SrMoO_3$ films grown at different temperatures in the base pressure of the chamber. All surfaces were found to be rough, showing island features. As T_g increased, the island size (diameter and height)

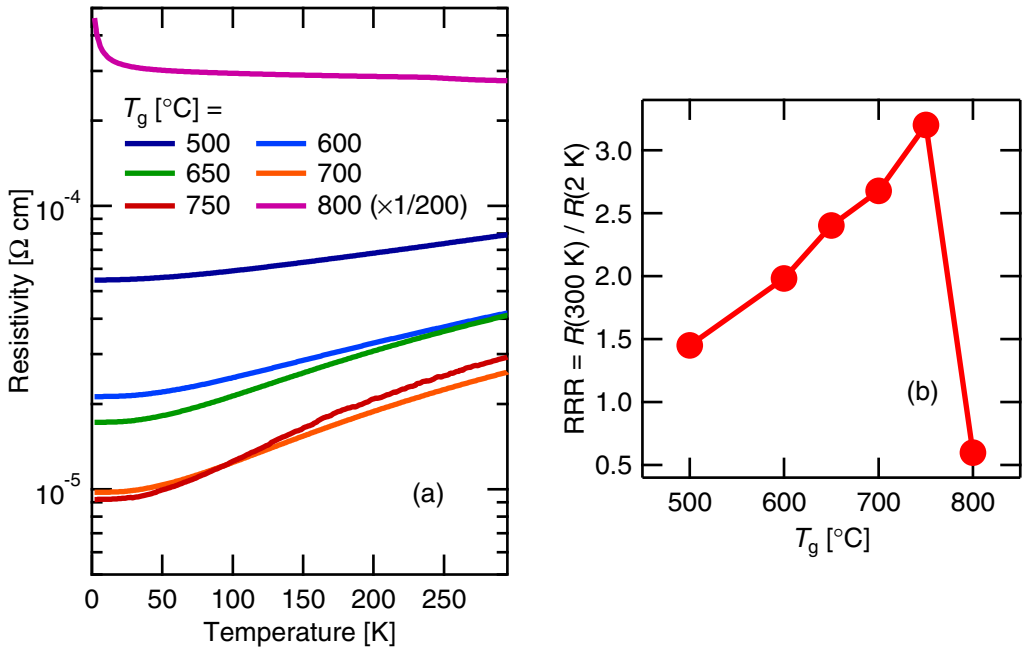

Fig. 7.5 (a) Temperature dependence of the resistivity of the $SrMoO_3$ films grown at different temperatures in the base pressure. (b) Residual resistivity ratio as a function of growth temperature. Lines in (b) are guides to the eye.

also increased, and correspondingly the average surface roughness also increased [Fig. 7.4(e)]. The *in situ* RHEED patterns showed a consistent trend with this AFM result; the initial two-dimensional streak pattern of the substrate quickly disappeared at the beginning of growth, and three-dimensional patterns appeared within $\approx$ 1 min (corresponding to a nominal film thickness of $\sim$ 1.5 nm), with no significant change after that.

Figure 7.5(a) shows the temperature dependence of the resistivity of the films. RRR of the films is summarized in Fig. 7.5(b). Up to T_g = 750 °C, higher T_g resulted in higher conductivity and RRR.[*5] This trend is consistent with thermodynamical considerations; as seen in the Ellingham diagram [Fig. 7.1], at fixed P_{O_2}, a thermodynamically stronger reducing condition is realized at higher T_g, and thus a higher-quality $SrMoO_3$ film can likely be grown. A candidate of the competing factor which induces the peak at T_g = 750 °C is the degassing of the chamber, which becomes stronger as T_g increases and correspondingly the whole chamber gets hotter (see Sec. 3.2.3, Fig. 3.4 in particular).

These results show that the surface flatness and the conductivity of the $SrMoO_3$ films currently cannot be optimized simultaneously: the former is improved by reducing T_g, while the latter by increasing. In the following, we examine if they can be simultaneously optimized by controlling other growth parameters.

[*5] As the rough surface prevented a precise thickness evaluation, each resistivity data set may have a nontrivial systematic error originating from the uncertainty in thickness normalization. Apparently the change of the resistivity with T_g is slightly random, most likely because of this thickness uncertainty.

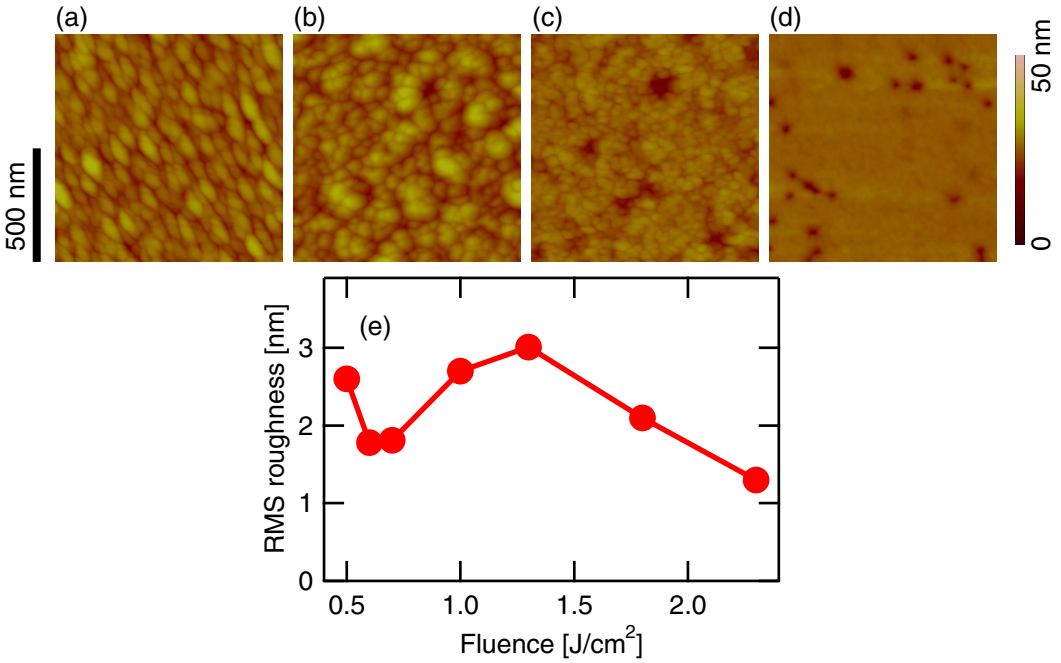

Fig. 7.6 AFM surface topography of the $SrMoO_3$ films grown using different laser fluences at T_g = 600 °C in the base pressure. (a) 0.5 J/cm^2, (b) 1.3 J/cm^2, (c) 1.8 J/cm^2, and (d) 2.3 J/cm^2. (e) RMS surface roughness as a function of laser fluence. Lines are guides to the eye.

7.3.2 Effect of the laser parameters

As explained in Sec. 4.1.2, the character of the ablating laser is well known in oxides to be crucial to obtain precisely controlled film stoichiometry, which is very likely to affect the conductivity. The laser fluence also modifies the plume kinetics, which is likely an important parameter to control the surface roughness. Therefore, we next examine the effect of the laser fluence on the surface morphology and the conductivity of $SrMoO_3$ films.

Figures 7.6(a)–(d) show AFM surface topography of $SrMoO_3$ films grown at T_g = 600 °C using different laser fluences. The laser spot sizes were 4.5 mm^2 for 0.5 J/cm^2 (and 0.7 J/cm^2), 3.2 mm^2 otherwise.[*6] As the fluence is increased, the island size decreases, with holes appearing at the same time. The density of the holes increases with fluence; as a result, the overall film roughness is not largely improved, as shown in Fig 7.6(e). Note that AFM does not precisely measure the size and depth of such holes, due to the finite curvature of the probe (see Sec. 3.4), and thus the depth of the holes might be underestimated.

Figure 7.7(a) shows the temperature dependence of the resistivity of the films. RRR of the films is summarized in Fig. 7.7(b). The apparently non-monotonic variation of the resistivity

[*6] As the controllable range of the laser energy by the variable attenuator (see Sec. 3.2.1 for details of the optics) was limited, changing the spot size was also necessary to control the fluence in a wide range.

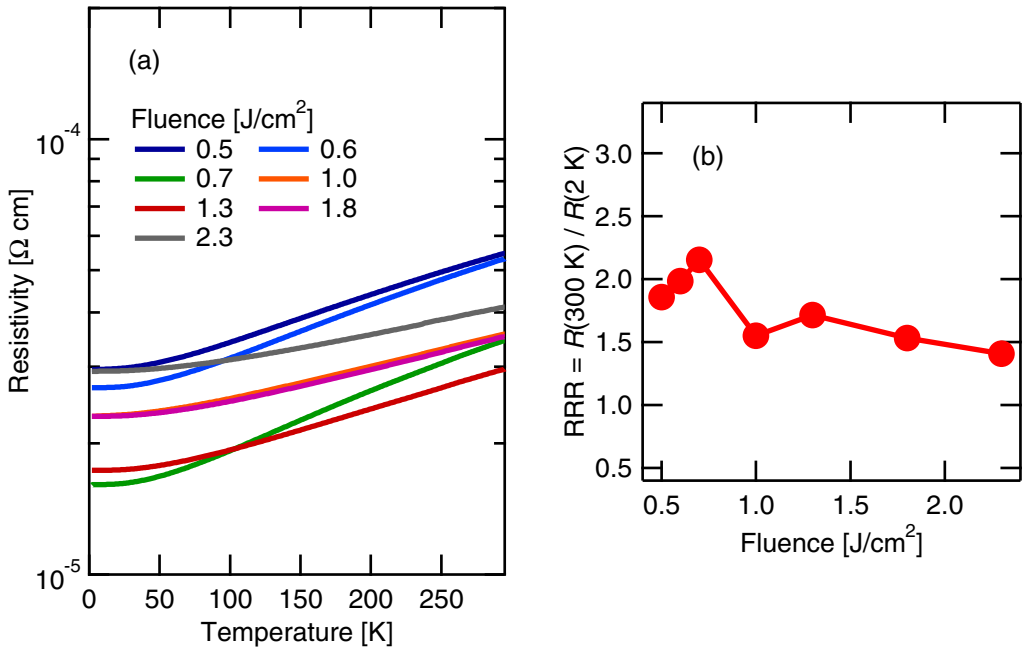

Fig. 7.7 (a) Temperature dependence of the resistivity of the $SrMoO_3$ films grown using different laser fluences at T_g = 600 °C in the base pressure. (b) Residual resistivity ratio as a function of laser fluence. Lines in (b) are guides to the eye.

with the fluence is likely due to the uncertainty in thickness normalization.[*7] Except at the lowest fluence regime, higher fluences result in lower RRR, and the highest RRR is obtained at a relatively low fluence of 0.7 J/cm^2. This trend also shows a weak, but significant anti-correlation with the surface flatness, which is improved (although not largely) by increasing the fluence. Therefore, these results again show that in vacuum, the surface flatness and the conductivity of the $SrMoO_3$ films cannot be simultaneously optimized.

7.4 Growth in argon

7.4.1 Motivation for growth in inert gas

We next examine the possible effect of argon. Argon is an inert gas, and thus it does not affect the reducing thermodynamic condition required for growth of $SrMoO_3$. Nevertheless, when the pressure (density) of the argon gas is high, the ablated species are scattered by the gas molecules before reaching the substrate. Therefore, argon gas pressure is another growth parameter to modify the plume kinetics and stoichiometry, which are expected to have an effect on the surface flatness and the conductivity of the $SrMoO_3$ films, possibly enabling the simultaneous optimization of them.

It should also be noted that argon is known empirically to be effective for growth of some

[*7] See Footnote ∗5.

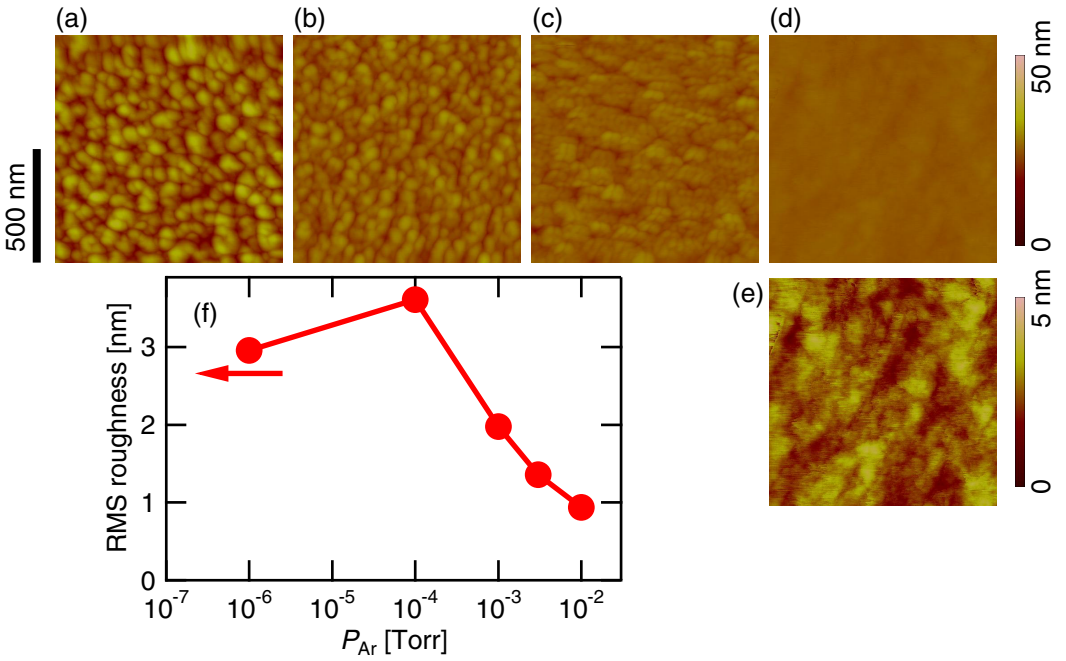

Fig. 7.8 AFM surface topography of the $SrMoO_3$ films grown at T_g = 600 °C in different Ar partial pressures. (a) $P_{Ar} = 1 \times 10^{-4}$ Torr, (b) 1×10^{-3} Torr, (c) 3×10^{-3} Torr, and (d) 1×10^{-2} Torr. (e) Same data in (d) displayed in a different height scale. (f) RMS surface roughness as a function of Ar partial pressure. For clarity, the $P_{Ar} \sim 0$ sample is plotted at 10^{-6} Torr. Lines are guides to the eye.

materials. For example, Krockenberger *et al.* have shown that in order to grow high-quality Sr_2RuO_4 films, precise control of oxygen *and* argon partial pressures is required; the former alone does not work [203]. Moreover, the effectiveness of argon for growth of $SrMoO_3$ has already been suggested by Radetinac *et al.* [120]: they have grown a relatively high-quality $SrMoO_3$ film in P_{Ar} = 1 mTorr, which shows a fairly high conductivity (see Fig. 7.2). As Radetinac *et al.* [120] have not explicitly presented the P_{Ar} dependence of the film quality, it is not fully clear whether the plume–ambient gas interaction is really the key; they mention that rather than argon itself, finite impurities in the gas might be more relevant. Therefore, it is of central importance to examine P_{Ar} dependence, to clarify the reason why argon is effective for growth of this material.

7.4.2 Effect on the surface morphology

Figures 7.8(a)–(d) show AFM surface topography of $SrMoO_3$ films grown at 600 °C in different P_{Ar}. As P_{Ar} increased, the island size became smaller, and correspondingly the surface roughness decreased, as summarized in Fig. 7.8(f). In particular, the film surface grown in the highest P_{Ar} = 10 mTorr was flat in nanometer-scale, although the roughness was still significantly larger than the $SrMoO_3$ unit cell height [Fig. 7.8(e)]. Contrasting to the laser parameter dependence (Sec. 7.3.2), the flat surface showed no obvious holes.

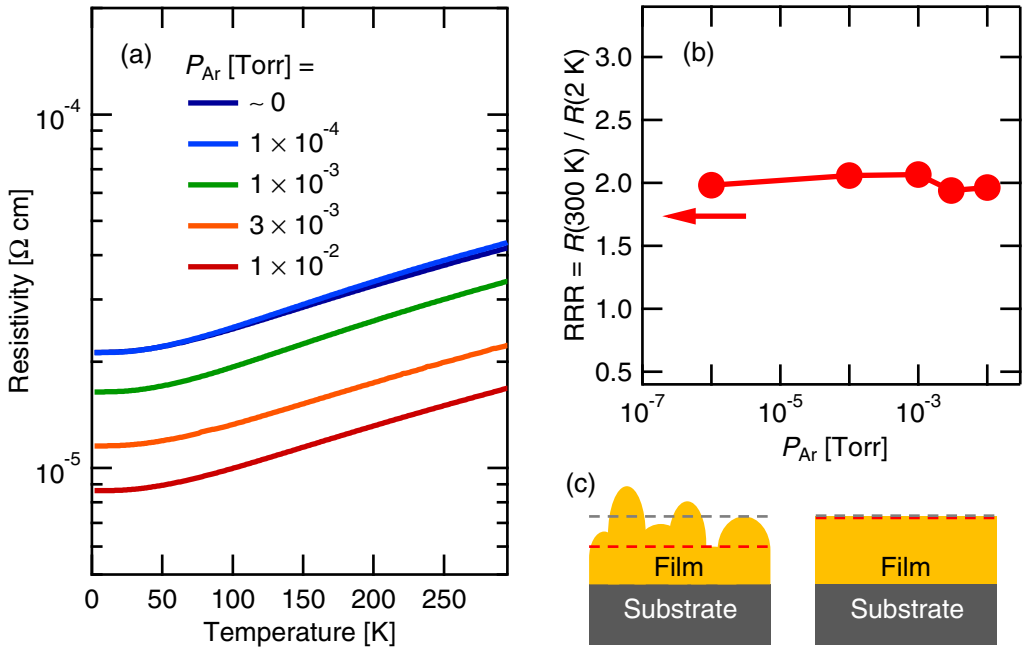

Fig. 7.9 (a) Temperature dependence of the resistivity of the $SrMoO_3$ films grown at T_g = 600 °C in different Ar partial pressure. (b) Residual resistivity ratio as a function of Ar partial pressure. For clarity, the $P_{Ar} \sim 0$ sample is plotted at 10^{-6} Torr. Lines in (b) are guides to the eye. (c) Schematic illustration of rough (left) and flat (right) films. Dashed lines denote the macroscopically averaged thickness (gray) and the electrically effective thickness (red), respectively.

It should be noted that the effect of argon is significant only above ~ 1 mTorr: the $P_{Ar} = 10^{-4}$ Torr sample showed a rough surface slightly worse than the $P_{Ar} \sim 0$ sample [Fig. 7.8(f); see also Figs. 7.4(b) and 7.8(a)]. The mean free path of the ablated species at P_{Ar} = 1 mTorr is about 55 mm [201], which corresponds to the substrate–target distance in our chamber. This strongly indicates that the plume–ambient gas interaction, rather than the impurities in the gas, is important to obtain the flat surface.

7.4.3 Transport properties

Figure 7.9(a) shows the temperature dependence of the resistivity of the films grown in different P_{Ar}. RRR of the films is summarized in Fig. 7.9(b). The transport properties were essentially not affected by P_{Ar}; the decrease of the resistivity is likely because of better normalization of the film thickness, which is enabled by the flat surfaces achieved. As schematically shown in Fig. 7.9(c), when the surface is rough, the electrically effective thickness may be smaller than the macroscopically averaged thickness.

This is contrasting to the films grown in vacuum, which showed a fairly strong anti-correlation between the surface flatness and the conductivity, as presented in Sec. 7.3. It is also important to note that the resistivity of the film grown in argon is significantly improved from the previous reports, as already summarized in Fig. 7.2 (This work(1)). As explained in

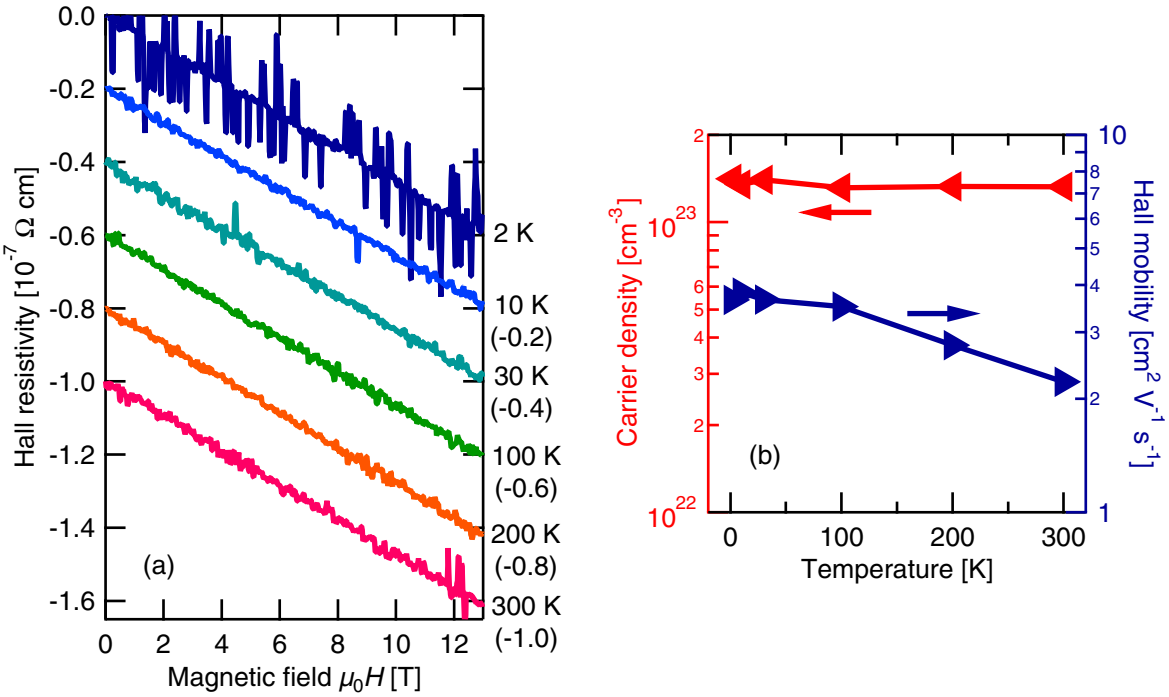

Fig. 7.10 (a) Hall effect of the 40 nm $SrMoO_3$ film grown at T_g = 600 °C in P_{Ar} = 10 mTorr. Numbers in parentheses indicate the vertical offset for each data set. (b) Carrier density and mobility, evaluated from the Hall effect, as a function of temperature. Lines in (b) are guides to the eye.

Sec. 7.3.1, when grown in vacuum, higher T_g resulted in higher conductivity in the film. Essentially the same T_g dependence was found also when grown in argon; the $SrMoO_3$ film grown at T_g = 750 °C in P_{Ar} = 10 mTorr showed a little rougher surface (RMS roughness ≈ 2 nm), but a better conductivity, particularly in terms of the large RRR of 3.32. The conductivity of this film is also shown in Fig. 7.2 (This work(2)).

Having grown high-quality $SrMoO_3$ thin films which have a flat surface and a high conductivity, we next characterized the transport properties in more detail. Figure 7.10(a) shows the Hall effect of the 40 nm thick $SrMoO_3$ film grown at T_g = 600 °C in P_{Ar} = 10 mTorr, measured at different temperatures. The larger noise at 2 K is extrinsic; during this cooldown the system had a minor problem, and the temperature stability was slightly worse at the lowest temperature. The Hall resistivity is linear with the magnetic field, contrasting to magnetic materials, which often show anomalous Hall effects [204]. The linear Hall effect is thus consistent with the Pauli-paramagnetism of $SrMoO_3$ [107].

The carrier density and the mobility were evaluated from the Hall effect, as summarized in Fig. 7.10(b). The carrier density was found to be ≈ 1.3×10^{23} cm^{-3} and have no significant temperature dependence. This value is about four times larger than 3.19×10^{22} cm^{-3}, which is expected if two electrons are induced per unit cell.[*8] The Hall mobility was found to be

[*8] Note that $SrMo^{6+}O_4$ is an insulator [205, 206].

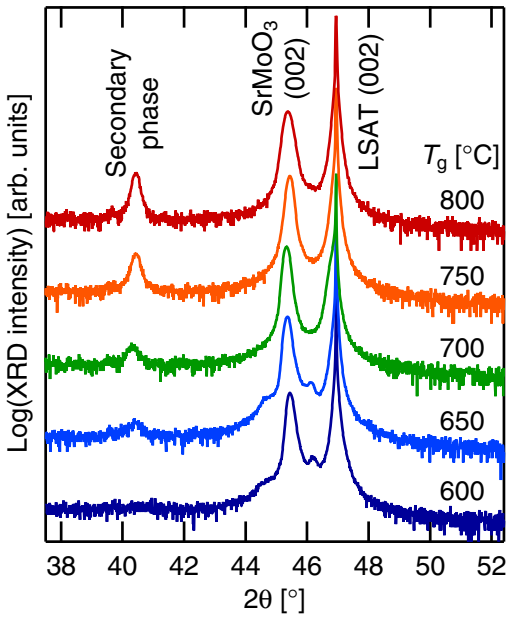

Fig. 7.11 XRD θ–2θ patterns of the $SrMoO_3$ thin films on LSAT (001) grown at different temperatures in $P_{Ar} = 10$ mTorr. Shoulders around the film peak of the $T_g = 600$ °C and 650 °C samples are thickness fringes.

$\approx 3.7\ cm^2V^{-1}s^{-1}$ at 2 K. As the resistivity of the film is still considerably higher than the bulk single crystal particularly at low temperatures (see Fig. 7.2), there probably remains room to improve the mobility. Using the low temperature resistivity of the bulk single crystal of $\approx 0.35\ \mu\Omega\,cm$ from Ref. [21], and the carrier density of $\approx 1.3 \times 10^{23}\ cm^{-3}$ obtained in this study, a mobility of $\sim 140\ cm^2V^{-1}s^{-1}$ is expected to be achievable.

7.4.4 Discussion

Next we discuss the possible reason why the argon gas improves the quality of the $SrMoO_3$ films. As mentioned in Sec. 7.4.2, the existence of a pressure threshold of $\sim$ 1 mTorr indicates that the scattering between the ablated species and the argon gas is important, as the corresponding mean free path is close to the substrate–target distance in our chamber. The scattering modifies the kinetic energy of the ablated species, the expansion of the plume, and the plume stoichiometry (as certain species may be preferentially more scattered than the others) [207, 208]. The changes of the first two parameters are expected to be small at 1 mTorr, as they become significant when the mean free path is much shorter (scattering occurs much more frequently) [207, 208]. The stoichiometry modulation by preferential scattering is thus more likely to be relevant to the quality improvement. More specifically, oxygen stoichiometry in the plume is perhaps the most critical; considering the similar masses of Sr (88 amu) and Mo (96 amu), and the much lighter mass of O (16 amu), the Sr/Mo ratio is not likely to be strongly modulated by argon, but the change of the (Sr + Mo)/O ratio can be significant [209].

Although the conductivity of the $SrMoO_3$ thin films grown in this study is improved com-

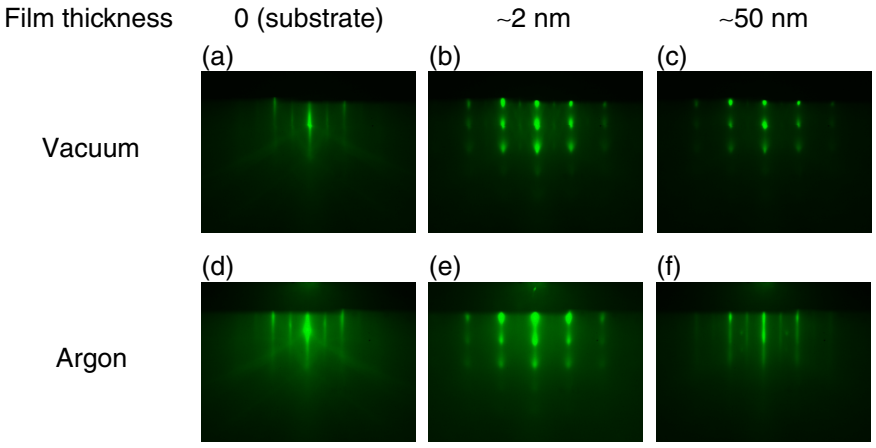

Fig. 7.12 RHEED patterns during growth of $SrMoO_3$ in (a)–(c) the base pressure and (d)–(f) P_{Ar} = 10 mTorr. (a), (d) Before growth, (b), (e) after deposition of ~ 2 nm and (c), (f) ~ 50 nm.

pared to those grown by other groups, the low temperature conductivity and RRR are still considerably lower than the bulk single crystal (see Fig. 7.2), indicating that the bulk-equivalent quality has not been achieved yet. A likely limiting factor is the secondary phase, as briefly mentioned in Sec. 7.3.1. The secondary phase has been found not to be suppressed by argon: the XRD θ–2θ patterns [Fig. 7.11] indicates that, when grown at relatively high temperatures, the $SrMoO_3$ films grown in argon also have the secondary phase. Since the higher temperature means thermodynamically stronger reducing conditions, the secondary phase could originate from decomposition of $SrMoO_3$. However, considering that the base pressure of our chamber has a finite amount of oxygen (see Sec.3.2.3, Fig. 3.4 in particular), this is not so likely; rather, the degassing of the chamber (impurities) may be more relevant. Identifying the secondary phase, for example by electron microscopy, is thus of particular importance, which is expected to give clues on how to suppress the secondary phase formation.

Another possible limiting factor is is the initial three-dimensional growth, likely originating from the low wettability of $SrMoO_3$ on typical insulating substrates. As shown in Fig 7.12, the initial two-dimensional streaky RHEED pattern of the substrate [Fig 7.12(a) and (d)] quickly disappeared, and three-dimensional patterns appeared, both during growth in vacuum [Fig 7.12(b)] and in argon [Fig 7.12(e)]. After growth of relatively thick films, the RHEED pattern did not change in vacuum [Fig 7.12(c)], but became streaky again in argon [Fig 7.12(c)], consistent with the AFM results. The initial three-dimensional growth has also been observed by Radetinac *et al.* [120]. This can be resolved if we find an appropriate buffer material which has a good wettability both with the substrate and the film [210].

7.5 Conclusion

In summary, we improved the quality of $SrMoO_3$ thin films by optimizing PLD growth conditions. We demonstrated that the plume–ambient gas interaction is a key growth parameter to

simultaneously realize a high conductivity and a flat surface. High-quality $SrMoO_3$ thin films were successfully grown which has the highest conductivity among the films reported, which enabled the Hall effect measurement to evaluate the carrier density and mobility. While the low temperature mobility was low at this point, much higher mobility could be achieved with further improvements.

The high-quality films grown in this study should enable a more detailed study on this material, possibly by transport measurements under high magnetic fields. Also, the flat surface indicates that more complex structures than a single-layer thin film can now be grown, which will shed light on possible device applications using this high conductivity metal. As growth of many other perovskite oxides requires more oxidizing conditions, the stability of the $SrMoO_3$ films under such oxidizing conditions is an important issue to be further investigated. It has been demonstrated that epitaxial stabilization and capping layers can prevent excess oxidation of $EuTiO_3$ thin films [211], which also requires extremely strong reducing conditions for growth. Similar approaches may be available for stabilizing $SrMoO_3$.

Chapter 8

Summary and Perspectives

Overall summary

Triggered by the discovery of high-temperature superconductivity in cuprates [2], the field of oxide electronics has been rapidly growing. In this Thesis, in order to construct a more solid basis for the further development of this field, we aimed to demonstrate the importance of detailed control of PLD growth parameters for complex oxide heterostructures. Here, we summarize how this goal was achieved.

In the case of PLD, one of the most common oxide thin film fabrication techniques, it is well known that the film properties can vary greatly with growth conditions, due to growth induced defects, especially off-stoichiometry. Therefore, in Chap. 4, we investigated the effect of the ablating laser parameters on the $LaAlO_3$ cation stoichiometry, structure, and the interfacial electronic properties of the $LaAlO_3/SrTiO_3$ heterointerface, one of the most extensively studied systems in this field. The La/Al ratio could be varied over a wide range, and was found to have a strong effect on the interface conductivity. In particular, the carrier density was modulated over more than two orders of magnitude, following one functional control parameter – the $LaAlO_3$ lattice constant. These results could be understood to arise from the variations in the electrostatic boundary conditions, and their resolution, with $LaAlO_3$ stoichiometry.

The wide growth-tunability of the properties of this system motivated further growth optimization to realize low-density high-mobility electron systems, as presented in Chap. 5. The low-temperature mobility was greatly enhanced by the growth optimization, which enabled the observation of quantum oscillations under high magnetic fields. Comparison between the Shubnikov–de Haas oscillations and the Hall effect provided important insights into the complex electronic structure at the interface. In particular, the pulsed magnet measurement suggested the presence of an effective spin degeneracy, and at the lowest density regime, nearly all of the mobile electrons might be detected via the quantum oscillations.

The growth-tunability was also applied to the study on ferromagnetism in this system, as presented in Chap. 6. The correlation between magnetic and (super)conducting properties indicated that interface reconstruction driven by the polar discontinuity is necessary for the formation of magnetism, but the existence of mobile carriers is not a prerequisite. The element-specific spectroscopic techniques identified the host of the magnetism as the additional electron in the

Ti^{3+} state with the d_{xy} orbital character. These results indicated that the localized carriers contribute to magnetism, decoupled from the itinerant electrons.

Finally, as presented in Chap. 7, we aimed to grow high-quality $SrMoO_3$ thin films, a contrasting system to the $LaAlO_3/SrTiO_3$ heterostructure. By systematically tuning the PLD growth parameters, the conductivity and the surface flatness were simultaneously optimized, with the former significantly improved from the previous reports. The interaction of ablated species with argon (inert gas) was found to be the key growth parameter to improve the film quality. The high-quality film enabled Hall effect measurements, which quantified the electron density and mobility of this high conductivity metal in thin film form.

In summary, the sensitivity of growth control by PLD has been found to be crucial for studies of complex oxide heterostructures. In PLD, thermodynamic conditions (T_g and P_{O_2}) are not the only growth parameters, as often reported. Fine details of the ablating laser and ambient gas environment also greatly modify the film or interface properties, sometimes overwhelming the effect of the thermodynamic conditions. Although the importance has been demonstrated for two specific systems in this Thesis, we note that this idea should be applicable in the growth control to study the novel physical properties in many other complex oxide heterostructures in general.

Future perspectives

In closing of this Thesis, we note several prospects of possible future research based on this study. The wide growth-tunability of the properties of the $LaAlO_3/SrTiO_3$ heterointerface indicates that we can study novel two-dimensional electron physics using this system. In particular, as mentioned in the conclusion of Chap. 5, the low-density high-mobility sample fabricated in this study will in principle enable the observation of the quantum Hall effect. The low density superconductivity in $SrTiO_3$ [47, 48] suggests that the quantum Hall effect in this system can be unconventional, as the interplay between these two states is theoretically expected to show novel emergent phenomena [170]. To reach the extreme quantum limit, where only the lowest Landau level is occupied, the sheet carrier density $n_{2D} \sim 3 \times 10^{12}$ cm^{-2} may be still high.[*1] Measurements under very high magnetic fields is thus likely necessary; the 100 T pulsed magnet in the National High Magnetic Field Laboratory [212] can be helpful for this possible future research.

For $SrMoO_3$, as mentioned in the conclusion of Chap. 7, the flat surface achieved in this work indicates that more complex structures than a single-layer thin film can now be grown, which will shed light on possible device applications using this high conductivity metal. An obvious, but fundamental and important example of such structures is probably the $SrTiO_3/SrMoO_3$ Schottky junction, as the junctions between $SrTiO_3$ and the other conducting perovskite oxides have been extensively studied, providing important insights on the materials properties [213–215]. By measuring the properties of the $SrTiO_3/SrMoO_3$ Schottky junction, we will be able to characterize this high conductivity metal in more detail; most notably, the work function

[*1] Each Landau level can accommodate $2.4 \times 10^{10} \times B\,[\text{in T}] \times N_{\text{deg}}$ cm^{-2} electrons.

of $SrMoO_3$ may be obtained. Since $SrTiO_3$ will be highly reduced under the strong reducing conditions required for growth of $SrMoO_3$, post-annealing treatment is likely necessary. Examining possible stabilization of $SrMoO_3$ thin films by epitaxy and capping [211] is thus an important next step for further studying this potentially interesting material.

We hope the results obtained in this work will play an important role as a basis for the study of complex oxide heterostructures.

Appendix A

Data Treatment for Hall Effect and Magnetoresistance Measurements

A.1 DC magnet

As explained in Sec. 3.5, a standard Hall bar geometry was used throughout this thesis. However, there was a practical problem that R_{xx} and R_{xy} cannot be measured independently due to the inevitable misalignment of the electrodes, as schematically shown in Fig. A.1. Therefore, in order to extract R_{xx} and R_{xy} independently, the raw data of the Hall effect and the magnetoresistance measurements were treated as follows (unless otherwise indicated).

Assuming $R_{xx}(B)$ is an even function and $R_{xy}(B)$ is an odd function,[*1] we can extract $R_{xx}(B)$ ($R_{xy}(B)$) by symmetrizing (antisymmetrizing) the raw data:

$$R_{xx}(B) = \frac{R_{xx}^{(\mathrm{raw})}(B) + R_{xx}^{(\mathrm{raw})}(-B)}{2}, \tag{A.1}$$

$$R_{xy}(B) = \frac{R_{xy}^{(\mathrm{raw})}(B) - R_{xy}^{(\mathrm{raw})}(-B)}{2}. \tag{A.2}$$

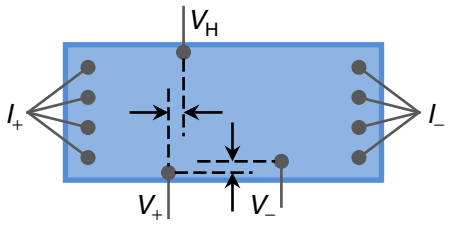

Fig. A.1 Schematic illustration of the practical geometry of electrodes.

[*1] This assumption might not be fully valid for the $LaAlO_3/SrTiO_3$ interface, which have been found to be ferromagnetic at low temperature (see Chap. 6), which can in principle induce hysteresis. It has always been confirmed that the raw data have no significant hysteresis above noise, indicating that the out-of-plane direction is the hard axis and/or the small magnetic moments have only a negligible effect on the transport properties.

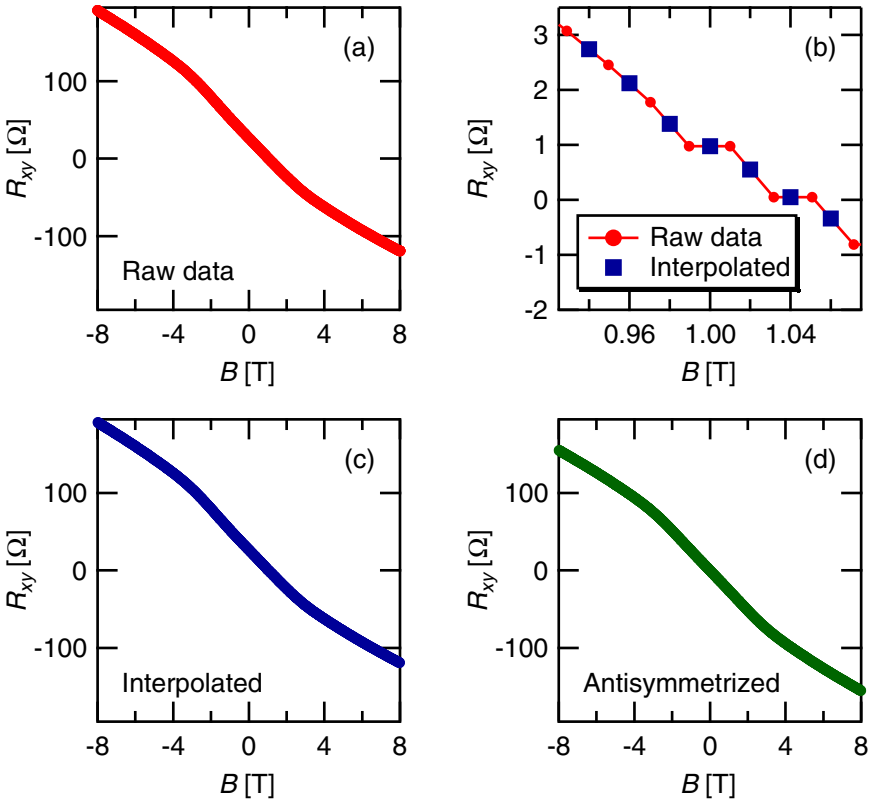

Fig. A.2 (a) A set of raw R_{xy} data. (b) The scheme of linear interpolation to derive a set of equally-spaced data. (c) Interpolated R_{xy} data. (d) Antisymmetrized R_{xy} data derived using Eq. A.2.

In this calculation, however, we have the second practical problem that the raw data are not perfectly spaced in magnetic field. For example, the raw data available are often like $R_{xx}^{(\mathrm{raw})}(B = 7.98\ \mathrm{T})$ and $R_{xx}^{(\mathrm{raw})}(B = -8.01\ \mathrm{T})$, with which we cannot derive $R_{xx}(B = 8.00\ \mathrm{T})$. In order to solve this problem, a set of equally-spaced data was derived by linear-interpolation of the raw data, as shown in Fig. A.2(b). It was always confirmed that the interpolated data [Fig. A.2(c)] have no significant difference from the raw data [Fig. A.2(a)], and then the interpolated data $R_{xx}^{(\mathrm{int})}(B)$ and $R_{xy}^{(\mathrm{int})}(B)$ were substituted in Eqs. A.1 and A.2 instead of the raw data to extract $R_{xx}(B)$ and $R_{xy}(B)$ [Fig. A.2(d)].

The sheet carrier density n_s and the Hall mobility μ_H are derived by

$$n_\mathrm{s} = -\frac{1}{eR_\mathrm{H}}, \tag{A.3}$$

$$\mu_\mathrm{H} = \frac{1}{en_\mathrm{s}\rho_\mathrm{s}} = -\frac{R_\mathrm{H}}{\rho_\mathrm{s}}, \tag{A.4}$$

where

$$R_\mathrm{H} \equiv \frac{R_{xy}(B)}{B} \tag{A.5}$$

is the Hall coefficient and ρ_s is the sheet resistance. As seen in Fig. A.2(d), the Hall resistance $R_{xy}(B)$ is sometimes nonlinear with the magnetic field in the systems investigated, and therefore

the Hall coefficient is a function of magnetic field. Throughout this thesis, R_{H} was calculated by linear-fitting of the antisymmetrized data between 0–1 T.

A.2 Pulsed magnet

Compared to the measurement under the DC magnet in the PPMS, the pulsed magnet has a few additional problems. The first is the electromagnetic induction. Due to the very large $\mathrm{d}B/\mathrm{d}t$ in the pulsed magnet, a nontrivial voltage is induced even in a tiny loop of electrodes.

This problem can in principle be avoided by selectively measuring the sample signal using an AC lock-in technique. However, the AC measurement is practically impossible for the samples in this study. Since the typical pulse width of the magnet is $\sim$ 10 msec (see Fig. 5.8 and Ref. [167]), the practical lower limit of the frequency for the AC measurement is $\approx$ 30 kHz. Due to the low density, although with a high mobility, of the samples in this study, this frequency is already too high to correctly measure the sample properties.[*2]

Therefore, in this study, a DC bias was applied to the sample, and the contributions of the electromagnetic induction and the Hall effect (due to the inevitable misalignment of the electrodes, as mentioned above) were subtracted by treating the raw data as follows. The raw longitudinal voltage can be described as

$$
\begin{aligned}
V_{xx}^{(\mathrm{raw})}(+B,\,+I) &= +IR_{xx} + I\delta R_{xy} + V_{\mathrm{ind}},\\
V_{xx}^{(\mathrm{raw})}(+B,\,-I) &= -IR_{xx} - I\delta R_{xy} + V_{\mathrm{ind}},\\
V_{xx}^{(\mathrm{raw})}(-B,\,+I) &= +IR_{xx} - I\delta R_{xy} - V_{\mathrm{ind}},\\
V_{xx}^{(\mathrm{raw})}(-B,\,-I) &= -IR_{xx} + I\delta R_{xy} - V_{\mathrm{ind}},
\end{aligned}
$$

where I is the bias current, δR_{xy} denotes the finite contribution of the Hall effect, V_{ind} is the electromagnetically induced voltage, which changes the sign as the polarity of the pulse changes. Therefore, R_{xx} can be extracted by

$$
R_{xx} = \frac{V_{xx}^{(\mathrm{raw})}(+B,\,+I) - V_{xx}^{(\mathrm{raw})}(+B,\,-I) + V_{xx}^{(\mathrm{raw})}(-B,\,+I) - V_{xx}^{(\mathrm{raw})}(-B,\,-I)}{4I}. \tag{A.6}
$$

Similarly, R_{xy} can be extracted by

$$
R_{xy} = \frac{V_{xy}^{(\mathrm{raw})}(+B,\,+I) - V_{xy}^{(\mathrm{raw})}(+B,\,-I) - V_{xy}^{(\mathrm{raw})}(-B,\,+I) + V_{xy}^{(\mathrm{raw})}(-B,\,-I)}{4I}. \tag{A.7}
$$

As before, equally-spaced data sets derived by linear-interpolation were used for these calculations.

Figure A.3(a) shows an example of four sets of interpolated[*3] V_{xx} data with different pulse polarities and bias current directions. The loops correspond to V_{ind} in each shot. Substituting

[*2] When a 30 kHz AC bias was applied, the sample response showed a phase shift. M. Kim, private communication (2012).

[*3] For clarity; the number of the raw data points is too large to be displayed here.

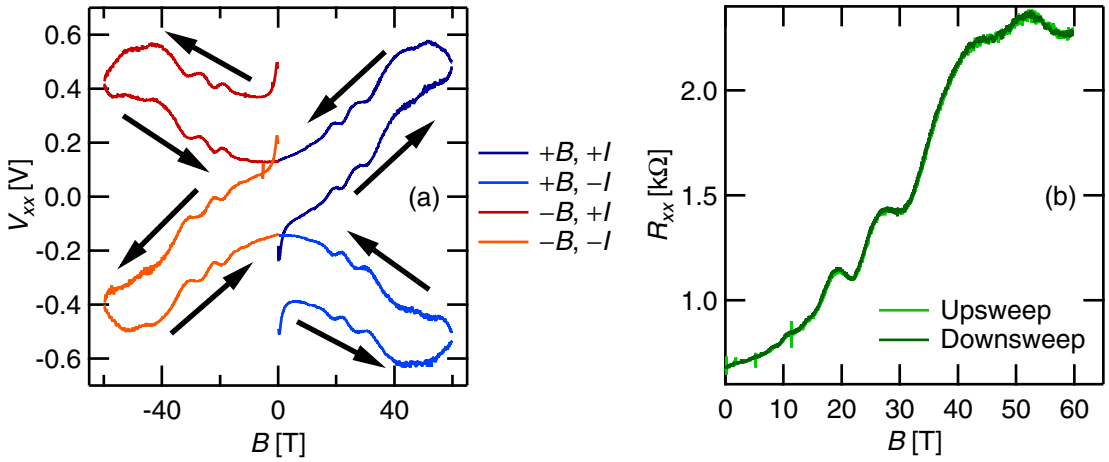

Fig. A.3 (a) Sets of interpolated V_{xx} data. (b) Symmetrized R_{xx} data derived using Eq. A.6. Bias current $I = 10\ \mu\text{A}$.

these data sets in Eq. A.6, the symmetrized R_{xx} data were extracted, as shown in Fig. A.3(b). The small, although almost within the noise level, difference between the upsweep and the downsweep is because of the finite shot-to-shot variation of V_{ind}. As $|\mathrm{d}B/\mathrm{d}t|$ is smaller during the downsweep, the effect of V_{ind} is also smaller, and thus the data sets obtained from the downsweep are always used for further analysis.

References

[1] M. Imada, A. Fujimori, and Y. Tokura, Metal-insulator transitions, *Rev. Mod. Phys.* **70**, 1039 (1998).

[2] J. G. Bednorz and K. A. Müller, Possible high T_c superconductivity in the Ba–La–Cu–O system, *Z. Phys. B* **64**, 189 (1986).

[3] A. P. Malozemoff, J. Mannhart, and D. Scalapino, High-temperature cuprate superconductors get to work, *Phys. Today* **58**, 41 (2005).

[4] A. Urushibara, Y. Moritomo, T. Arima, A. Asamitsu, G. Kido, and Y. Tokura, Insulator-metal transition and giant magnetoresistance in $La_{1-x}Sr_xMnO_3$, *Phys. Rev. B* **51**, 14103 (1995).

[5] Y. Kato, Y. Kaneko, H. Tanaka, and Y. Shimada, Nonvolatile memory using epitaxially grown composite-oxide-film technology, *Jpn. J. Appl. Phys.* **47**, 2719 (2008).

[6] H. Tanaka, Y. Kaneko, and Y. Kato, A ferroelectric gate field effect transistor with a ZnO/Pb(Zr,Ti)O_3 heterostructure formed on a silicon substrate, *Jpn. J. Appl. Phys.* **47**, 7527 (2008).

[7] S. Jin, T. H. Tiefel, M. McCormack, R. A. Fastnacht, R. Ramesh, and L. H. Chen, Thousandfold change in resistivity in magnetoresistive La-Ca-Mn-O films, *Science* **264**, 413 (1994).

[8] S. Jin, T. H. Tiefel, M. McCormack, H. M. O'Bryan, L. H. Chen, R. Ramesh, and D. Schurig, Thickness dependence of magnetoresistance in La–Ca–Mn–O epitaxial films, *Appl. Phys. Lett.* **67**, 557 (1995).

[9] K. Ueda, H. Tabata, and T. Kawai, Ferromagnetism in $LaFeO_3$-$LaCrO_3$ superlattices, *Science* **280**, 1064 (1998).

[10] A. Ohtomo and H. Y. Hwang, A high-mobility electron gas at the $LaAlO_3$/$SrTiO_3$ heterointerface, *Nature* **427**, 423 (2004), corrigendum: **441**, 120 (2006).

[11] D. G. Schlom, L.-Q. Chen, C.-B. Eom, K. M. Rabe, S. K. Streiffer, and J.-M. Triscone, Strain tuning of ferroelectric thin films, *Annu. Rev. Mater. Res.* **37**, 589 (2007).

[12] D. Dijkkamp, T. Venkatesan, X. D. Wu, S. A. Shaheen, N. Jisrawi, Y. H. Min-Lee, W. L. McLean, and M. Croft, Preparation of Y-Ba-Cu oxide superconductor thin films using pulsed laser evaporation from high T_c bulk material, *Appl. Phys. Lett.* **51**, 619 (1987).

[13] A. Tsukazaki, A. Ohtomo, and M. Kawasaki, High-mobility electronic transport in ZnO thin films, *Appl. Phys. Lett.* **88**, 152106 (2006).

[14] A. Tsukazaki, A. Ohtomo, T. Kita, Y. Ohno, H. Ohno, and M. Kawasaki, Quantum Hall effect in polar oxide heterostructures, *Science* **315**, 1388 (2007).

[15] B. Dam, J. H. Rector, J. Johansson, J. Huijbregtse, and D. G. De Groot, Mechanism of incongruent ablation of $SrTiO_3$, *J. Appl. Phys.* **83**, 3386 (1998).

[16] J. M. Huijbregtse, B. Dam, J. H. Rector, and R. Griessen, High-quality off-stoichiometric $YBa_2Cu_3O_{7-\delta}$ films produced by diffusion-assisted preferential laser ablation, *J. Appl. Phys.* **86**, 6528 (1999).

[17] T. Ohnishi, K. Shibuya, T. Yamamoto, and M. Lippmaa, Defects and transport in complex oxide thin films, *J. Appl. Phys.* **103**, 103703 (2008).

[18] J. H. Song, T. Susaki, and H. Y. Hwang, Enhanced thermodynamic stability of epitaxial oxide thin films, *Adv. Mater.* **20**, 2528 (2008).

[19] Y. Matsumoto, M. Murakami, T. Shono, T. Hasegawa, T. Fukumura, M. Kawasaki, P. Ahmet, T. Chikyow, S. Koshihara, and H. Koinuma, Room-temperature ferromagnetism in transparent transition metal-doped titanium dioxide, *Science* **291**, 854 (2001).

[20] T. C. Kaspar, S. M. Heald, C. M. Wang, J. D. Bryan, T. Droubay, V. Shutthanandan, S. Thevuthasan, D. E. McCready, A. J. Kellock, D. R. Gamelin, and S. A. Chambers, Negligible magnetism in excellent structural quality $Cr_xTi_{1-x}O_2$ anatase: Contrast with high-T_C ferromagnetism in structurally defective $Cr_xTi_{1-x}O_2$, *Phys. Rev. Lett.* **95**, 217203 (2005).

[21] I. Nagai, N. Shirakawa, S. Ikeda, R. Iwasaki, H. Nishimura, and M. Kosaka, Highest conductivity oxide $SrMoO_3$ grown by a floating-zone method under ultralow oxygen partial pressure, *Appl. Phys. Lett.* **87**, 024105 (2005).

[22] K. A. Müller, W. Berlinger, and F. Waldner, Characteristic structural phase transition in perovskite-type compounds, *Phys. Rev. Lett.* **21**, 814 (1968).

[23] G. Shirane and Y. Yamada, Lattice-dynamical study of the 110°K phase transition in $SrTiO_3$, *Phys. Rev.* **177**, 858 (1969).

[24] J. A. Noland, Optical absorption of single-crystal strontium titanate, *Phys. Rev.* **94**, 724 (1954).

[25] M. Capizzi and A. Frova, Optical gap of strontium titanate (deviation from Urbach tail behavior), *Phys. Rev. Lett.* **25**, 1298 (1970).

[26] A. H. Kahn and A. J. Leyendecker, Electronic energy bands in strontium titanate, *Phys. Rev.* **135**, A1321 (1964).

[27] L. F. Mattheiss, Energy bands for $KNiF_3$, $SrTiO_3$, $KMoO_3$, and $KTaO_3$, *Phys. Rev. B* **6**, 4718 (1972).

[28] L. F. Mattheiss, Effect of the 100°K phase transition on the $SrTiO_3$ conduction bands, *Phys. Rev. B* **6**, 4740 (1972).

[29] H. P. R. Frederikse, W. R. Thurber, and W. R. Hosler, Electronic transport in strontium titanate, *Phys. Rev.* **134**, A442 (1964).

[30] O. N. Tufte and P. W. Chapman, Electron mobility in semiconducting strontium titanate, *Phys. Rev.* **155**, 796 (1967).

[31] C. Lee, J. Yahia, and J. L. Brebner, Electronic conduction in slightly reduced strontium titanate at low temperatures, *Phys. Rev. B* **3**, 2525 (1971).

[32] T. Sakudo and H. Unoki, Dielectric properties of $SrTiO_3$ at low temperatures, *Phys. Rev. Lett.* **26**, 851 (1971).

[33] K. A. Müller and H. Burkard, $SrTiO_3$: An intrinsic quantum paraelectric below 4 K, *Phys. Rev. B* **19**, 3593 (1979).

[34] H.-M. Christen, J. Mannhart, E. J. Williams, and C. Gerber, Dielectric properties of sputtered $SrTiO_3$ films, *Phys. Rev. B* **49**, 12095 (1994).

[35] T. Yamamoto, S. Suzuki, K. Kawaguchi, and K. Takahashi, Temperature dependence of the ideality factor of $Ba_{1-x}K_xBiO_3$/Nb-doped $SrTiO_3$ all-oxide-type schottky junctions, *Jpn. J. Appl. Phys.* **37**, 4737 (1998).

[36] J. G. Bednorz and K. A. Müller, $Sr_{1-x}Ca_xTiO_3$: An *XY* quantum ferroelectric with transition to randomness, *Phys. Rev. Lett.* **52**, 2289 (1984).

[37] M. Itoh, R. Wang, Y. Inaguma, T. Yamaguchi, Y.-J. Shan, and T. Nakamura, Ferroelectricity induced by oxygen isotope exchange in strontium titanate perovskite, *Phys. Rev. Lett.* **82**, 3540 (1999).

[38] H. Uwe and T. Sakudo, Stress-induced ferroelectricity and soft phonon modes in $SrTiO_3$, *Phys. Rev. B* **13**, 271 (1976).

[39] J. H. Haeni, P. Irvin, W. Chang, R. Uecker, P. Reiche, Y. L. Li, S. Choudhury, W. Tian, M. E. Hawley, B. Craigo, A. K. Tagantsev, X. Q. Pan, S. K. Streiffer, L. Q. Chen, S. W. Kirchoefer, J. Levy, and D. G. Schlom, Room-temperature ferroelectricity in strained $SrTiO_3$, *Nature* **430**, 758 (2004).

[40] S. Thiel, G. Hammerl, A. Schmehl, C. W. Schneider, and J. Mannhart, Tunable quasi-two-dimensional electron gases in oxide heterostructures, *Science* **313**, 1942 (2006).

[41] A. D. Caviglia, S. Gariglio, N. Reyren, D. Jaccard, T. Schneider, M. Gabay, S. Thiel, G. Hammerl, J. Mannhart, and J.-M. Triscone, Electric field control of the $LaAlO_3$/$SrTiO_3$ interface ground state, *Nature* **456**, 624 (2008).

[42] C. Bell, S. Harashima, Y. Kozuka, M. Kim, B. G. Kim, Y. Hikita, and H. Y. Hwang, Dominant mobility modulation by the electric field effect at the $LaAlO_3$/$SrTiO_3$ interface, *Phys. Rev. Lett.* **103**, 226802 (2009).

[43] J. H. Ngai, Y. Segal, D. Su, Y. Zhu, F. J. Walker, S. Ismail-Beigi, K. Le Hur, and C. H. Ahn, Electric field tuned crossover from classical to weakly localized quantum transport in electron doped $SrTiO_3$, *Phys. Rev. B* **81**, 241307 (2010).

[44] J. F. Schooley, W. R. Hosler, and M. L. Cohen, Superconductivity in semiconducting $SrTiO_3$, *Phys. Rev. Lett.* **12**, 474 (1964).

[45] J. F. Schooley, W. R. Hosler, E. Ambler, J. H. Becker, M. L. Cohen, and C. S. Koonce, Dependence of the superconducting transition temperature on carrier concentration in semiconducting $SrTiO_3$, *Phys. Rev. Lett.* **14**, 305 (1965).

[46] E. Ambler, J. H. Colwell, W. R. Hosler, and J. F. Schooley, Magnetization and critical fields of superconducting $SrTiO_3$, *Phys. Rev.* **148**, 280 (1966).

[47] C. S. Koonce, M. L. Cohen, J. F. Schooley, W. R. Hosler, and E. R. Pfeiffer, Superconducting transition temperatures of semiconducting $SrTiO_3$, *Phys. Rev.* **163**, 380 (1967).

[48] X. Lin, Z. Zhu, B. Fauqué, and K. Behnia, Fermi surface of the most dilute superconductor, *Phys. Rev. X* **3**, 021002 (2013).

[49] E. A. Ekimov, V. A. Sidorov, E. D. Bauer, N. N. Mel'nik, N. J. Curro, J. D. Thompson, and S. M. Stishov, Superconductivity in diamond, *Nature* **428**, 542 (2004).

[50] E. Bustarret, J. Kačmarčik, C. Marcenat, E. Gheeraert, C. Cytermann, J. Marcus, and T. Klein, Dependence of the superconducting transition temperature on the doping level in single-crystalline diamond films, *Phys. Rev. Lett.* **93**, 237005 (2004).

[51] E. Bustarret, C. Marcenat, P. Achatz, J. Kačmarčik, F. Lévy, A. Huxley, L. Ortéga, E. Bourgeois, X. Blase, D. Débarre, and J. Boulmer, Superconductivity in doped cubic silicon, *Nature* **444**, 465 (2006).

[52] Z.-A. Ren, J. Kato, T. Muranaka, J. Akimitsu, M. Kriener, and Y. Maeno, Superconductivity in boron-doped SiC, *J. Phys. Soc. Jpn.* **76**, 103710 (2007).

[53] T. Herrmannsdörfer, V. Heera, O. Ignatchik, M. Uhlarz, A. Mücklich, M. Posselt, H. Reuther, B. Schmidt, K.-H. Heinig, W. Skorupa, M. Voelskow, C. Wündisch, R. Skrotzki, M. Helm, and J. Wosnitza, Superconducting state in a gallium-doped germanium layer at low temperatures, *Phys. Rev. Lett.* **102**, 217003 (2009).

[54] N. P. Butch, P. Syers, K. Kirshenbaum, A. P. Hope, and J. Paglione, Superconductivity in the topological semimetal YPtBi, *Phys. Rev. B* **84**, 220504 (2011).

[55] T. V. Bay, T. Naka, Y. K. Huang, and A. de Visser, Superconductivity in noncentrosymmetric YPtBi under pressure, *Phys. Rev. B* **86**, 064515 (2012).

[56] F. F. Tafti, T. Fujii, A. Juneau-Fecteau, S. René de Cotret, N. Doiron-Leyraud, A. Asamitsu, and L. Taillefer, Superconductivity in the noncentrosymmetric half-Heusler compound LuPtBi: A candidate for topological superconductivity, *Phys. Rev. B* **87**, 184504 (2013).

[57] H. P. R. Frederikse and W. R. Hosler, Hall mobility in $SrTiO_3$, *Phys. Rev.* **161**, 822 (1967).

[58] G. Perluzzo and J. Destry, The characterization of pure and niobium-doped crystals of strontium titanate using Hall, electrical conductivity, and optical absorption data, *Can. J. Phys.* **56**, 453 (1978).

[59] H. Suzuki, H. Bando, Y. Ootuka, I. H. Inoue, T. Yamamoto, K. Takahashi, and Y. Nishihara, Superconductivity in single-crystalline $Sr_{1-x}La_xTiO_3$, *J. Phys. Soc. Jpn.* **65**, 1529 (1996).

[60] S. Geller and V. B. Bala, Crystallographic studies of perovskite-like compounds. II. Rare earth alluminates, *Acta Cryst.* **9**, 1019 (1956).

[61] S. A. Hayward, F. D. Morrison, S. A. T. Redfern, E. K. H. Salje, J. F. Scott, K. S. Knight, S. Tarantino, A. M. Glazer, V. Shuvaeva, P. Daniel, M. Zhang, and M. A. Carpenter, Transformation processes in $LaAlO_3$: Neutron diffraction, dielectric, thermal, optical, and Raman studies, *Phys. Rev. B* **72**, 054110 (2005).

[62] G. W. Berkstresser, A. J. Valentino, and C. D. Brandle, Growth of single crystals of lanthanum aluminate, *J. Cryst. Growth* **109**, 457 (1991).

[63] S.-G. Lim, S. Kriventsov, T. N. Jackson, J. H. Haeni, D. G. Schlom, A. M. Balbashov, R. Uecker, P. Reiche, J. L. Freeouf, and G. Lucovsky, Dielectric functions and optical bandgaps of high-K dielectrics for metal-oxide-semiconductor field-effect transistors by far ultraviolet spectroscopic ellipsometry, *J. Appl. Phys.* **91**, 4500 (2002).

[64] T. L. Nguyen, M. Dokiya, S. Wang, H. Tagawa, and T. Hashimoto, The effect of oxygen vacancy on the oxide ion mobility in $LaAlO_3$-based oxides, *Solid State Ionics* **130**, 229

(2000).

[65] J. Krupka, R. G. Geyer, M. Kuhn, and J. H. Hinken, Dielectric properties of single crystals of Al_2O_3, $LaAlO_3$, $NdGaO_3$, $SrTiO_3$, and MgO at cryogenic temperatures, *IEEE Trans. Microwave Theory Tech.* **42**, 1886 (1994).

[66] R. Jany, M. Breitschaft, G. Hammerl, A. Horsche, C. Richter, S. Paetel, J. Mannhart, N. Stucki, N. Reyren, S. Gariglio, P. Zubko, A. D. Caviglia, and J.-M. Triscone, Diodes with breakdown voltages enhanced by the metal-insulator transition of $LaAlO_3$–$SrTiO_3$ interfaces, *Appl. Phys. Lett.* **96**, 183504 (2010).

[67] B. Förg, C. Richter, and J. Mannhart, Field-effect devices utilizing $LaAlO_3$-$SrTiO_3$ interfaces, *Appl. Phys. Lett.* **100**, 053506 (2012).

[68] M. Hosoda, Y. Hikita, H. Y. Hwang, and C. Bell, Transistor operation and mobility enhancement in top-gated $LaAlO_3$/$SrTiO_3$ heterostructures, *Appl. Phys. Lett.* **103**, 103507 (2013).

[69] N. Reyren, S. Thiel, A. D. Caviglia, L. Fitting Kourkoutis, G. Hammerl, C. Richter, C. W. Schneider, T. Kopp, A.-S. Rüetschi, D. Jaccard, M. Gabay, D. A. Muller, J.-M. Triscone, and J. Mannhart, Superconducting interfaces between insulating oxides, *Science* **317**, 1196 (2007).

[70] A. D. Caviglia, S. Gariglio, C. Cancellieri, B. Sacépé, A. Fête, N. Reyren, M. Gabay, A. F. Morpurgo, and J.-M. Triscone, Two-dimensional quantum oscillations of the conductance at $LaAlO_3$/$SrTiO_3$ interfaces, *Phys. Rev. Lett.* **105**, 236802 (2010).

[71] A. Brinkman, M. Huijben, M. van Zalk, J. Huijben, U. Zeitler, J. C. Maan, W. G. van der Wiel, G. Rijnders, D. H. A. Blank, and H. Hilgenkamp, Magnetic effects at the interface between non-magnetic oxides, *Nature Mater.* **6**, 493 (2007).

[72] J. Nishimura, A. Ohtomo, A. Ohkubo, Y. Murakami, and M. Kawasaki, Controlled carrier generation at a polarity-discontinued perovskite heterointerface, *Jpn. J. Appl. Phys.* **43**, L1032 (2004).

[73] N. Nakagawa, H. Y. Hwang, and D. A. Muller, Why some interfaces cannot be sharp, *Nature Mater.* **5**, 204 (2006).

[74] M. Kawasaki, K. Takahashi, T. Maeda, R. Tsuchiya, M. Shinohara, O. Ishiyama, T. Yonezawa, M. Yoshimoto, and H. Koinuma, Atomic control of the $SrTiO_3$ crystal surface, *Science* **266**, 1540 (1994).

[75] G. Koster, B. L. Kropman, G. J. H. M. Rijnders, D. H. A. Blank, and H. Rogalla, Quasi-ideal strontium titanate crystal surfaces through formation of strontium hydroxide, *Appl. Phys. Lett.* **73**, 2920 (1998).

[76] G. A. Baraff, J. A. Appelbaum, and D. R. Hamann, Self-consistent calculation of the electronic structure at an abrupt GaAs-Ge interface, *Phys. Rev. Lett.* **38**, 237 (1977).

[77] W. A. Harrison, E. A. Kraut, J. R. Waldrop, and R. W. Grant, Polar heterojunction interfaces, *Phys. Rev. B* **18**, 4402 (1978).

[78] A. Kalabukhov, R. Gunnarsson, J. Börjesson, E. Olsson, T. Claeson, and D. Winkler, Effect of oxygen vacancies in the $SrTiO_3$ substrate on the electrical properties of the $LaAlO_3$/$SrTiO_3$ interface, *Phys. Rev. B* **75**, 121404 (2007).

[79] W. Siemons, G. Koster, H. Yamamoto, W. A. Harrison, G. Lucovsky, T. H. Geballe,

D. H. A. Blank, and M. R. Beasley, Origin of charge density at $LaAlO_3$ on $SrTiO_3$ heterointerfaces: Possibility of intrinsic doping, *Phys. Rev. Lett.* **98**, 196802 (2007).

[80] G. Herranz, M. Basletić, M. Bibes, C. Carrétéro, E. Tafra, E. Jacquet, K. Bouzehouane, C. Deranlot, A. Hamzić, J.-M. Broto, A. Barthélémy, and A. Fert, High mobility in $LaAlO_3/SrTiO_3$ heterostructures: Origin, dimensionality, and perspectives, *Phys. Rev. Lett.* **98**, 216803 (2007).

[81] P. R. Willmott, S. A. Pauli, R. Herger, C. M. Schlepütz, D. Martoccia, B. D. Patterson, B. Delley, R. Clarke, D. Kumah, C. Cionca, and Y. Yacoby, Structural basis for the conducting interface between $LaAlO_3$ and $SrTiO_3$, *Phys. Rev. Lett.* **99**, 155502 (2007).

[82] A. S. Kalabukhov, Y. A. Boikov, I. T. Serenkov, V. I. Sakharov, V. N. Popok, R. Gunnarsson, J. Börjesson, N. Ljustina, E. Olsson, D. Winkler, and T. Claeson, Cationic disorder and phase segregation in $LaAlO_3/SrTiO_3$ heterointerfaces evidenced by medium-energy ion spectroscopy, *Phys. Rev. Lett.* **103**, 146101 (2009).

[83] L. Qiao, T. C. Droubay, V. Shutthanandan, Z. Zhu, P. V. Sushko, and S. A. Chambers, Thermodynamic instability at the stoichiometric $LaAlO_3/SrTiO_3(001)$ interface, *J. Phys.: Condens. Matter* **22**, 312201 (2010).

[84] S. A. Chambers, M. H. Engelhard, V. Shutthanandan, Z. Zhu, T. C. Droubay, L. Qiao, P. V. Sushko, T. Feng, H. D. Lee, T. Gustafsson, E. Garfunkel, A. B. Shah, J.-M. Zuo, and Q. M. Ramasse, Instability, intermixing and electronic structure at the epitaxial $LaAlO_3/SrTiO_3(001)$ heterojunction, *Surf. Sci. Rep.* **65**, 317 (2010).

[85] M. L. Reinle-Schmitt, C. Cancellieri, D. Li, D. Fontaine, M. Medarde, E. Pomjakushina, C. W. Schneider, S. Gariglio, P. Ghosez, J.-M. Triscone, and P. R. Willmott, Tunable conductivity threshold at polar oxide interfaces, *Nature Commun.* **3**, 932 (2012).

[86] M. Basletic, J.-L. Maurice, C. Carrétéro, G. Herranz, O. Copie, M. Bibes, É. Jacquet, K. Bouzehouane, S. Fusil, and A. Barthélémy, Mapping the spatial distribution of charge carriers in $LaAlO_3/SrTiO_3$ heterostructures, *Nature Mater.* **7**, 621 (2008).

[87] C. Cancellieri, N. Reyren, S. Gariglio, A. D. Caviglia, A. Fete, and J.-M. Triscone, Influence of the growth conditions on the $LaAlO_3/SrTiO_3$ interface electronic properties, *Europhys. Lett.* **91**, 17004 (2010).

[88] G. Herranz, F. Sánchez, N. Dix, M. Scigaj, and J. Fontcuberta, High mobility conduction at (110) and (111) $LaAlO_3/SrTiO_3$ interfaces, *Sci. Rep.* **2**, 758 (2012).

[89] A. Annadi, Q. Zhang, X. Renshaw Wang, N. Tuzla, K. Gopinadhan, W. M. Lü, A. Roy Barman, Z. Q. Liu, A. Srivastava, S. Saha, Y. L. Zhao, S. W. Zeng, S. Dhar, E. Olsson, B. Gu, S. Yunoki, S. Maekawa, H. Hilgenkamp, T. Venkatesan, and Ariando, Anisotropic two-dimensional electron gas at the $LaAlO_3/SrTiO_3$ (110) interface, *Nature Commun.* **4**, 1838 (2013).

[90] Y. Mukunoki, N. Nakagawa, T. Susaki, and H. Y. Hwang, Atomically flat (110) $SrTiO_3$ and heteroepitaxy, *Appl. Phys. Lett.* **86**, 171908 (2005).

[91] Y. Hotta, T. Susaki, and H. Y. Hwang, Polar discontinuity doping of the $LaVO_3/SrTiO_3$ interface, *Phys. Rev. Lett.* **99**, 236805 (2007).

[92] J. Lee and A. A. Demkov, Charge origin and localization at the n-type $SrTiO_3/LaAlO_3$ interface, *Phys. Rev. B* **78**, 193104 (2008).

[93] Z. S. Popović, S. Satpathy, and R. M. Martin, Origin of the two-dimensional electron gas carrier density at the $LaAlO_3$ on $SrTiO_3$ interface, *Phys. Rev. Lett.* **101**, 256801 (2008).

[94] R. Pentcheva and W. E. Pickett, Avoiding the polarization catastrophe in $LaAlO_3$ overlayers on $SrTiO_3$(001) through polar distortion, *Phys. Rev. Lett.* **102**, 107602 (2009).

[95] Y. W. Xie, C. Bell, T. Yajima, Y. Hikita, and H. Y. Hwang, Charge writing at the $LaAlO_3$/$SrTiO_3$ surface, *Nano Lett.* **10**, 2588 (2010).

[96] G. Singh-Bhalla, C. Bell, J. Ravichandran, W. Siemons, Y. Hikita, S. Salahuddin, A. F. Hebard, H. Y. Hwang, and R. Ramesh, Built-in and induced polarization across $LaAlO_3$/$SrTiO_3$ heterojunctions, *Nature Phys.* **7**, 80 (2011).

[97] Y. Segal, J. H. Ngai, J. W. Reiner, F. J. Walker, and C. H. Ahn, X-ray photoemission studies of the metal-insulator transition in $LaAlO_3$/$SrTiO_3$ structures grown by molecular beam epitaxy, *Phys. Rev. B* **80**, 241107 (2009).

[98] Y. W. Xie, Y. Hikita, C. Bell, and H. Y. Hwang, Control of electronic conduction at an oxide heterointerface using surface polar adsorbates, *Nature Commun.* **2**, 494 (2011).

[99] G. Berner, M. Sing, H. Fujiwara, A. Yasui, Y. Saitoh, A. Yamasaki, Y. Nishitani, A. Sekiyama, N. Pavlenko, T. Kopp, C. Richter, J. Mannhart, S. Suga, and R. Claessen, Direct *k*-space mapping of the electronic structure in an oxide-oxide interface, *Phys. Rev. Lett.* **110**, 247601 (2013).

[100] T. Higuchi and H. Y. Hwang, General considerations of the electrostatic boundary conditions in oxide heterostructures, in *Multifunctional Oxide Heterostructures*, edited by E. Y. Tsymbal, E. R. A. Dagotto, C.-B. Eom, and R. Ramesh (Oxford University Press, 2012), chap. 7, pp. 183–213.

[101] J. B. Torrance, P. Lacorre, C. Asavaroengchai, and R. M. Metzger, Why are some oxides metallic, while most are insulating?, *Physica C* **182**, 351 (1991).

[102] E. Dagotto, Complexity in strongly correlated electronic systems, *Science* **309**, 257 (2005).

[103] A. Callaghan, C. W. Moeller, and R. Ward, Magnetic interactions in ternary ruthenium oxides, *Inorg. Chem.* **5**, 1572 (1966).

[104] P. B. Allen, H. Berger, O. Chauvet, L. Forro, T. Jarlborg, A. Junod, B. Revaz, and G. Santi, Transport properties, thermodynamic properties, and electronic structure of $SrRuO_3$, *Phys. Rev. B* **53**, 4393 (1996).

[105] M. Izumi, K. Nakazawa, Y. Bando, Y. Yoneda, and H. Terauchi, Magnetotransport of $SrRuO_3$ thin film on $SrTiO_3$(001), *J. Phys. Soc. Jpn.* **66**, 3893 (1997).

[106] G. Koster, L. Klein, W. Siemons, G. Rijnders, J. S. Dodge, C.-B. Eom, D. H. A. Blank, and M. R. Beasley, Structure, physical properties, and applications of $SrRuO_3$ thin films, *Rev. Mod. Phys.* **84**, 253 (2012).

[107] S. I.Ikeda and N. Shirakawa, Magnetic and transport properties of perovskite-related strontium molybdates, *Physica C* **341**, 785 (2000).

[108] S. Yamanaka, K. Kurosaki, T. Maekawa, T. Matsuda, S. Kobayashi, and M. Uno, Thermochemical and thermophysical properties of alkaline-earth perovskites, *J. Nucl. Mater.* **344**, 61 (2005).

[109] R. B. Macquart, B. J. Kennedy, and M. Avdeev, Neutron diffraction study of phase tran-

sitions in perovskite-type strontium molybdate $SrMoO_3$, *J. Solid State Chem.* **183**, 250 (2010).

[110] Z.-L. Zhu, J.-H. Gu, Y. Jia, and X. Hu, A comparative study of electronic structure and magnetic properties of $SrCrO_3$ and $SrMoO_3$, *Physica B* **407**, 1990 (2012).

[111] K. S. Takahashi, A. Sawa, Y. Ishii, H. Akoh, M. Kawasaki, and Y. Tokura, Inverse tunnel magnetoresistance in all-perovskite junctions of $La_{0.7}Sr_{0.3}MnO_3/SrTiO_3/SrRuO_3$, *Phys. Rev. B* **67**, 094413 (2003).

[112] M. N. Baibich, J. M. Broto, A. Fert, F. Nguyen Van Dau, F. Petroff, P. Etienne, G. Creuzet, A. Friederich, and J. Chazelas, Giant magnetoresistance of (001)Fe/(001)Cr magnetic superlattices, *Phys. Rev. Lett.* **61**, 2472 (1988).

[113] G. Binasch, P. Grünberg, F. Saurenbach, and W. Zinn, Enhanced magnetoresistance in layered magnetic structures with antiferromagnetic interlayer exchange, *Phys. Rev. B* **39**, 4828 (1989).

[114] A. Baikalov, Y. Q. Wang, B. Shen, B. Lorenz, S. Tsui, Y. Y. Sun, Y. Y. Xue, and C. W. Chu, Field-driven hysteretic and reversible resistive switch at the $Ag/Pr_{0.7}Ca_{0.3}MnO_3$ interface, *Appl. Phys. Lett.* **83**, 957 (2003).

[115] Y. Tokunaga, Y. Kaneko, J. P. He, T. Arima, A. Sawa, T. Fujii, M. Kawasaki, and Y. Tokura, Colossal electroresistance effect at metal electrode/$La_{1-x}Sr_{1+x}MnO_4$ interfaces, *Appl. Phys. Lett.* **88**, 223507 (2006).

[116] T. Susaki, Y. Kozuka, Y. Tateyama, and H. Y. Hwang, Temperature-dependent polarity reversal in Au/Nb:$SrTiO_3$ Schottky junctions, *Phys. Rev. B* **76**, 155110 (2007).

[117] K. Kamata, T. Nakamura, and T. Sata, Valence stability of molybdenum in alkaline earth molybdates, *Mater. Res. Bull.* **10**, 373 (1975).

[118] H. H. Wang, D. F. Cui, Y. L. Zhou, Z. H. Chen, F. Chen, T. Zhao, H. B. Lu, G. Z. Yang, M. C. Xu, Y. C. Lan, X. L. Chen, H. J. Qian, and F. Q. Liu, Growth and characterization of $SrMoO_3$ thin films, *J. Cryst. Growth* **226**, 261 (2001).

[119] H. H. Wang, G. Z. Yang, D. F. Cui, H. B. Lu, T. Zhao, F. Chen, Y. L. Zhou, Z. H. Chen, Y. C. Lan, Y. Ding, L. Chen, X. L. Chen, and J. K. Liang, Epitaxial growth and electric characteristics of $SrMoO_3$ thin films, *J. Vac. Sci. Technol. A* **19**, 930 (2001).

[120] A. Radetinac, K. S. Takahashi, L. Alff, M. Kawasaki, and Y. Tokura, Single-crystalline $CaMoO_3$ and $SrMoO_3$ films grown by pulsed laser deposition in a reductive atmosphere, *Appl. Phys. Express* **3**, 073003 (2010).

[121] D. B. Chrisey and G. K. Hubler, eds., *Pulsed Laser Deposition of Thin Films* (John Wiley & Sons, Inc., 1994).

[122] P. R. Willmott and J. R. Huber, Pulsed laser vaporization and deposition, *Rev. Mod. Phys.* **72**, 315 (2000).

[123] T. Ohnishi, H. Koinuma, and M. Lippmaa, Pulsed laser deposition of oxide thin films, *Appl. Surf. Sci.* **252**, 2466 (2006).

[124] *User Manual for Dycor LC-D Residual Gas Analyzer*, AMETEK Process Instruments, Pittsburgh PA, USA (2007).

[125] W. Braun, *Applied RHEED: Reflection High-Energy Electron Diffraction During Crystal Growth* (Springer, 1999).

[126] G. J. H. M. Rijnders, G. Koster, D. H. A. Blank, and H. Rogalla, In situ monitoring during pulsed laser deposition of complex oxides using reflection high energy electron diffraction under high oxygen pressure, *Appl. Phys. Lett.* **70**, 1888 (1997).

[127] G. Rijnders and D. H. A. Blank, Real-time growth monitoring by high-pressure RHEED during pulsed laser deposition, in *Thin Films and Heterostructures for Oxide Electronics*, edited by S. B. Ogale (Springer US, 2005), chap. 12, pp. 355–384.

[128] G. Koster, Artificially layered oxides by pulsed laser deposition, Ph.D. thesis, University of Twente (1999), available online at: `http://doc.utwente.nl/23466/`.

[129] J. H. Neave, B. A. Joyce, P. J. Dobson, and N. Norton, Dynamics of film growth of GaAs by MBE from rheed observations, *Appl. Phys. A* **31**, 1 (1983).

[130] P. J. Dobson, B. A. Joyce, J. H. Neave, and J. Zhang, Current understanding and applications of the RHEED intensity oscillation technique, *J. Cryst. Growth* **81**, 1 (1987).

[131] Y. Horio and A. Ichimiya, Origin of phase shift phenomena in RHEED intensity oscillation curves, *Ultramicroscopy* **55**, 321 (1994).

[132] B. E. Warren, *X-Ray Diffraction* (Dover Publications, Inc., 1990).

[133] F. J. Giessibl, Advances in atomic force microscopy, *Rev. Mod. Phys.* **75**, 949 (2003).

[134] C. Bell, S. Harashima, Y. Hikita, and H. Y. Hwang, Thickness dependence of the mobility at the $LaAlO_3/SrTiO_3$ interface, *Appl. Phys. Lett.* **94**, 222111 (2009).

[135] R. Yamamoto, C. Bell, Y. Hikita, H. Y. Hwang, H. Nakamura, T. Kimura, and Y. Wakabayashi, Structural comparison of *n*-type and *p*-type $LaAlO_3/SrTiO_3$ interfaces, *Phys. Rev. Lett.* **107**, 036104 (2011).

[136] T. Tanaka, K. Matsunaga, Y. Ikuhara, and T. Yamamoto, First-principles study on structures and energetics of intrinsic cacancies in $SrTiO_3$, *Phys. Rev. B* **68**, 205213 (2003).

[137] S. N. Ruddlesden and P. Popper, New compounds of the K_2NiF_4 type, *Acta Crystallogr.* **10**, 538 (1957).

[138] R. Meyer, R. Waser, J. Helmbold, and G. Borchardt, Cationic surface segregation in donor-doped $SrTiO_3$ under oxidizing conditions, *J. Electroceram.* **9**, 101 (2002).

[139] H. Yamada and G. R. Miller, Point defects in reduced strontium titanate, *J. Solid State Chem.* **6**, 169 (1973).

[140] T. Ohnishi, M. Lippmaa, T. Yamamoto, S. Meguro, and H. Koinuma, Improved stoichiometry and misfit control in perovskite thin film formation at a critical fluence by pulsed laser deposition, *Appl. Phys. Lett.* **87**, 241919 (2005).

[141] H. K. Sato, C. Bell, Y. Hikita, and H. Y. Hwang, Stoichiometry control of the electronic properties of the $LaAlO_3/SrTiO_3$ heterointerface, *Appl. Phys. Lett.* **102**, 251602 (2013).

[142] X. Luo, B. Wang, and Y. Zheng, First-principles study on energetics of intrinsic point defects in $LaAlO_3$, *Phys. Rev. B* **80**, 104115 (2009).

[143] X. Luo and B. Wang, Structural and elastic properties of $LaAlO_3$ from first-principles calculations, *J. Appl. Phys.* **104**, 073518 (2008).

[144] F. A. Kröger and H. J. Vink, Relations between the concentrations of imperfections in crystalline solids, *Solid State Phys.* **3**, 307 (1956).

[145] M. P. Warusawithana, C. Richter, J. A. Mundy, P. Roy, J. Ludwig, S. Paetel, T. Heeg, A. A. Pawlicki, L. F. Kourkoutis, M. Zheng, M. Lee, B. Mulcahy, W. Zander, Y. Zhu,

J. Schubert, J. N. Eckstein, D. A. Muller, C. S. Hellberg, J. Mannhart, and D. G. Schlom, $SrTiO_3$ stoichiometry is key to electron liquid formation at $LaAlO_3/SrTiO_3$ interfaces, *Nature Commun.* **4**, 2351 (2013).

[146] I. M. Dildar, D. B. Boltje, M. H. S. Hesselberth, J. Aarts, Q. Xu, H. W. Zandbergen, and S. Harkema, Non-conducting interfaces of $LaAlO_3/SrTiO_3$ produced in sputter deposition: The role of stoichiometry, *Appl. Phys. Lett.* **102**, 121601 (pages 4) (2013).

[147] E. Breckenfeld, N. Bronn, J. Karthik, A. R. Damodaran, S. Lee, N. Mason, and L. W. Martin, Effect of growth induced (non)stoichiometry on interfacial conductance in $LaAlO_3/SrTiO_3$, *Phys. Rev. Lett.* **110**, 196804 (2013).

[148] T. Ando, A. B. Fowler, and F. Stern, Electronic properties of two-dimensional systems, *Rev. Mod. Phys.* **54**, 437 (1982).

[149] H. Uwe, R. Yoshizaki, T. Sakudo, A. Izumi, and T. Uzumaki, Conduction band structure of $SrTiO_3$, *Jpn. J. Appl. Phys.* **24S2**, 335 (1985).

[150] N. W. Ashcroft and N. D. Mermin, *Solid State Physics* (Thomson Learning, Inc., 1976).

[151] Y. Kozuka, Y. Hikita, C. Bell, and H. Y. Hwang, Dramatic mobility enhancements in doped $SrTiO_3$ thin films by defect management, *Appl. Phys. Lett.* **97**, 012107 (2010).

[152] Y. Kozuka, M. Kim, H. Ohta, Y. Hikita, C. Bell, and H. Y. Hwang, Enhancing the electron mobility via delta-doping in $SrTiO_3$, *Appl. Phys. Lett.* **97**, 222115 (2010).

[153] Y. Kozuka, M. Kim, C. Bell, B. G. Kim, Y. Hikita, and H. Y. Hwang, Two-dimensional normal-state quantum oscillations in a superconducting heterostructure, *Nature* **462**, 487 (2009).

[154] M. Kim, C. Bell, Y. Kozuka, M. Kurita, Y. Hikita, and H. Y. Hwang, Fermi surface and superconductivity in low-density high-mobility δ-doped $SrTiO_3$, *Phys. Rev. Lett.* **107**, 106801 (2011).

[155] M. Kim, Emergent low-dimensional quantum phenomena in $SrTiO_3$, Ph.D. thesis, The University of Tokyo (2012).

[156] O. Copie, V. Garcia, C. Bödefeld, C. Carrétéro, M. Bibes, G. Herranz, E. Jacquet, J.-L. Maurice, B. Vinter, S. Fusil, K. Bouzehouane, H. Jaffrès, and A. Barthélémy, Towards two-dimensional metallic behavior at $LaAlO_3/SrTiO_3$ interfaces, *Phys. Rev. Lett.* **102**, 216804 (2009).

[157] N. Reyren, S. Gariglio, A. D. Caviglia, D. Jaccard, T. Schneider, and J.-M. Triscone, Anisotropy of the superconducting transport properties of the $LaAlO_3/SrTiO_3$ interface, *Appl. Phys. Lett.* **94**, 112506 (2009).

[158] I. Pallecchi, M. Codda, E. Galleani d'Agliano, D. Marré, A. D. Caviglia, N. Reyren, S. Gariglio, and J.-M. Triscone, Seebeck effect in the conducting $LaAlO_3/SrTiO_3$ interface, *Phys. Rev. B* **81**, 085414 (2010).

[159] A. Dubroka, M. Rössle, K. W. Kim, V. K. Malik, L. Schultz, S. Thiel, C. W. Schneider, J. Mannhart, G. Herranz, O. Copie, M. Bibes, A. Barthélémy, and C. Bernhard, Dynamical response and confinement of the electrons at the $LaAlO_3/SrTiO_3$ interface, *Phys. Rev. Lett.* **104**, 156807 (2010).

[160] F. Gunkel, S. Hoffmann-Eifert, R. Dittmann, S. B. Mi, C. L. Jia, P. Meuffels, and R. Waser, High temperature conductance characteristics of $LaAlO_3/SrTiO_3$-heterostructures un-

der equilibrium oxygen atmospheres, *Appl. Phys. Lett.* **97**, 012103 (2010).

[161] F. Gunkel, P. Brinks, S. Hoffmann-Eifert, R. Dittmann, M. Huijben, J. E. Kleibeuker, G. Koster, G. Rijnders, and R. Waser, Influence of charge compensation mechanisms on the sheet electron density at conducting $LaAlO_3/SrTiO_3$-interfaces, *Appl. Phys. Lett.* **100**, 052103 (2012).

[162] R. Moos and K. H. Härdtl, Defect chemistry of donor-doped and undoped strontium titanate ceramics between 1000° and 1400°C, *J. Am. Ceram. Soc.* **80**, 2549 (1997).

[163] P. Pasierb, S. Komornicki, and M. Rekas, Comparison of the chemical diffusion of undoped and Nb-doped $SrTiO_3$, *J. Phys. Chem. Solids* **60**, 1835 (1999).

[164] B. Vinter and A. W. Overhauser, Resolution of Shubnikov-de Haas paradoxes in Si inversion layers, *Phys. Rev. Lett.* **44**, 47 (1980).

[165] J. P. Eisenstein, H. L. Störmer, V. Narayanamurti, A. C. Gossard, and W. Wiegmann, Effect of inversion symmetry on the band structure of semiconductor heterostructures, *Phys. Rev. Lett.* **53**, 2579 (1984).

[166] G. Khalsa and A. H. MacDonald, Theory of the $SrTiO_3$ surface state two-dimensional electron gas, *Phys. Rev. B* **86**, 125121 (2012).

[167] W. S. Marshall, C. A. Swenson, A. Gavrilin, and H. J. Schneider-Muntau, Development of "fast cool" pulse magnet coil technology at NHMFL, *Physica B* **346**, 594 (2004).

[168] V. V. Laguta, G. M. D, R. O. Kuzian, S. N. Nokhrin, I. P. Bykov, J. Rosa, L. Jastrabik, and M. G. Karkut, The photoinduced Ti^{3+} centre in $SrTiO_3$, *J. Phys.: Condens. Matter* **14**, 13813 (2002).

[169] A. D. Caviglia, M. Gabay, S. Gariglio, N. Reyren, C. Cancellieri, and J.-M. Triscone, Tunable Rashba spin-orbit interaction at oxide interfaces, *Phys. Rev. Lett.* **104**, 126803 (2010).

[170] M. Rasolt and Z. Tešanović, Theoretical aspects of superconductivity in very high magnetic fields, *Rev. Mod. Phys.* **64**, 709 (1992).

[171] Ariando, X. Wang, G. Baskaran, Z. Q. Liu, J. Huijben, J. B. Yi, A. Annadi, A. R. Barman, A. Rusydi, S. Dhar, Y. P. Feng, J. Ding, H. Hilgenkamp, and T. Venkatesan, Electronic phase separation at the $LaAlO_3/SrTiO_3$ interface, *Nature Commun.* **2**, 188 (2011).

[172] D. A. Dikin, M. Mehta, C. W. Bark, C. M. Folkman, C. B. Eom, and V. Chandrasekhar, Coexistence of superconductivity and ferromagnetism in two dimensions, *Phys. Rev. Lett.* **107**, 056802 (2011).

[173] L. Li, C. Richter, J. Mannhart, and R. C. Ashoori, Coexistence of magnetic order and two-dimensional superconductivity at $LaAlO_3/SrTiO_3$ interfaces, *Nature Phys.* **7**, 762 (2011).

[174] J. A. Bert, B. Kalisky, C. Bell, M. Kim, Y. Hikita, H. Y. Hwang, and K. A. Moler, Direct imaging of the coexistence of ferromagnetism and superconductivity at the $LaAlO_3/SrTiO_3$ interface, *Nature Phys.* **7**, 767 (2011).

[175] J. Kondo, Resistance minimum in dilute magnetic alloys, *Prog. Theor. Phys.* **32**, 37 (1964).

[176] I. S. Elfimov, S. Yunoki, and G. A. Sawatzky, Possible path to a new class of ferromagnetic and half-metallic ferromagnetic materials, *Phys. Rev. Lett.* **89**, 216403 (2002).

[177] N. Pavlenko, T. Kopp, E. Y. Tsymbal, G. A. Sawatzky, and J. Mannhart, Magnetic and superconducting phases at the $LaAlO_3/SrTiO_3$ interface: The role of interfacial Ti 3*d* electrons, *Phys. Rev. B* **85**, 020407 (2012).

[178] N. Pavlenko, T. Kopp, and J. Mannhart, Emerging magnetism and electronic phase separation at titanate interfaces, *Phys. Rev. B* **88**, 201104 (2013).

[179] B. W. Gardner, J. C. Wynn, P. G. Bjornsson, E. W. J. Straver, K. A. Moler, J. R. Kirtley, and M. B. Ketchen, Scanning superconducting quantum interference device susceptometry, *Rev. Sci. Instrum.* **72**, 2361 (2001).

[180] M. E. Huber, N. C. Koshnick, H. Bluhm, L. J. Archuleta, T. Azua, P. G. Bjornsson, B. W. Gardner, S. T. Halloran, E. A. Lucero, and K. A. Moler, Gradiometric micro-SQUID susceptometer for scanning measurements of mesoscopic samples, *Rev. Sci. Instrum.* **79**, 053704 (2008).

[181] M. R. Fitzsimmons, N. W. Hengartner, S. Singh, M. Zhernenkov, F. Y. Bruno, J. Santamaria, A. Brinkman, M. Huijben, H. J. A. Molegraaf, J. de la Venta, and I. K. Schuller, Upper limit to magnetism in $LaAlO_3/SrTiO_3$ heterostructures, *Phys. Rev. Lett.* **107**, 217201 (2011).

[182] R. Pentcheva and W. E. Pickett, Charge localization or itineracy at $LaAlO_3/SrTiO_3$ interfaces: Hole polarons, oxygen vacancies, and mobile electrons, *Phys. Rev. B* **74**, 035112 (2006).

[183] K. Michaeli, A. C. Potter, and P. A. Lee, Superconducting and ferromagnetic phases in $SrTiO_3/LaAlO_3$ oxide interface structures: Possibility of finite momentum pairing, *Phys. Rev. Lett.* **108**, 117003 (2012).

[184] S. Banerjee, O. Erten, and M. Randeria, Ferromagnetic exchange, spin-orbit coupling and spiral magnetism at the $LaAlO_3/SrTiO_3$ interface, *Nature Phys.* **9**, 626 (2013).

[185] B. Kalisky, J. A. Bert, B. B. Klopfer, C. Bell, H. K. Sato, M. Hosoda, Y. Hikita, H. Y. Hwang, and K. A. Moler, Critical thickness for ferromagnetism in $LaAlO_3/SrTiO_3$ heterostructures, *Nature Commun.* **3**, 922 (2012).

[186] J. A. Bert, K. C. Nowack, B. Kalisky, H. Noad, J. R. Kirtley, C. Bell, H. K. Sato, M. Hosoda, Y. Hikita, H. Y. Hwang, and K. A. Moler, Gate-tuned superfluid density at the superconducting $LaAlO_3/SrTiO_3$ interface, *Phys. Rev. B* **86**, 060503 (2012).

[187] J.-S. Lee, Y. W. Xie, H. K. Sato, C. Bell, Y. Hikita, H. Y. Hwang, and C.-C. Kao, Titanium d_{xy} ferromagnetism at the $LaAlO_3/SrTiO_3$ interface, *Nature Mater.* **12**, 703 (2013).

[188] B. Kalisky, J. A. Bert, C. Bell, Y. Xie, H. K. Sato, M. Hosoda, Y. Hikita, H. Y. Hwang, and K. A. Moler, Scanning probe manipulation of magnetism at the $LaAlO_3/SrTiO_3$ heterointerface, *Nano Lett.* **12**, 4055 (2012).

[189] B. Kalisky, E. M. Spanton, H. Noad, J. R. Kirtley, K. C. Nowack, C. Bell, H. K. Sato, M. Hosoda, Y. Xie, Y. Hikita, C. Woltmann, G. Pfanzelt, R. Jany, C. Richter, H. Y. Hwang, J. Mannhart, and K. A. Moler, Locally enhanced conductivity due to the tetragonal domain structure in $LaAlO_3/SrTiO_3$ heterointerfaces, *Natutre Mater.* **12**, 1091 (2013).

[190] M. Sing, G. Berner, K. Goß, A. Müller, A. Ruff, A. Wetscherek, S. Thiel, J. Mannhart, S. A. Pauli, C. W. Schneider, P. R. Willmott, M. Gorgoi, F. Schäfers, and R. Claessen, Profiling the interface electron gas of $LaAlO_3/SrTiO_3$ heterostructures with hard x-ray

photoelectron spectroscopy, *Phys. Rev. Lett.* **102**, 176805 (2009).

[191] K.-J. Zhou, M. Radovic, J. Schlappa, V. Strocov, R. Frison, J. Mesot, L. Patthey, and T. Schmitt, Localized and delocalized Ti 3*d* carriers in $LaAlO_3/SrTiO_3$ superlattices revealed by resonant inelastic x-ray scattering, *Phys. Rev. B* **83**, 201402 (2011).

[192] M. Takizawa, S. Tsuda, T. Susaki, H. Y. Hwang, and A. Fujimori, Electronic charges and electric potential at $LaAlO_3/SrTiO_3$ interfaces studied by core-level photoemission spectroscopy, *Phys. Rev. B* **84**, 245124 (2011).

[193] M. Gabay and J.-M. Triscone, Oxide heterostructures: Hund rules with a twist, *Nature Phys.* **9**, 610 (2013).

[194] P. Gambardella, S. S. Dhesi, S. Gardonio, C. Grazioli, P. Ohresser, and C. Carbone, Localized magnetic states of Fe, Co, and Ni impurities on alkali metal films, *Phys. Rev. Lett.* **88**, 047202 (2002).

[195] H. Ikeno, F. M. F. de Groot, E. Stavitski, and I. Tanaka, Multiplet calculations of $L_{2,3}$ x-ray absorption near-edge structures for 3d transition-metal compounds, *J. Phys.: Condens. Matter* **21**, 104208 (2009).

[196] W.-J. Son, E. Cho, B. Lee, J. Lee, and S. Han, Density and spatial distribution of charge carriers in the intrinsic *n*-type $LaAlO_3$-$SrTiO_3$ interface, *Phys. Rev. B* **79**, 245411 (2009).

[197] P. Delugas, A. Filippetti, V. Fiorentini, D. I. Bilc, D. Fontaine, and P. Ghosez, Spontaneous 2-dimensional carrier confinement at the *n*-type $SrTiO_3/LaAlO_3$ interface, *Phys. Rev. Lett.* **106**, 166807 (2011).

[198] E. Abrahams, P. W. Anderson, D. C. Licciardello, and T. V. Ramakrishnan, Scaling theory of localization: Absence of quantum diffusion in two dimensions, *Phys. Rev. Lett.* **42**, 673 (1979).

[199] H. Jeffrey Gardner, A. Kumar, L. Yu, P. Xiong, M. P. Warusawithana, L. Wang, O. Vafek, and D. G. Schlom, Enhancement of superconductivity by a parallel magnetic field in two-dimensional superconductors, *Nature Phys.* **7**, 895 (2011).

[200] C. H. Ahn, J.-M. Triscone, and J. Mannhart, Electric field effect in correlated oxide systems, *Nature* **424**, 1015 (2003).

[201] W. M. Haynes, ed., *CRC Handbook of Chemistry and Physics* (CRC Press/Taylor and Francis, 2013), 94th ed.

[202] S. Hayashi, R. Aoki, and T. Nakamura, Metallic conductivity in perovskite-type compounds $A\mathrm{MoO_3}$ (A = Ba, Sr, Ca) down to 2.5 K, *Mater. Res. Bull.* **14**, 409 (1979).

[203] Y. Krockenberger, M. Uchida, K. S. Takahashi, M. Nakamura, M. Kawasaki, and Y. Tokura, Growth of superconducting Sr_2RuO_4 thin films, *Appl. Phys. Lett.* **97**, 082502 (2010).

[204] N. Nagaosa, J. Sinova, S. Onoda, A. H. MacDonald, and N. P. Ong, Anomalous Hall effect, *Rev. Mod. Phys.* **82**, 1539 (2010).

[205] L. I. Ivleva, N. S. Kozlova, and A. V. Kir'yanov, Influence of electron irradiation on optical properties of scheelite crystals, *Laser Physics* **20**, 635 (2010).

[206] Z. Li, J. Wang, H. Zhang, H. Yu, and Z. Pan, Growth and characterization of large $SrMoO_4$ crystals, *J. Cryst. Growth* **318**, 679 (2011).

[207] J. G. Jones, A. A. Voevodin, and J. S. Zabinski, Characterization of plume fluence for

laser ablation of yttria stabilized zirconia in mixed oxygen and argon environments, *Surf. Coat. Technol.* **146**, 258 (2001).

[208] C. Aruta, S. Amoruso, R. Bruzzese, X. Wang, D. Maccariello, F. Miletto Granozio, and U. Scotti di Uccio, Pulsed laser deposition of $SrTiO_3/LaGaO_3$ and $SrTiO_3/LaAlO_3$: Plasma plume effects, *Appl. Phys. Lett.* **97**, 252105 (2010).

[209] T. Ohnishi and K. Takada, High-rate growth of high-crystallinity $LiCoO_2$ epitaxial thin films by pulsed laser deposition, *Appl. Phys. Express* **5**, 055502 (2012).

[210] Y. Kozuka, H. Seki, T. C. Fujita, S. Chakraverty, K. Yoshimatsu, H. Kumigashira, M. Oshima, M. S. Bahramy, R. Arita, and M. Kawasaki, Epitaxially stabilized $EuMoO_3$: A new itinerant ferromagnet, *Chem. Mater.* **24**, 3746 (2012).

[211] K. Shimamoto, K. Hatabayashi, Y. Hirose, S. Nakao, T. Fukumura, and T. Hasegawa, Full compensation of oxygen vacancies in $EuTiO_3$ (001) epitaxial thin film stabilized by a $SrTiO_3$ surface protection layer, *Appl. Phys. Lett.* **102**, 042902 (2013).

[212] J. R. Sims, D. G. Rickel, C. A. Swenson, J. B. Schillig, G. W. Ellis, and C. N. Ammerman, Assembly, commissioning and operation of the NHMFL 100 tesla multi-pulse magnet system, *IEEE Trans. Appl. Supercond.* **18**, 587 (2008).

[213] N. Nakagawa, M. Asai, Y. Mukunoki, T. Susaki, and H. Y. Hwang, Magnetocapacitance and exponential magnetoresistance in manganite–titanate heterojunctions, *Appl. Phys. Lett.* **86**, 082504 (2005).

[214] T. Muramatsu, Y. Muraoka, and Z. Hiroi, Photocarrier injection and current–voltage characteristics of $La_{0.8}Sr_{0.2}MnO_3/SrTiO_3$:Nb heterojunction at low temperature, *Jpn. J. Appl. Phys.* **44**, 7367 (2005).

[215] T. Fujii, M. Kawasaki, A. Sawa, H. Akoh, Y. Kawazoe, and Y. Tokura, Hysteretic current–voltage characteristics and resistance switching at an epitaxial oxide Schottky junction $SrRuO_3/SrTi_{0.99}Nb_{0.01}O_3$, *Appl. Phys. Lett.* **86**, 012107 (2005).

Publication and Presentation Lists

Publications

I. B. Kalisky, E. M. Spanton, H. Noad, J. R. Kirtley, K. C. Nowack, C. Bell, H. K. Sato, M. Hosoda, Y. W. Xie, Y. Hikita, C. Woltmann, G. Pfanzelt, R. Jany, C. Richter, H. Y. Hwang, J. Mannhart, and K. A. Moler, "Locally enhanced conductivity due to the tetragonal domain structure in $LaAlO_3/SrTiO_3$ heterointerfaces," *Nature Mater.* **12**, 1091 (2013).

II. Y. Yamada, H. K. Sato, Y. Hikita, H. Y. Hwang, and Y. Kanemitsu, "Measurement of the femtosecond optical absorption of $LaAlO_3/SrTiO_3$ heterostructures: Evidence for an extremely slow electron relaxation at the interface," *Phys. Rev. Lett.* **111**, 047403 (2013).

III. H. K. Sato, C. Bell, Y. Hikita, and H. Y. Hwang, "Stoichiometry control of the electronic properties of the $LaAlO_3/SrTiO_3$ heterointerface," *Appl. Phys. Lett.* **102**, 251602 (2013).

IV. J.-S. Lee, Y. W. Xie, H. K. Sato, C. Bell, Y. Hikita, H. Y. Hwang, and C.-C. Kao, "Titanium d_{xy} ferromagnetism at the $LaAlO_3/SrTiO_3$ interface," *Nature Mater.* **12**, 703 (2013).

V. J. A. Bert, K. C. Nowack, B. Kalisky, H. Noad, J. R. Kirtley, C. Bell, H. K. Sato, M. Hosoda, Y. Hikita, H. Y. Hwang, and K. A. Moler, "Gate-tuned superfluid density at the superconducting $LaAlO_3/SrTiO_3$ interface," *Phys. Rev. B* **86**, 060503(R) (2012).

VI. B. Kalisky, J. A. Bert, C. Bell, Y. W. Xie, H. K. Sato, M. Hosoda, Y. Hikita, H. Y. Hwang, and K. A. Moler, "Scanning Probe Manipulation of Magnetism at the $LaAlO_3/SrTiO_3$ Heterointerface," *Nano Lett.* **12**, 4055 (2012).

VII. B. Kalisky, J. A. Bert, B. B. Klopfer, C. Bell, H. K. Sato, M. Hosoda, Y. Hikita, H. Y. Hwang, and K. A. Moler, "Critical thickness for ferromagnetism in $LaAlO_3/SrTiO_3$ heterostructures," *Nature Commun.* **3**, 922 (2012).

VIII. H. K. Sato, J. A. Mundy, T. Higuchi, Y. Hikita, C. Bell, D. A. Muller, and H. Y. Hwang, "Nanometer-scale epitaxial strain release in perovskite heterostructures using "$SrAlO_x$" sliding buffer layers," *Appl. Phys. Lett.* **98**, 171901 (2011).

Presentations (International Conference)

1. H. K. Sato, C. Bell, Y. Hikita, and H. Y. Hwang, "Stoichiometry control of the electronic properties of the $LaAlO_3/SrTiO_3$ heterointerface," 2012 Materials Research Society Fall Meeting, Boston MA, USA, November 2012.
2. H. Sato, T. Higuchi, Y. Hikita, and H. Y. Hwang, "Fabrication of bulk-like single crystal

$LaAlO_3$ thin films on $SrTiO_3$ (001) using "$SrAlO_x$" buffer layers," 2010 Materials Research Society Spring Meeting, San Francisco CA, USA, April 2010.

Presentations (Domestic Conference)

1. H. Sato, C. Bell, Y. Hikita, and H. Y. Hwang, "Stoichiometry control of the electronic properties of the $LaAlO_3/SrTiO_3$ heterointerface," JSAP 60th Spring Meeting, Kanagawa, Japan, March 2013.
2. H. Sato, C. Bell, Y. Hikita, and H. Y. Hwang, "Tuning the electronic properties of the $LaAlO_3/SrTiO_3$ interface by growth conditions," JSAP 58th Spring Meeting, Kanagawa, Japan, March 2011.
3. H. Sato, T. Higuchi, C. Bell, Y. Hikita, and H. Y. Hwang, "Cation stoichiometry of $LaAlO_3$ thin films grown by pulsed laser deposition," JSAP 57th Spring Meeting, Kanagawa, Japan, March 2010.
4. H. Sato, T. Higuchi, Y. Hikita, and H. Y. Hwang, "Fabrication of bulk-like and epitaxial $LaAlO_3$ thin films using "$SrAlO_x$" buffer layers," JSAP 70th Autumn Meeting, Toyama, Japan, September 2009.

Thesis

The Relationship between Structural and Electrical Properties in Complex Oxide Heterostructures

Hiroki Sato

Department of Advanced Materials Science
Graduate School of Frontier Sciences
The University of Tokyo

Supervisors:
Prof. Hiroshi Okamoto
Prof. Harold Y. Hwang (SLAC National Accelerator Laboratory, USA)

First version submitted December 2013
Revised version submitted February 2014